CHARACTERIZATION OF IGNITION AND COMBUSTION OF NITROMETHANE AND ISOPROPYL NITRATE MONOPROPELLANT DROPLETS

by

Angela W. Mbugua

A Dissertation

Submitted to the Faculty of Purdue University

In Partial Fulfillment of the Requirements for the degree of

Doctor of Philosophy

School of Aeronautics & Astronautics

West Lafayette, Indiana

May 2019

THE PURDUE UNIVERSITY GRADUATE SCHOOL
STATEMENT OF COMMITTEE APPROVAL

Dr. Sally Bane, Chair

    Department of Aeronautics and Astronautics

Dr. Timothée Pourpoint

    Department of Aeronautics and Astronautics

Dr. Robert Lucht

    Department of Mechanical Engineering

Dr. Steven Son

    Department of Mechanical Engineering

Approved by:

    Dr. Weinong Chen

        Head of the Graduate Program

For dad, I miss you; and for mum, lyn, nyoiks, gits, and my husband and love, gogz

ACKNOWLEDGMENTS

I would like to thank my advisor, Professor Sally P. Bane, for her encouragement and support throughout my graduate school experience. Her guidance gave me the space to make mistakes, learn from them and grow as I navigated the ups and downs of study and research. I would also like to thank my committee members for all their advice. Specifically, I would like to thank Professor Timothée Pourpoint, for giving me the amazing opportunity to work with hypergols; Professor Steven Son, for his help in redefining the direction of this research; and Professor Robert Lucht, for graciously providing the space to perform experiments, the opportunity to work with lasers, and for being an example of excellence and humility in academia and beyond. My thanks to Dr. Aman Satija, for his mentorship, support, samosas, encouragement and patience with me throughout this study. His thoroughness and resilience in research was evident at each stage of this work. Thank you to Dr. Dustin Cruise, I will never forget the droplet song. My gratitude goes to Dr. Daniel Leaird, for providing some of the resources for the experiments, time and time again. My thanks also go to the ASL machine shop (Jim, Rob and Jerry), you are all rock stars. To one of the most helpful people in the world, John Phillips, you are too good at what you do! To Professor Terrence Meyer and his group, thank you for graciously lending us your resources to be able to perform the experiments. Many thanks to the students and staff at the Green Propellants Laboratory for all your help and resources over the years, I have learned so much from you all. Thank you to Dr. Rohan Gejji, for your time and advice in designing and setting up the experiment. To Dr. Bhavini Singh, Dr. Ravichandra Jagannath, and Dr. Prashanth Bangalore, thank you for all your help, and for accommodating all my many tests. To Dr. Lalit Rajendran, thank you for all your support and encouragement since the beginning, you are one of the smartest people I have ever known. My gratitude to Dr. Nadia Numa, for the meals, the tears, the laughter, the prayers, and the encouragement. I could not have finished this season without you. To Dr. and Mrs. Paa Kwasi Adusei, your love, prayers and sacrifice are overwhelming, thank you for everything you have done. I thank my family, who have been in this season alongside me, your love and support have meant everything to me. Mum, lyn, nyoiks and gits, always together. To my husband Sam, you are an extension of me, thank you for giving me so much to live for, I could not have done this without you. Finally, to my God, who has never let me down, thank you for charting this course, and for always finishing what You begin. Your grace will always be sufficient for me.

TABLE OF CONTENTS

LIST OF TABLES

LIST OF FIGURES

NOMENCLATURE

A'	Pre-exponential factor		**Subscripts**	
E	Activation energy		F	Fuel
R_u	Universal gas constant		O	Oxidizer
Y	Mass fraction		FP	Decomposition flame products
ε	Small perturbation parameter		P	Oxidation flame products (Hybrid model)
T_a	Activation temperature			
T	Temperature		A	Region A
B	Spalding number (Droplet ignition model)		B	Region B (Hybrid model)
ν	Stoichiometric air-fuel ratio		C	Region C
Δh_c	Heat of combustion		l	Liquid
λ	Thermal conductivity		I	Decomposition flame (Hybrid model)
C	Specific heat at constant pressure		I	Ignition (Droplet ignition model)
L^*	Nondimensional heat of vaporization		f	Oxidation flame
β	Nondimensional radial distance (Hybrid model)		∞	Ambient conditions
β	Heat transfer parameter (Droplet ignition model)			
θ	Nondimensional temperature			
D_a	Damköhler number			
Δ	Modified Damköhler number			
K	Burn rate constant			

ABSTRACT

Author: Mbugua, Angela, W. PhD
Institution: Purdue University
Degree Received: May 2019
Title: Characterization of Ignition and Combustion of Nitromethane and Isopropyl Nitrate
  Monopropellant Droplets
Major Professor: Sally Bane

Conventional rocket propellants such as monomethyl hydrazine (MMH) and hydrazine have been used for decades due to their high specific impulse and performance. However, interest in greener alternatives, including HAN or HAN-based propellants, has grown due to high levels of toxicity and difficulties in the handling and storage of conventional fuels. Included among potential propellants are monopropellants nitromethane (NM) and isopropyl nitrate (IPN) and their blends. Though large-scale investigations on the ignition and combustion of these fuels have been done, the ignition and combustion processes of these monopropellant fuels are still not well understood. Droplet studies have been traditionally and extensively employed to decipher the influence of ambient conditions and fuel properties on ignition and combustion of different fuels. These fundamental studies allow for the isolation of different factors such as ambient temperature and initial droplet size among others, to provide a deeper understanding of their effects in overall spray combustion.

The research described here seeks to add to the knowledge on the ignition and combustion processes of NM and IPN through single droplet ignition and combustion studies. To this end, the first effort has been to establish a suitable method of studying the ignition and combustion of droplets in conditions similar to those in practical systems. Droplet ignition delay measurements for NM and IPN droplets have also been conducted, and the influence of ambient temperature and droplet size has been studied. The double flame structures of NM and IPN, representative of hybrid combustion, have also been observed. In addition, the applicability of the hybrid combustion model, developed to predict mass burning rates for hypergolic fuels exhibiting hybrid burning including MMH, UDMH and hydrazine by Allison et al. [1], has been assessed. Lastly, the ability of the quasi-steady droplet ignition model to predict ignition delays of IPN and NM monopropellant droplets is also discussed.

1. INTRODUCTION

1.1 Motivation

The exothermic decomposition of pure liquid monopropellants has found its niche in space vehicles, high altitude unmanned aerial vehicles, as well as in underwater power sources. Hydrazine, a hypergolic monopropellant, and its derivatives have been used in the space industry for over four decades due to their high specific impulse and performance. However, due to high levels of toxicity and difficulties in handling, the combustion community has been motivated to find greener alternatives without sacrificing performance. Available alternatives and candidates include hydrogen peroxide, hydroxyl-ammonium nitrate (HAN) or HAN-based propellants, nitromethane (NM) (and its blends) and isopropyl nitrate (IPN) (and its blends) [1,2]. Their relative performance is shown in Figure 1.
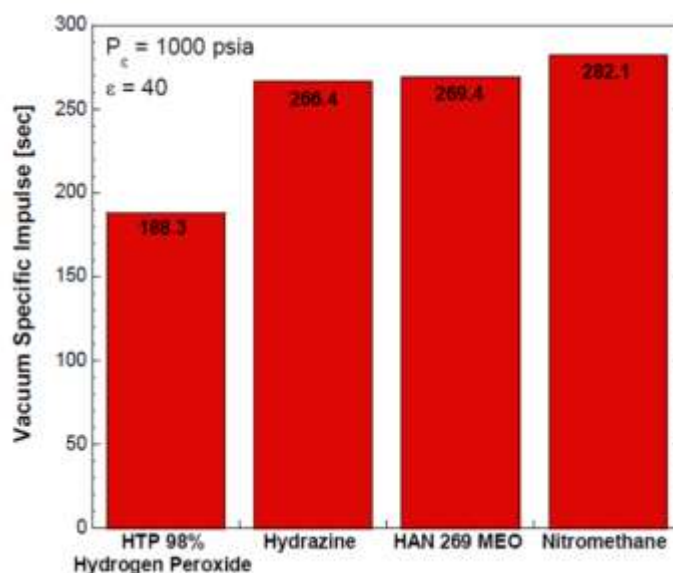
Figure 1. Monopropellant performance comparison [3]

Interest in NM as a propellant began in the 1930s but dwindled after the discovery of hydrazine. In more recent years as the search for greener alternatives has increased, a renewed interest in nitromethane has motivated studies to characterize its combustion. Due to its high energy content and ease of storage for long periods of time, NM has potential for use in space thrusters as a

replacement for the more conventional hydrazine and hydrazine-based monopropellant fuels. NM can also be considered for use in bipropellant propulsion devices when combined with oxidizers. Different additives have also been studied to enhance the performance of nitromethane and nitromethane-based propellants. Another promising monopropellant fuel candidate is isopropyl nitrate (IPN). Out of the aforementioned fuels, IPN is known for its non-toxicity, non-corrosiveness, its low cost and low sensitivity to premature detonation. It has been used in gas turbine engines and as an improver of diesel cetane [2]. As such, both these monopropellant fuels (NM and IPN) have been chosen for the experiments in this work.

The ignition process of liquid fuels in rocket or gas turbine engines involves initiation of pre-ignition reactions. The rates of these reactions, their products and the associated heat release are closely associated with transport properties like heat and mass transfer. To decipher the degree of influence of these properties on ignition, experiments have been designed to isolate and separately study the effect of important physical and chemical factors such as ambient temperature and ambient oxygen concentration among others [4]. There have been many direct studies on ignition and combustion of liquid sprays, however these studies do not easily provide detailed insight on the complex physical and chemical processes controlling droplet ignition and combustion within the spray. It is for this reason that single droplet and multi-droplet studies using droplet arrays and droplet clouds are important. A better understanding of these smaller scale systems can help us understand overall spray combustion characteristics. In addition, more detailed information on the complex physical and chemical processes that occur during ignition and combustion of fuel droplets and fuel droplet arrays serve to improve combustion efficiency and improve the control of pollutant formation in combustion devices [5].

A variety of droplet sizes are present in any given liquid spray. In addition, these droplets may experience varying ambient conditions during their lifetime. These wide-ranging ambient conditions include varying mixtures of oxidizer, fuel vapor and combustion products in the surroundings, high relative velocities between the oxidizing gas and the droplet, and the presence of flame zones of other droplets in close proximity. All these factors affect the ignition and combustion characteristics of the droplet. Isolating these factors in single droplet studies process provides a deeper understanding into their effects in the overall combustion process in a spray [6].

For example, critical droplet size for ignition and its dependence on ambient conditions and other droplet parameters can be obtained from single droplet experiments.

An important aspect of droplet ignition and combustion studies is the ability to extend the results to droplet sizes realized in practical sprays [7]. There have been very few investigations into the effect of varying initial droplet diameter, yet the ignition and combustion behavior may vary greatly between large and small droplets, and it is uncertain to what degree results for larger droplets can be extrapolated to smaller droplets. The limited number of studies on small droplets in the literature can be largely attributed to experimental difficulties. Consequently, numerical studies have become important in predicting ignition and combustion behavior of droplets less than 200 µm in diameter. In light of this knowledge gap, a primary objective of this research is to understand the effects of droplet diameter on the ignition and combustion characteristics of the fuels studied in this work.

1.2   Research Objectives

This research focuses on characterizing the ignition and combustion behavior of non-toxic, non-corrosive, monopropellant droplets that could potentially replace conventional toxic and hard-to-handle hypergolic propellants such as hydrazine (and its derivatives) and nitrogen tetroxide. The monopropellants nitromethane (NM) and isopropyl nitrate (IPN) were chosen for this work because they are promising candidates, but their ignition characteristics and mode of combustion, specifically "hybrid combustion," are not well understood. To investigate their ignition and combustion characteristics, an experiment was developed in which varying droplet sizes are ignited in the post-combustion gases of a flat flame burner. The specific objectives of this study are to:

1) Investigate and establish a suitable technique for droplet ignition and combustion studies
2) Measure the effect of varying droplet size and ambient temperature on the mass burning rate and ignition delay of NM and IPN monopropellant droplets
3) Assess the ability of the hybrid combustion model (originally derived to predict burning rates for MMH) to be extended to burning rates for NM and IPN monopropellant droplets burning in oxidizing atmospheres

4) Assess the ability of the thermal droplet ignition model to predict ignition delays for monopropellant droplets in oxidizing atmospheres

1.3 Document Organization

This document is divided into five chapters. Chapter 1 consists of the motivation for this research and the overall research objectives. Background information relevant to the research is provided in Chapter 2, while Chapters 3 and 4 describe the experimental method employed in this study and the results obtained, respectively. Chapter 5 summarizes the findings and proposes future research work. Supporting material can be found in the Appendices.

2. BACKGROUND

2.1 Introduction

Liquid fuel combustion is an extremely important area of study in the field of combustion. Research in this area has led to reduction of harmful emissions and more efficient conversion of chemical energy to thermal energy in devices such as liquid-fueled rocket engines and gas turbine combustion systems. Nevertheless, additional experimental data is needed to continue to improve existing combustion models and modeling techniques.

In general, liquid fuel combustion involves the burning of liquid droplets in a gas. Consequently, the key to understanding spray combustion is understanding how individual droplets of fuel burn in oxidizing media. Some of the parameters that influence droplet and spray combustion include droplet size, fuel composition, ambient conditions (such as gas composition, temperature and pressure), and relative velocity between the droplet and the surrounding gas [8]. Droplet combustion studies form the foundation for predicting steady state combustion chamber performance and have been conducted extensively using a variety of fuels including hydrocarbon and hypergolic propellants.

The earliest research on the behavior and evolution of individual liquid droplets began in the 1930s. A majority of these early studies focused on investigating condensation and evaporation as it related to a variety of applications from aerosols to liquid fuel combustion. Significant interest in droplet ignition and combustion processes arose in the 1950s [9]. Since that time, the ignition and combustion of isolated liquid fuel droplets has formed an essential step in the understanding of combustion processes occurring in compression ignition engines, gas turbines, and liquid fuel rocket engines [7]. Understanding isolated droplet evaporation, ignition and combustion is an important fundamental step in understanding the overall spray evaporation and combustion processes occurring in these devices [10]. In addition, it also provides fundamental information and empirical data for validation of models on spray behavior [11].

A challenging problem in ignition and combustion research is determining the critical conditions for ignition based on the physical and chemical factors involved in the ignition process [12]. As mentioned previously, though the study of isolated droplets neglects important spray combustion processes associated with the presence of other droplets in the system, the simplification of the problem to single droplets is beneficial for studying basic processes involved in the complex ignition process [13]. It is the intent of this document to use this approach to improve understanding of monopropellant droplet ignition and combustion. However, rather than directly apply the results of single droplet ignition and combustion studies to spray combustion, it is more realistic to consider the isolated droplet as an entity from which a larger spray model can be built [6].

Most of the droplet studies in literature have used droplets with relatively large diameters (>1mm). Of the sub-millimeter droplet studies, most work has been on free-falling arrays rather than on single droplets. The following sections summarize the literature on the ignition and combustion of bipropellant and monopropellant droplets, including both hydrocarbon and hypergolic fuels. The chapter concludes with an overview of the theoretical models employed in predicting droplet ignition and combustion rates, with a primary focus on the quasi-steady droplet ignition theory and the hybrid combustion theory as it relates to this work.

2.2 Droplet Ignition and Combustion

2.2.1 Droplet Ignition and Ignition Delay

The problem of interest in this work is the ignition and burning of a liquid fuel droplet in an oxidizing gaseous atmosphere. For non-hypergolic fuels, this oxidizing atmosphere must be at a much higher temperature than the boiling point of the liquid fuel. Fundamental studies of this type of problem have long been recognized as important in understanding spray combustion, especially for high-density fuels [14]. Extensive research has been done on steady-state droplet combustion, while there are fewer studies on droplet ignition. Much of the droplet ignition work began in the early 1940s, with most studies focused on determining the ignitability of individual droplets and the conditions that lead to ignition such as temperature, pressure and ambient oxidizer concentration, as well as the effect of these parameters on ignition delay. The basic processes

involved in liquid fuel ignition can then be studied, and reaction rate constants may be obtained for complex ignition models.

The overall ignition process for an isolated non-hypergolic droplet introduced into a hot oxidizing atmosphere begins with droplet heating and vaporization. As the droplet surface temperature increases, the droplet continues to vaporize, and the fuel vapor is transported outwards where it mixes with the surrounding gas containing the oxidizer and initially weak exothermic reactions are initiated. As droplet heating continues, the rate of fuel vapor generation increase and the reactions intensify [15]. If the appropriate conditions are maintained, a state is eventually achieved in which the rate of chemical heat release exceeds the rate at which heat is transported away, leading to a chemical 'runaway' event, or *ignition*. It is at this stage that an envelope flame surrounding the droplet can generally be detected. If the droplet diameter is too small, there is insufficient vapor surrounding the droplet to form a combustible mixture with the ambient oxidizer or to sustain sufficient exothermic reactions to produce an ignition event [16]. For hypergolic droplets, it can be argued that the only difference in this process is the heating mechanism that contributes to vaporizing the fuel. Fast liquid-vapor reactions are initiated on contact between the liquid droplet and the gaseous oxidizer. It is these reactions that drive the vaporization process and determine the availability of fuel vapor for gas-phase reactions between the fuel and oxidizer.

One of the most fundamental parameters in the ignition of any propellant is ignition delay. In general, ignition delay is defined as the period of time that elapses between injection and ignition of propellants into a chamber. Though this definition is considered universal, Hurbert et. al [17] states the importance of making the distinction between hypergolic and non-hypergolic propellants when discussing ignition delay, as the ignition processes fundamentally differ. For hypergolic propellants, where spontaneous ignition occurs without any external source of energy, the ignition process is controlled by propellant kinetics during exothermic liquid-vapor reactions. For non-hypergolic propellants, ignition delay is controlled by the gas-phase kinetics, as well as energy input, vaporization rates and turbulent mixing [17]. In general, ignition delay is difficult to predict due to the variety of physical and chemical factors (such as ambient temperature, pressure, oxidizer concentration and others) that control the interactions between complex liquid- physical and chemical processes occurring during ignition [18]. The total ignition delay time includes the delay

caused by both physical processes such as heating, diffusion, mixing, atomization and evaporation, and the finite rate of the chemical kinetics of the reaction [19]. Short ignition delays are desirable in rocket engines to prevent hard starts caused by excess propellant in the combustion chamber, which can result in structural damage or explosion due to excessive pressure spikes.

Ignition delay has been experimentally defined in different ways in literature depending on the combustion characteristics of the propellants and the experimental techniques employed. In some studies, ignition delay is defined as the time it takes to record the first appearance of light, while other authors relate ignition delay with pressure spikes especially for large-scale engine tests where the pressure during ignition can be clearly observed to increase drastically. In addition, differences in injection techniques of the propellants also cause variations in ignition delay [20]. Other factors influencing ignition delay include propellant temperature, oxidizer-to-fuel (O/F) ratio, ambient pressure and ambient oxidizer concentration [21].

For liquid fuel droplets igniting and burning in gaseous oxidizing media, ignition delay has most often been defined as the time from introduction into the gaseous oxidizing environment to the instant a flame is observed either surrounding the droplet or in the wake region of the droplet [14]. Depending on the droplet size and propellant characteristics, other investigators have also determined ignition to have occurred when a spike in temperature or OH species concentration is detected.

Spray ignition delays are more difficult to determine than droplet ignition delays, but in many cases are preferred as they more closely resemble conditions in rocket thrusters. One approach to predicting spray ignition delay and that has been useful in deepening the understanding of overall spray ignition is studying ignition of droplet clouds or clusters. The term cloud or cluster refers to a group of more than 10 droplets [16]. In this case, ignition may occur outside or inside the cloud depending on the droplet density, and may involve one or several droplets [14]. Very dense droplet clouds can be visualized as a single large isolated droplet, with a fuel-rich core that inhibits reactions within the cloud, and ignition occurring outside the cloud of droplets is identified by a flame surrounding the droplet cloud.

2.2.2   Droplet Ignition and Burning Regimes

In droplet ignition and combustion research, two distinct thermal ignition and burning regimes have been identified in literature, namely the droplet-heating regime, also called the vaporization-controlled or diffusion-controlled regime, and the kinetically-controlled or reaction-controlled regime [22]–[24]. The diffusion-controlled regime is associated with relatively large droplets with low volatility and high boiling points, as well as high ambient temperatures. In contrast, the kinetically-controlled or reaction-controlled regime is associated with small droplets of fuels with high volatility reacting in relatively low ambient temperatures. These regimes depend on the competing rates of supply and consumption of the reactants. Differences in the ignition and combustion of droplets in these two regimes have been experimentally observed for different fuels and have resulted in the need to determine or predict the ignition or burning regime for a given droplet and ambient conditions. To this end, the Damköhler number (Da) has been defined in literature as the ratio between diffusion and reaction timescales and has been used to determine the regime in which a droplet will ignite or burn.

2.2.2.1   Ignition in the Kinetically-controlled and Diffusion-controlled Regimes

In the kinetically-controlled regime the rate of fuel and oxidizer consumption by chemical reaction is slower than the rate of supply by diffusion, while in the diffusion-controlled regime, the reaction rate is much faster than the diffusion rate, and as a result this regime is usually associated with a visible flame.

For droplets evaporating or reacting in the diffusion-controlled regime, a relatively long time is required to raise the droplet surface temperature to near the boiling point. As the droplet heats up, very little vaporization or mass loss takes place before the surface temperature of the droplet reaches sufficiently near boiling point for sufficient vaporization to take place leading to ignition [23]. The physical process of evaporation therefore dictates the progress of the reaction by controlling the vapor flux and consequently the convective heat loss in the vicinity of the droplet [13]. Once the droplet surface reaches near boiling point, sufficient fuel accumulation is achieved in the vicinity of the droplet, and the reaction is relatively fast leading to establishment of a diffusion flame. Ignition delay in this regime is therefore largely due to the droplet heating

time. For smaller droplets igniting in this regime, the heating time shortens, and has been shown to be generally independent of ambient temperature.

As initial droplet size is continually reduced (or for increasing fuel volatility), a relatively short time is required to raise the temperature of the liquid droplet surface to near boiling point. In addition, mass transfer rates, which scale inversely with droplet size increase and compete with kinetic rates. At a sufficiently small initial droplet size (dependent on propellant characteristics and ambient conditions), mass transfer rates becomes faster than reaction rates, and a transition occurs into a kinetically-controlled regime where the reactions times are relatively longer than diffusion times [23]. For small droplets of fuels with relatively low volatility, ignition delay in the kinetically-controlled regime has been experimentally shown to increase as droplet size decreases. Existing experimental results also show that for sufficiently low values of ambient temperature and/or pressure, oxidizer mass fraction, droplet size, or initial droplet surface temperature, ignition may not take place (infinite ignition delay) [25]. Examples of kinetically-controlled processes include ignition, explosion, extinction and flame quenching [26]. For some fuels and ambient conditions in the kinetically-controlled regime, small droplets will evaporate completely without igniting due to the higher rates of heat loss versus net heat generation from chemical reactions [27].

Analytically, two ignition criteria have been defined in literature to determine when a droplet immersed in given conditions has ignited. The more widely accepted criterion is thermal-based, where it is agreed that the competing rates of heat supply by chemical reaction and rate of heat loss by diffusion determine whether or not a droplet will ignite. The second criterion is based on the concentration of a selected crucial chain-branching intermediate specie. When this specie reaches a critical value in the vicinity of the droplet, ignition is then said to have occurred. The rate of formation of this specie at a point in the vicinity of the droplet would then be dependent on the temperature and the mixture ratio history [6]. The focus in this work is on the thermal-based ignition criterion which involves the competing rates of heat supply and heat loss, characterized by a dimensionless number known as the Damköhler number (Da).

Analyses of the ignition of fuel droplets in hot gaseous media typically involve the use of the Damköhler (Da) number to describe the ignition and burning regime for a given set of droplet and

ambient conditions. The Da number is defined as the ratio between the time scales for the diffusion and reaction processes, i.e.:

$$Da = \frac{\text{Diffusion time}}{\text{Reaction time}} = \frac{\text{Reaction rate}}{\text{Diffusion rate}} \tag{1}$$

As initial droplet size decreases, diffusion rates increase dramatically and so the diffusion time becomes much shorter compared to chemical reaction time. The   and the combustion mode becomes kinetically-controlled [27]. A unity Da number is therefore associated with the change between a kinetically-controlled regime and a diffusion-controlled regime.

In a study on the ignition characteristics of blended fuels, Takei et. al [23] studied n-hexadecane, n-heptane, and mixtures of both fuels in high ambient temperatures between 950 K and 1023 K at atmospheric pressure. The two fuels were chosen based on their different volatilities, with the more volatile n-heptane having a boiling point of 317 K, and the less volatile n-hexadecane having a boiling point of 560 K. Results showed that for the same ambient conditions and droplet size range (~0.4 mm to ~1.4 mm), n-heptane exhibited a decrease in ignition delay with an increase in droplet size, while n-hexadecane showed the opposite trend as shown in **Error! Reference source not found.**.
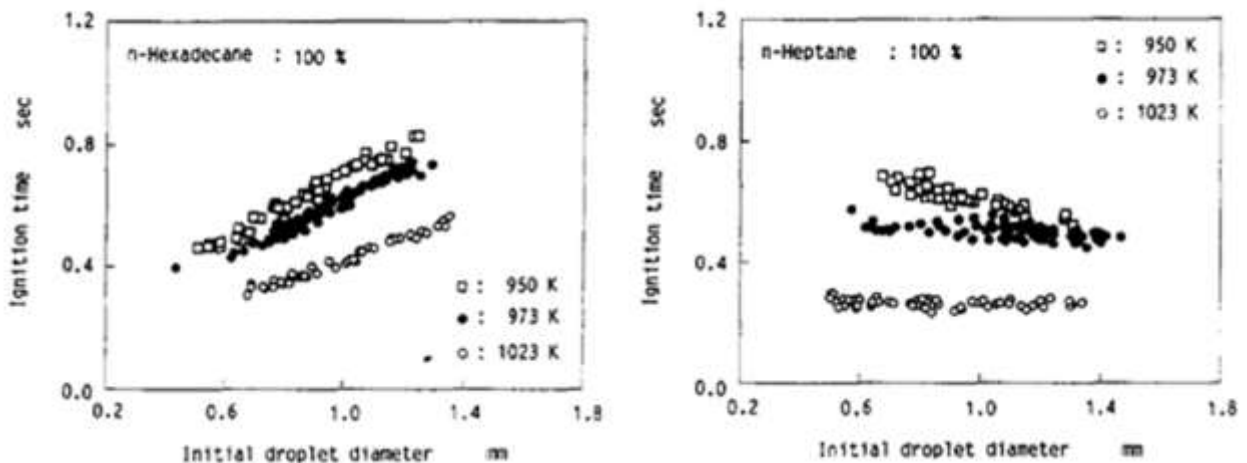
Figure 2. Variation of ignition delay (sec) with initial droplet diameter (mm) for n-hexadecane (left) and n-heptane (right) [23]

The authors describe the n-hexadecane results as ignition in the diffusion-controlled regime, postulating that for a sufficiently small initial droplet size, the mass transfer rate would be large enough, and the reaction time would lengthen so that the ignition delay would begin to increase. However, this hypothesis unachievable experimentally due to the sudden increase to infinity of the ignition delay (ignition delay did not occur) as initial droplet size was decreased. Consequently, for n-hexadecane, the smallest droplet size that could ignite was the optimum droplet size for minimum ignition delay.

For the same ambient conditions and droplet size range, n-heptane was shown to ignite entirely in the kinetically-controlled regime. Ignition delay decreases as initial droplet size increased, however this effect became less significant at higher temperatures. These results showed that for n-heptane, the optimum initial droplet size for minimum ignition delay was larger than that of n-hexadecane.

2.2.2.2 Combustion in the Kinetically-controlled and Diffusion-controlled Regimes

In the diffusion-controlled regime, the burning rate has been shown both computationally and experimentally to be constant after a short transient period as predicted by the D^2 law. In the kinetically-controlled regime however, the burning rate may vary greatly.

In the kinetically-controlled regime, temperature and species distributions have enough time to smooth out any spatial non-uniformities due to high diffusion rates (rates of supply of fuel and oxidizer by flow, diffusion or mixing) compared to chemical reaction rates (rates of consumption of the fuel and oxidizer) [26]. A depiction of the difference between kinetically-controlled and diffusion-controlled burning is shown in Figure 3. In this figure, A and B represent the fuel and oxidizer, respectively, C represents the products, all in gas phase in a combustion chamber, and T refers to a uniform temperature [24]. Due to faster diffusion or 'mixing' times for fuel and oxidizer in the kinetically-controlled regime, the flame has a larger reaction space, analogous to flame-zone broadening in droplet burning. In the diffusion-controlled regime, there is a flame at a distinct location. The flame sheet approximation for the diffusion-controlled regime therefore breaks down below a certain initial droplet size,

accompanied by a reduction in flame temperature as kinetics start to play a more significant role [27].
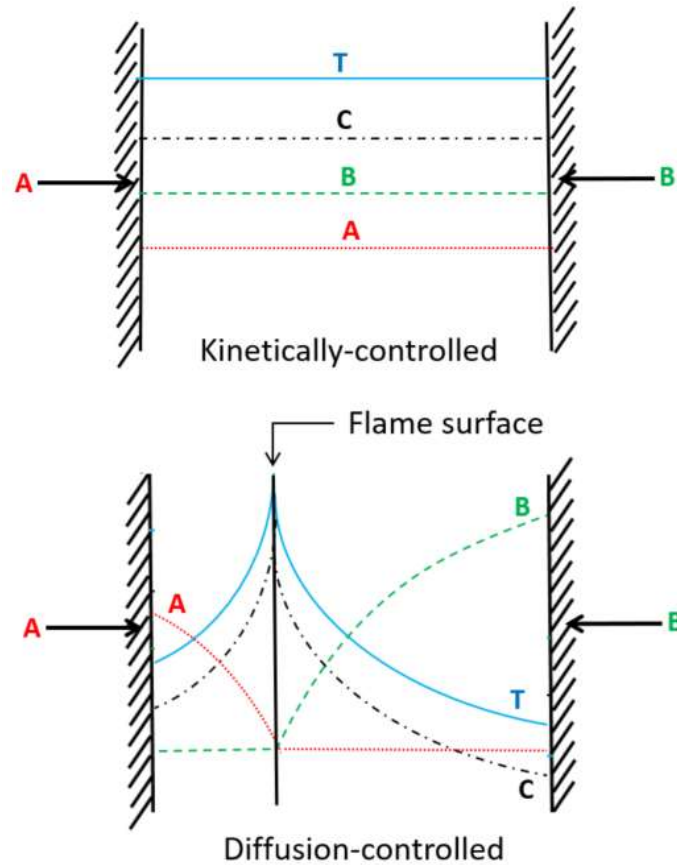
Figure 3. Depictions of combustion in kinetically-controlled and diffusion-controlled regimes [24]

Beginning with a discussion on experimental techniques used in studies investigating ignition and combustion of fuel droplets, the following sections describe and compare studies on ignition of both bipropellant and monopropellant droplets in hot oxidizing gaseous environments.

2.2.3   Experimental Techniques for Droplet Ignition and Combustion Studies

To characterize ignition characteristics of droplets, experimental studies involve the determination of ignition delay, location of initial flame front, and dependence of these parameters on ambient conditions at time of ignition, among other characteristics [28].

Techniques that have been used to experimentally investigate droplet ignition and combustion phenomenon generally fall into one of two categories, the suspended-droplet technique and the free-falling droplet technique.

In the suspended-droplet technique, a droplet is typically suspended from a thermocouple, thin fiber or the needle of a syringe. The suspended droplet is then exposed to a hot, gaseous environment. The hot ambient gases are supplied by a heat source such as a furnace, the combustion gases of a flat flame burner, or heat from a nickel-chrome (nichrome) wire depending on the data of interest. To simulate a suspended droplet being suddenly introduced into the hot gaseous environment, pneumatic methods have been employed to either rapidly push the heat source into position beneath the suspended droplet or to withdraw a flame shield initially insulating he droplet from the hot gases. In some experiments, issues of liquid adherence to the outer surface of a hollow needle make droplet deployment difficult. In these instances, some investigators coat the outer surface of stainless steel needles with a liquid-repelling substance such as silicone grease to make droplets more reproducible [29].

In contrast, in the free-falling droplet technique individual droplets or a train of droplets are generated from an electrically actuated droplet generating device and then fall through a gaseous medium. The free-falling droplet generation technique eliminates any disturbance caused by the presence of a supporting fiber, however it introduces forced convection which may significantly alter the ignition and combustion characteristics. For instance, convection may increase the transportation rates surrounding a droplet and thus decrease its ignition delay, or cause a shift in the flame location from an envelope flame surrounding the droplet to a wake flame [13].

Another experimental technique that is less common in the literature is the porous-sphere technique. In this approach, the liquid fuel is supplied to the inside of a porous sphere and then forced radially outward where it burns as it reaches the surface of the sphere. For this method, cooling techniques may be necessary to prevent pre-heating of the fuel due to the presence of surrounding hot gases. Limitations of the porous-sphere technique include large surface area requirements (thus limiting the droplet size range that can be tested using this method), excessive heat transfer to the porous spheres, and fixed droplet size during burning [29].

Optical techniques used to detect ignition of a droplet including high speed imaging and chemiluminescence signal detection. High speed cameras are used to detect ignition by visualizing flame establishment around the droplet and for tracking the droplet diameter history. High speed cameras in conjunction with intensifiers and appropriate optical filters have been used for detecting OH* and CH* chemiluminescence and the point of droplet ignition is then identified as a sudden increase in the emission of these species.

2.3 Effect of Droplet Size, Fuel Type and Ambient Conditions on Droplet Ignition and Combustion

2.3.1 Effect of Initial Droplet Diameter

The trends of ignition delay with droplet size vary in the literature for hydrocarbon and alcohol-based fuels. Depending on the fuel volatility, ambient temperature and initial droplet size, fuel droplets may react with gaseous oxidizing atmospheres in either the kinetically-controlled or diffusion-controlled regime. In the diffusion-controlled regime, an increase in initial droplet diameter causes an increase in the ignition delay. The increase in ignition delay with droplet diameter is attributed to the longer time required to heat up the surface layers of relatively larger droplets for vaporization [30]. In the kinetically-controlled regime, droplets may either fail to ignite or exhibit a decrease in ignition delay with increasing droplet size. In both regimes, there exists a critical droplet diameter below which ignition will not occur.

In a study on evaporation and ignition delay of fuel droplets, Nishiwaki [31] tested cetane and alpha-methyl napthalene droplets between 500 µm and 1.5 mm in ambient temperatures between 400 ℃ and 716 ℃. Experimental results showed that for alpha-methyl naphthalene at lower temperatures (below 700 ℃), ignition delay increased with increasing droplet diameter. However, at higher temperatures (above 700 ℃), they found that for the same range of droplet sizes, there was a certain droplet size (~1 mm) below which ignition delay began to slightly increase. No explanation for this was provided for this observation. Succeeding investigations using a variety of fuels and ambient conditions would reveal the underlying physics driving the changes observed in the droplet ignition and combustion behavior.

Some of the most commonly used experimental data in models on hydrocarbon fuel droplet ignition was obtained by Faeth and Olson [6]. The droplet diameters studied were between ~0.7 mm and ~1.7 mm and the ambient pressure was maintained at 1 atm. The experiments were conducted in both zero-gravity and normal gravity environments. The zero-gravity environment was included to satisfy the assumption of a spherically symmetric droplet to validate the neglect of convection effects. As shown in Figure 4, tests conducted for n-hexadecane droplets at ~950 K showed an increase in ignition delay with an increase in initial droplet size. Saitoh et al. [32] attributed this increase in ignition delay to the increased heating time required for large diameters and a high fuel boiling point. Takei et al. [23] later confirmed that this behavior corresponded to ignition in the diffusion-controlled regime.
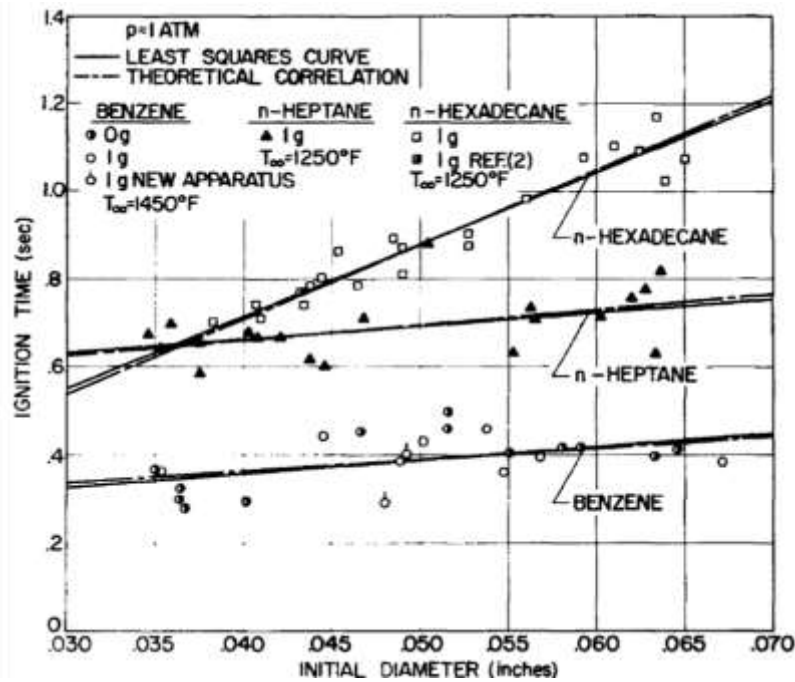
Figure 4. Ignition delay variation (sec) with initial droplet diameter (inches) for benzene, n-heptane, and n-hexadecane droplets [6]

In contrast, in a droplet ignition study of hydrocarbon droplets in similar ambient conditions, Bergeron and Hallet [13] observed a more modest effect of initial droplet diameter (between 1 mm and 1.6 mm) on ignition delay for n-heptane and n-hexadecane, with an even weaker effect for fuels with low boiling points such as cyclohexane and benzene. Similar conclusions were reached by Kadota et al. [33] in their investigation on n-heptane, n-dodecane and n-hexadecane droplets

reacting at elevated pressures. For n-heptane droplet sizes between ~1.7 mm and 2 mm reacting in 400℃ air at 10 atg (9 atm) ambient pressure, Kadota et. al found no appreciable effect of initial droplet size on ignition delay, which remained on average approximately 0.5 s. Wood and Rosser [25] also found that ignition delay was independent of droplet size if the droplets were large enough to ignite at all. For n-heptane droplets between 0.3 mm and 0.7 mm, Long and Grens [28] observed ignition delays ranging from 22 ms in 860℃ air to greater than 2 s in 500℃ air. However, no apparent effect of droplet size was observed, and no qualitative discussion was provided for this observation.

As discussed above, Bergeron and Hallet [13] found that the ignition delay for the fuel with the higher boiling point (n-hexadecane, 560 K) had a stronger dependence on initial droplet diameter than fuels with lower boiling points (benzene, 353 K and n-heptane, 371 K). However, these findings are inconsistent with conclusions reached by other investigators. Saitoh et. al [32] studied ignition delay of n-heptane droplets with diameters between ~0.7 mm and 2.5 mm in varying ambient temperatures between 973 K and 1073 K. As shown in Figure 5, they found that a droplet diameter range exists near the ignitable limit where the ignition delay increases as droplet diameter decreases. This was attributed to the decrease in local Da number, rendering the kinetic effects dominant in this region. At the ignitable limit, the droplet size is too small, and it vaporizes completely without ignition occurring. This critical droplet size is often correlated with a critical Da number at known ambient conditions. For large droplet sizes, the authors postulated that ignition times would begin to increase again as a result of the larger droplet requiring more heat-up time. For large droplets, the increase in ignition delay is primarily due to the larger heat capacity of the droplet requiring relatively longer times for surface temperature to achieve a temperature close to the boiling point of the fuel [34].
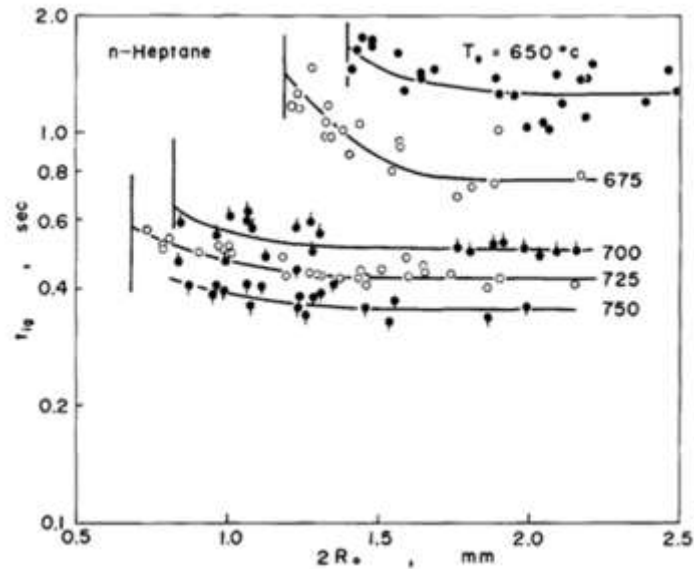
Figure 5. Ignition delay (sec) variation with initial droplet diameter (mm) for n-heptane droplets at various ambient temperatures (degrees Celsius) at P = 1 atm [32]

Nakanishi et. al [34] investigated the ignition behavior of n-heptane and n-hexadecane droplets between 350 µm and 1.4 mm in high-pressure and high-temperature environments. Results showed that at low pressure, ignition delay for both fuels initially decreased with an increase in initial droplet diameter, and then began to increase pass a critical droplet diameter, an observation that disappeared at high pressures. In the range of droplet diameters between 120 µm and 180 µm, Ogasawara et. al [33] observed that ignition delay of tetralin droplets apparently decreased as initial droplet diameter increased. However, since a larger droplet entered the hot environment faster than a smaller one, therefore increasing heat transfer and diffusion rates due to faster falling velocity, this conclusion could not be made with certainty. Sangiovanni and Kesten [35] observed that in the droplet size range between 200 µm and 300 µm, ignition delay for alcohol droplets reacting in combustion gases between 1240 K and 1680 K decreased slightly with an increase in droplet size. This effect however became less significant as temperature increased in that range.

The decrease of ignition delay with increasing droplet size was more pronounced in observations made by Makino and Fukada [36] in their study on the ignition and combustion of single falling sodium droplets. Sodium was heated to 400 K and ejected into a combustion chamber with an ambient oxygen mass fraction of 0.23. Droplet sizes were varied between 0.6 mm and 6 mm and

the ambient temperature was maintained at 723 K. Results showed that the ignition delay first decreased gradually with a decrease in initial droplet size, then increased sharply as shown in Figure 6. They attributed this behavior to the heat loss from the droplet surface increasing the time it takes the droplet to heat up for sufficient vaporization to take place before ignition can occur.
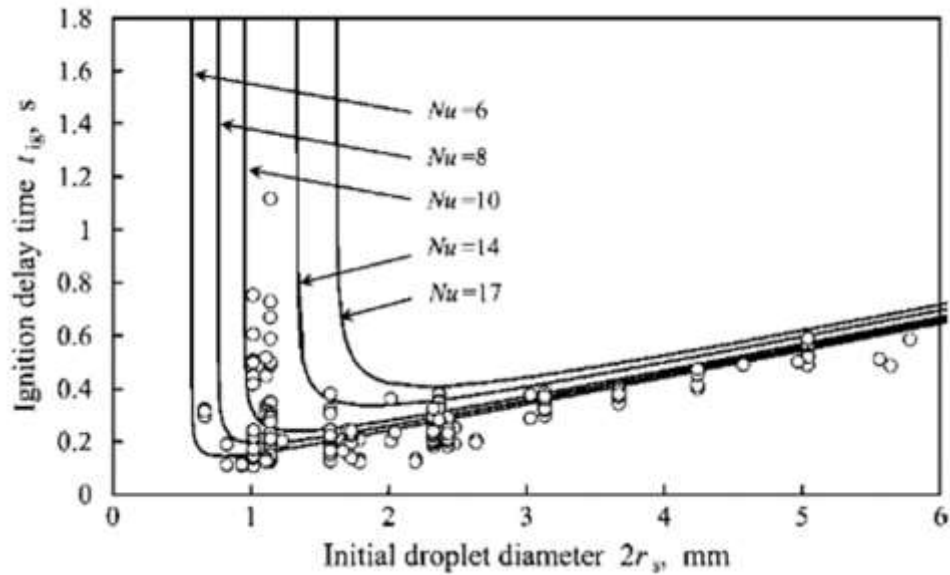
Figure 6. Ignition delay (sec) vs. initial droplet diameter (mm) sodium droplets [36]

As droplet size decreases for any set of ambient conditions and fuel type, there exists a critical diameter below which ignition will fail to occur. Faeth [7] attributed the presence of a critical diameter for ignition to the fact that there is a certain total time necessary for chemical reaction to produce a sufficient quantity of a reaction intermediate to lead to ignition. Ignition would then fail to occur due to the droplet evaporating completely before that critical time is reached due to its small size. The vapor velocity leaving the surface of the droplet is inversely proportional to the initial droplet size. Therefore, the smaller the droplet, the greater the vapor velocity, increasing convective heat loss from the reaction zone. This reduces the temperature at the reaction zone which consequently slows the progress of the reaction. For sufficiently small droplets, the droplet completely evaporates before the reaction has sufficiently progressed and therefore ignition does not take place [13]. Nakanishi [34] noted that for sufficiently small droplets, the evaporation flux is so high that the chemical reaction rate cannot consume the fuel fast enough to produce sufficient heat to lead to ignition.

In addition to ignition delay, the droplet burning rate and flame structure have also been found to depend on the initial droplet diameter. While the classical D^2 law quite accurately predicts that the droplet burning rate and flame stand-off ratio remain constant throughout the droplet lifetime for relatively large droplets, experiments have shown that in the kinetically-controlled regime, burning rate and flame stand-off ratio are time dependent with increasing unsteadiness as droplet size decreases [27].

Some of the smallest suspended droplets were investigated by Monaghan et. al [37] in their study on the effects of initial droplet diameter on the combustion characteristics. Droplets with diameters between 150 µm and 2 mm were suspended on fine silica fibers and ignited using an electric spark. Results showed that the initial droplet diameter had a significant effect on combustion characteristics. The authors found that the burning rate was not only a function of the instantaneous droplet diameter but was also a function of the initial diameter. They postulated that an initially larger droplet absorbed more heat during its lifetime and was hotter, and therefore burned more quickly in the later stages than an initially smaller droplet. This scenario was compared to a droplet with the same instantaneous droplet diameter which was initially much smaller and was described in this way: "…the two small drops compared are in effect a hot drop, resulting from a drop initially large, and a small cold drop. [37]". Figure 7 shows the results for burning rate vs. initial droplet diameter obtained by Monaghan et. al for various fuels.
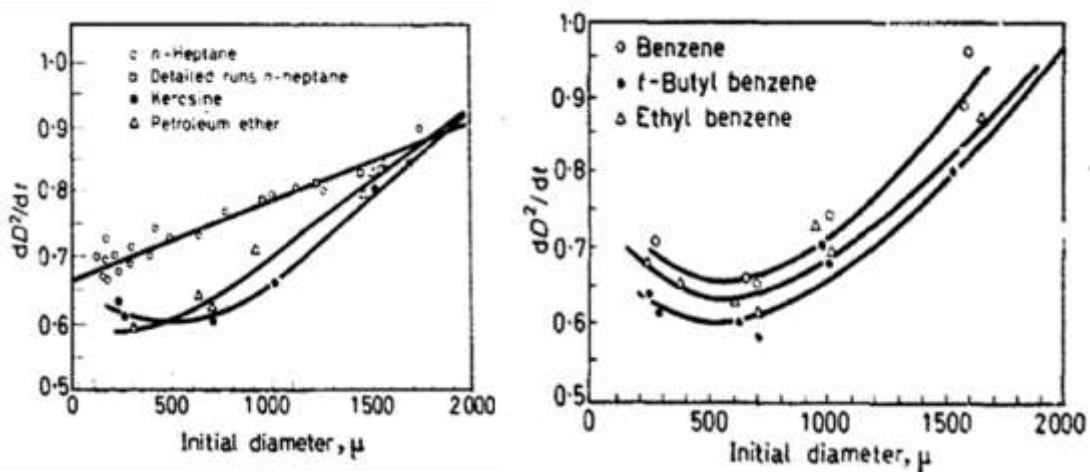
Figure 7. Effect of initial droplet diameter (µm) on (or droplet burning rate) for various fuels [37]

For all fuels, Monaghan et al. [37] observed a decrease in burning rate with a decrease in initial diameter over the droplet size range tested. For kerosene and the benzenes, however, there was a critical diameter below which burning rates began to increase with further decrease in initial droplet diameter. No qualitative explanation was offered for this observed trend, however the differences in burning rates for the different fuels were attributed to their boiling points or the amount of heat required to vaporize each of the fuels.

Monaghan et al. [37] also found that heat transfer by natural convection had a more significant effect on the combustion characteristics of larger droplets compared to smaller droplets. Firstly, the flame shape distortion due to natural convection effects was evident. In addition, the presence of natural convection increased burning rates of 1 mm droplets by approximately 40% when compared to burning rates obtained in microgravity conditions. This effect was observed to decrease for smaller droplet sizes. Due to a smaller volume of combustion products surrounding smaller droplets, flames were observed to be approximately spherical and concentric with the droplets, resulting in slower burning rates for droplets reacting in quiescent atmospheres.

In comparison, Hara and Kumagai found that the effect of initial diameter on burning rates was less pronounced for droplets in the range 70 µm to 400 µm in diameter. To elucidate the effect of initial diameter on the combustion of a single droplet, Hara and Kumagai [38] ignited 70 µm and 400 µm n-heptane droplets in normal gravity and microgravity conditions, respectively, using an electric spark. The authors concluded that, for the larger (400 µm) droplet, the variation of the square of the droplet diameter was consistent with the D^2 law after a short, transient heat up period. For the smaller droplets (70 µm), the variation of the square of the droplet diameter was consistent with the D^2 law until a certain point when the burning rate was observed to decrease due to extinction. The authors also observed burnout (burning throughout the droplet lifetime until it disappears) for the large droplet reacting in micro-gravity, while for the 70 µm droplets reacting in normal gravity, droplet extinction was observed and an extinction diameter measured.

Results from numerical modeling of droplet combustion by Awasthi [27] also showed an influence of initial droplet size on the flame stand-off ratio. The model predicted that as droplet size

decreased the flame stand-off ratio would increase. The increase in flame stand-off ratio with decreasing droplet size is attributed to the higher fuel accumulation between the droplet surface and the flame. Initially, a small amount of vapor exists in the gas phase near the droplet surface and the flame is therefore positioned much closer to the droplet surface in order to achieve stoichiometric burning. The proximity of the flame increases the rate of fuel droplet evaporation, which in turn increases the concentration of the fuel between the droplet surface and the flame, causing the flame to move further away from the droplet. In the same numerical study, another effect of droplet size found was that the initial transient or heat up time is shorter for smaller droplets, however its relative length compared to the droplet lifetime increased with decreasing droplet size. In addition, unlike larger droplets where temporal changes in droplet diameter history, flame temperature and flame stand-off ratio were almost instantaneous at the point of droplet extinction, smaller droplets exhibited a more gradual change in these parameters, making it difficult to characterize extinction if it occurred [27].

2.3.2   Effect of Fuel Type

Differences in ignition delay for similar droplet sizes of different fuels is largely attributed to differences in the fuel boiling points. A common comparison that has been made in the literature is between n-hexadecane and n-heptane. Table 1 shows the differences in properties between the two fuels. A low boiling point is characteristic of high-volatility fuels while the opposite is true for less volatile fuels.

Table 1. Selected Properties of n-heptane and n-hexadecane

	n-heptane	n-hexadecane
Formula	C_7H_{16}	$C_{16}H_{34}$
Boiling point	98 ℃	287 ℃
Vapor pressure	5.33 kPa (20 ℃)	< 0.1 kPa (20 ℃)
Density	0.67 g/cm^3	0.77 g/cm^3

The fuel volatility is a significant factor in determining the droplet ignition and burning regimes (diffusion-controlled vs. kinetically-controlled) for a given set of ambient conditions. A detailed discussion on ignition and burning regimes is given in Section 2.2.2. **Error! Reference source not found.** illustrates the difference in ignition behavior of n-hexadecane and n-heptane droplets, obtained from experimental results by Takei et. al [23]. For pure n-hexadecane droplets, an

increase in ignition delay was observed with increasing droplet sizes between 0.6 mm and 1.4 mm, in ambient temperatures between 950 K and 1023 K. In the same conditions and droplet size range, results for n-heptane showed a decrease in ignition delay with an increase in droplet diameter. Figure 8 illustrates the general trends for ignition time vs. initial droplet diameter for fuels with varying degrees of volatility.
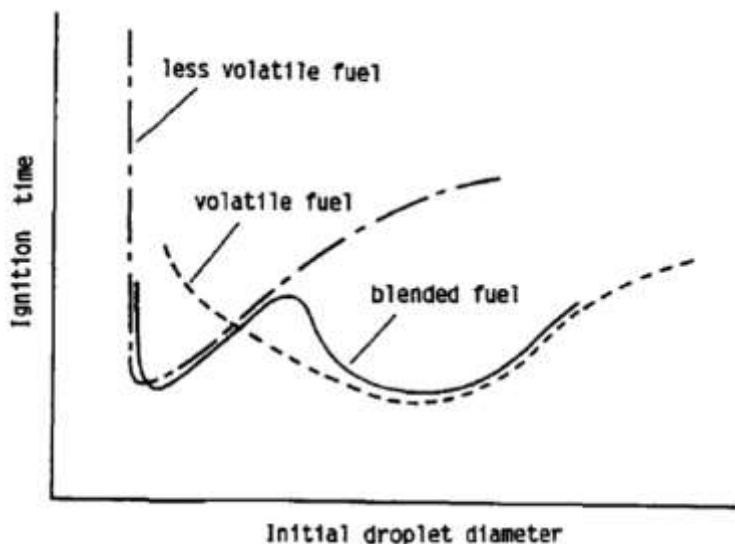
Figure 8. Schematic of ignition delay variation with droplet diameter for different fuels with varying degrees of volatility [23]

For low boiling point fuels, the droplet heat-up process is rapid, and a significant amount of fuel vapor is produced at relatively low temperatures, thus reactions begin early. For less volatile fuels (higher boiling points), a longer period of heating is required to bring the droplet surface to near boiling point for vapor production. Ignition delays are therefore higher in general for less volatile fuels due to the longer transient heat-up period [13].

In an investigation of the ignition delay of fuel droplets, Wang et. al [39] observed that for free-falling 300 µm and 400 µm n-heptane and n-hexadecane droplets in high-temperature and high-pressure environments, the ignition delays were consistently lower for the more volatile n-heptane due to the significantly lower boiling point. Comparison of droplet ignition experiments by Nakanishi et. al [34] between n-heptane and n-hexadecane revealed that the ignitable droplet diameter limit was larger for n-heptane for droplets of comparable sizes. Kadota et. al [40] found that ignition delay decreased rapidly with an increase in ambient temperature between 220℃ and

700°C for n-heptane. Comparing n-heptane to n-hexadecane, and n-dodecane, a trend was found where an increase in number of carbon atoms in the fuel molecule caused an increase in ignition delay for a fixed ambient temperature and pressure. However, the authors attributed this trend to the increase in volatility of the fuels and consequently, the rate of evaporation.

2.3.3   Effect of Ambient Temperature

In droplet ignition and combustion experiments, high ambient temperature environments (between 600 K and 1700 K) are provided by furnaces, resistance wires, or combustion gases from a burner. The effect of ambient temperature on droplet ignition and combustion is consistent across the literature, where an increase in ambient temperature results in a significant decrease in ignition delay. In addition, high temperatures decrease the critical size below which ignition will not occur for a given fuel. This effect has been attributed to the increased reactivity of the propellants at higher temperatures.

In a study on the ignition of fuel micro-droplets, Sangiovanni and Kesten [35] used a droplet generator to generate a stream of 200 µm and 300 µm furfuryl and butyl alcohol monodisperse droplets into a hot gaseous environment (1240 K – 1680 K). The spacing between the droplets was sufficiently large to neglect the effects of droplet interaction on ignition. As shown in Figure 9, for both fuels, a rapid increase in ignition delay was observed as ambient temperature was reduced. Similarly, a study on the ignition and combustion of single tetralin micro-droplets with diameters between ~120 µm and 180 µm showed a drastic decrease in ignition delay with a rise in ambient temperature from 800°C and 1000°C.
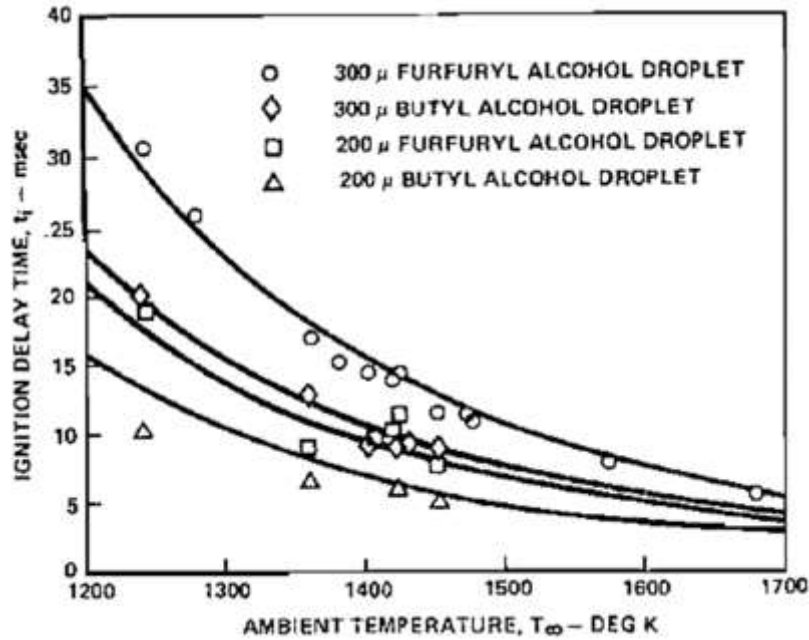
Figure 9. Ignition delay (ms) variation with ambient temperature (K) for 200 µm and 300 µm furfuryl and butyl alcohol droplets [35]

This observation is also consistent with results for larger droplets on the order of 1 mm. Faeth and Olson [6] designed an experiment to determine the effects of droplet size, ambient pressure, temperature and fuel type on the ignition delay of hydrocarbon droplets. N-heptane, n-hexadecane, benzene and iso-octane droplets with sizes ranging between 0.7 mm and 1.7 mm were suspended on a fine glass filament and exposed to hot ambient gases with temperatures between 700°C and 870°C. Micro-gravity conditions were imposed using a drop tower to eliminate the effects of natural convection. Faeth and Olson's results showed that ignition delay increased with a decrease in ambient gas temperature. In addition, for a fixed initial diameter size, there existed a critical ambient gas temperature below which ignition would not occur as shown in Figure 10.
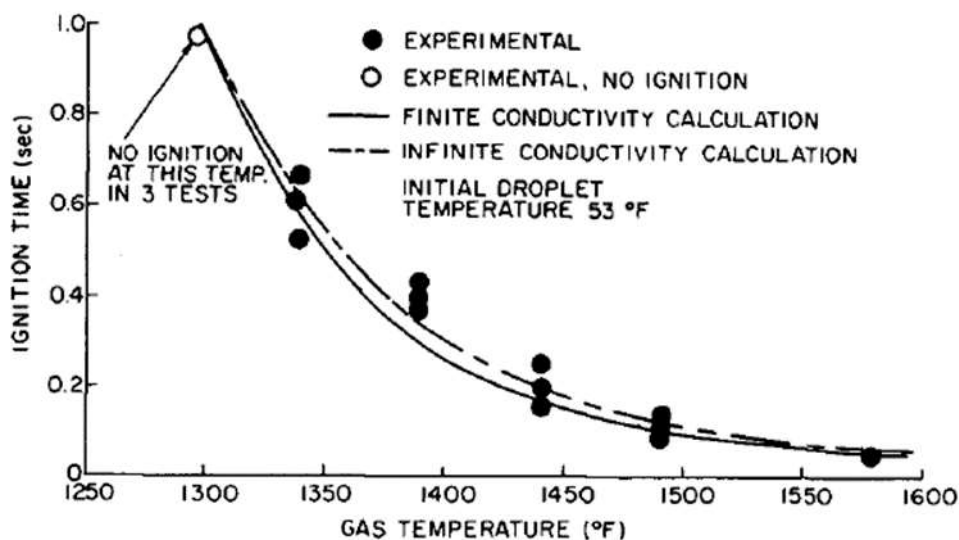
Figure 10. Variation of ignition delay (sec) with ambient gas temperature (^{0}F) [6]

For ~1.4 mm iso-octane droplets ignited at 1atm, Faeth [7] observed a drastic decrease in ignition delay as ambient temperature increased in the range ~704℃ to 871℃. At the lower end of the temperature range, this decrease in ignition delay was drastic. However, as temperatures increased, the ignition time became less sensitive to variations in the ambient gas temperature. The author attributed this to the fact that at lower temperatures, kinetic effects, which are quite sensitive to temperature changes, became dominant [7]. Goodger and Eissa [30] attributed this observation to the idea that at lower temperatures, less energy is available to initiate and sustain chain reactions, resulting in longer ignition delays.

As previously mentioned, another effect of elevated temperatures that is consistently observed across different investigations is the increased ignitability of droplets for a given set of ambient conditions. Data for some of the smallest droplet sizes considered in the literature was obtained by Wood and Rosser [41] in their study on the ignition and combustion of single n-hexadecane droplets. The size history, ignition delay and loci of droplets with initial diameters between 100 µm and 300 µm were obtained by allowing the droplets to fall freely into a furnace with ambient temperatures ranging between 863 K and 1013 K. Figure 11 shows the ignitability limits obtained for n-hexadecane droplets in air, where the dark circles represent droplets that ignited. Results showed that for a given ambient temperature, there exists a critical droplet size below which

ignition did not occur. This critical droplet diameter was smaller for higher ambient temperatures. Faeth attributed this to the fact there exists a certain amount of time that must elapse for chemical reactions to produce sufficient amounts of intermediate species and heat before ignition can take place. This 'critical time' becomes shorter at higher temperatures, because the reaction progresses at a much faster rate, thus allowing smaller droplets to ignite [7].
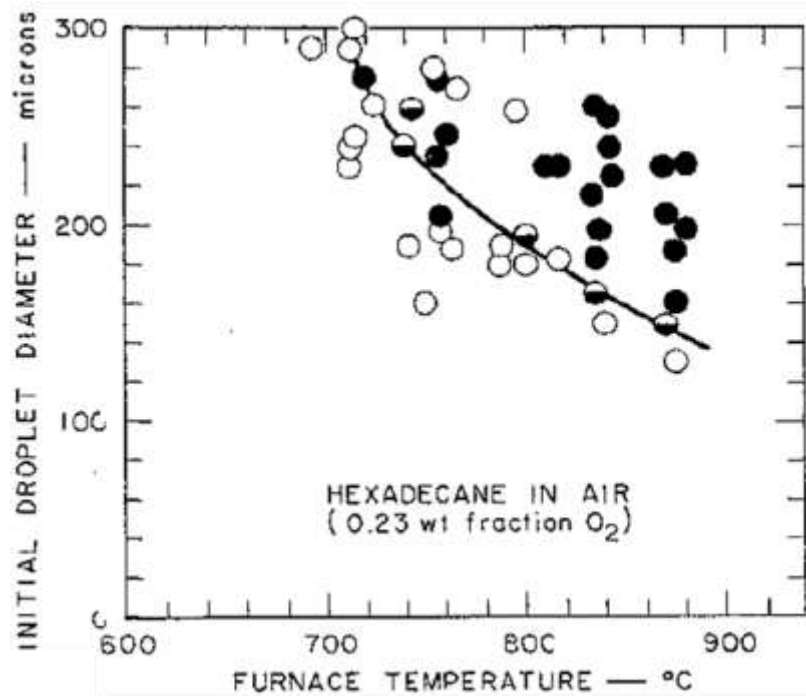
Figure 11. Characteristic ignition curves for n-hexadecane droplets in air [25]

Experimental data on the variation of ignition delay with temperature have been useful in obtaining reaction rate constants and effective activation energies for the systems under study. These values can then be used in semi-theoretical models to predict ignition delay and ignitability based on given conditions. Consider the Arrhenius equation for the reaction rate :

$$k = A'\exp(-\frac{E}{R_u T})$$ (2)

where A' is the pre-exponential factor, E is the activation energy, R_u is the universal gas constant and T is the temperature. If we make the assumption that the ignition delay, τ, represents the time

it takes for a fraction of the reaction to occur [42], we can reason that $\tau \propto 1/k$, where an increase in the reaction rate results in a shorter ignition delay time. We can then write Equation **Error! Reference source not found.**) in terms of ignition delay to obtain:

$$\tau = A^{"} \exp\left(\frac{E}{R_u T}\right)$$
(3)

Taking the logarithmic variation of Equation (3), we can plot the logarithm of ignition delay vs. the reciprocal of ambient temperature. The slope of this line then represents an activation temperature, or , where represents an effective activation energy. This method was used to obtain activation energies and pre-exponential factors used in theoretical comparisons made by several investigators of the quasi-steady droplet ignition (QSDI) model originally formulated by Law [15] with existing experimental ignition delay data.

2.3.4   Effect of Pressure

The effect of pressure on droplet ignition has been studied by several investigators, with pressures ranging between from 1 atm to 40 atm. In general, increasing pressure has been shown to shorten chemical ignition delay time by increasing the reactivity of fuel and oxidizer combinations.

Wang et al. [39] studied the effect of pressure on ignition delay of 300-400 µm n-heptane and n-hexadecane droplets falling into a high-temperature, high-pressure oxidizing atmosphere. Ambient temperature ranged between room temperature and 1000℃ and ambient pressure was varied between atmospheric pressure and 3 atm. Results showed a decrease in ignition delay with increasing pressure. However, this effect decreased as pressure increased. The authors explained these trends by comparing the competing influence of pressure on chemical reactivity, liquid fuel boiling point, and heat transfer rate. At lower pressures, the effect of increasing pressure was the drastic reduction of ignition delay, and this behavior resulted from an accompanying drastic increase in chemical activity. As pressure increases, the rate of decrease in ignition delay became slower as the influence of pressure on prolonging the physical delay through its tendency to increase liquid fuel boiling point (and hence heating time) became more dominant, overshadowing its tendency to shorten it through increasing the heat transfer rate. In addition, the rate of decrease of ignition delay with pressure for n-heptane was lower for higher temperatures. It was also

observed that the effect of pressure was greater for fuels with higher boiling points. In comparisons between n-hexadecane and n-heptane at a fixed temperature, the effect of pressure was much greater for n-hexadecane, mainly due to the influence of droplet heating. For fuels with higher boiling points (e.g n-hexadecane), a longer droplet-heating time is required before ignition can occur. Similar trends have been observed by other investigators [25, 29, 37].

In a study on ignition delays of droplets at high pressure and high temperature, Nakanishi et al. [34] observed a region of increasing in ignition delay with decreasing droplet diameters at atmospheric pressure and ambient temperatures of 850 K for n-hexadecane droplets as shown in Figure 12. This trend has been consistently observed for n-heptane [23], [32], but the opposite has been observed for n-hexadecane above this temperature at atmospheric pressure [23]. The data points to the extreme left represent the minimum droplet size below which ignition was not observed, or the 'critical droplet size'. As pressure was increased, the region of increasing ignition delay with decreasing initial droplet size disappeared and a positive slope of ignition delay versus initial droplet diameter was obtained. Similar observations were made for n-heptane at elevated temperatures. The authors attributed this ignition delay trend reversal with increasing pressures to the increase of the Da number with pressure. This suggested that an increase in pressure favors transition from a kinetically-controlled regime to a diffusion-controlled regime. Da number was shown to be directly proportional to the square of the pressure through the direct proportionality of mass transfer time to pressure and the inverse proportionality of chemical reaction time to pressure. The authors also concluded that at high pressures, the reaction time does not play a significant role in the overall ignition delay time.
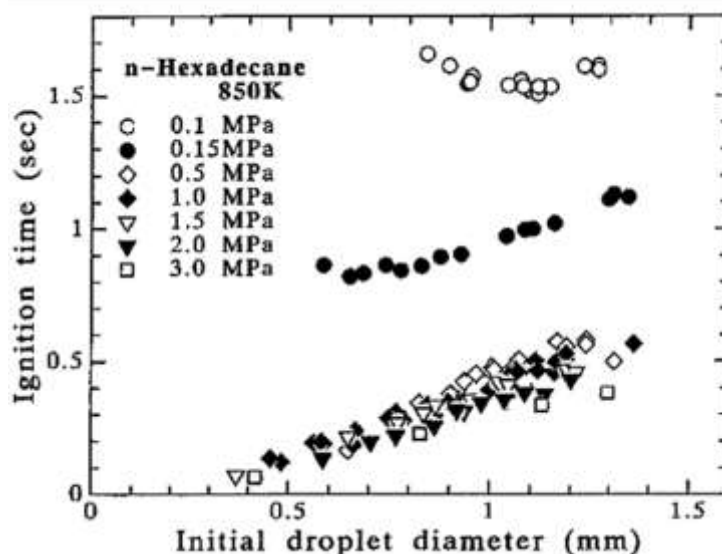
Figure 12. Variation of n-hexadecane ignition delay (ms) with pressure (atm) for D_o = 384 µm at various temperatures [39]

Nakanishi and co-workers also observed that increasing ambient pressure caused a decrease in the critical droplet diameters below which ignition did not occur as shown in Figure 13. The area to the right of the curves corresponds to ignitable droplets and conditions. As ambient pressure increases, the minimum droplet diameter for ignition decreases. At this critical diameter, ignition delay went to infinity and ignition did not take place, an observation attributed to the competing rates of mass transfer and chemical kinetics as discussed previously (Section 2.2.2.1). Comparisons were also made between n-heptane and n-hexadecane and the critical diameters for n-heptane were observed to be larger than for n-hexadecane. This trend was again attributed to the larger mass-flux of n-heptane compared to n-hexadecane as a result of the different boiling points. In addition, the temperature of the fuel vapor from the droplet surface is higher for n-hexadecane due to its higher boiling point, while n-heptane fuel vapor is relatively cold and thus requires more time for reaction to occur.
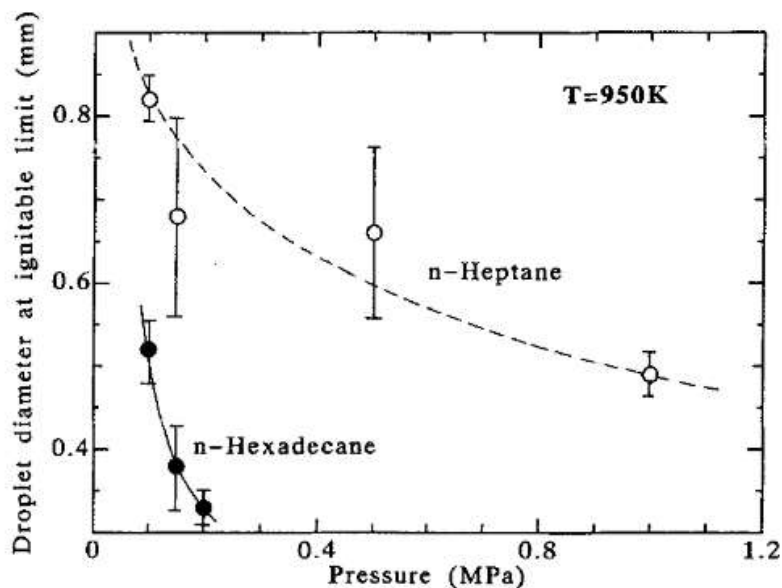
Figure 13. Limiting diameter (mm) variation with pressure (MPa) for n-heptane and
n-hexadecane [34]

2.3.5   Effect of Ambient Oxidizer Concentration

Varying observations have been made on the effect of ambient oxidizer concentration on ignition characteristics and ignition delay. However, the majority of investigators in the literature are in agreement that increasing the ambient oxidizer mass or mole fraction results in a reduction in ignition delay time due to increased chemical reaction rate. However, this effect decreases at very high oxidizer concentrations.

Wang et. al [39] studied the effect of ambient oxygen concentration on ignition of free-falling n-hexadecane droplets with diameters of 300-400 µm. The oxygen concentration was varied between 21% and 51% by volume. Experimental results showed that ignition delay decreased as oxygen concentration increased, however at higher concentrations this effect was less pronounced. The reduced sensitivity of ignition delay to oxidizer concentration in higher oxygen concentrations was attributed to the chemical delay time becoming very short at high oxygen concentrations and thus the physical processes (corresponding to physical delay time) dominated the total ignition delay. In addition, the rate of decrease of ignition delay with increasing ambient oxidizer concentrations became more pronounced as ambient temperatures were increased. Similar results

were observed by Kadota et. al [40], who found ignition delay to be inversely proportional to ambient oxygen mass fraction to the power of 1.12.

Contradictory results were obtained by Sangiovanni and Kesten [35], who varied ambient oxygen mass fraction between 0.02 and 0.14 for 200 µm and 300 µm butyl and furfuryl alcohol droplets. They found a negligible effect of increasing ambient oxygen concentration on ignition delay times as long as sufficient oxygen was available for ignition. A similar conclusion was made my Wood and Rosser [41]. Experiments with n-hexadecane droplets between 120-170 µm in air and 0.53 wt % O_2 showed a very weak variation in ignition delay between the two ambient oxidizer concentrations. However, for a given ambient oxygen concentration there existed a critical droplet size below which ignition would not occur.

2.3.6   Effect of Droplet Proximity

Studies on the effect of droplet number density or inter-droplet spacing have shed light on the effect of droplet proximity on ignition. As mentioned previously, studies of this nature have been conducted using linear droplet arrays, streams, or droplet clouds to investigate the interaction between droplets. In the case of droplet arrays or streams, inter-droplet spacing is typically reported in terms of the distance between the centers of the droplets normalized by the average monodisperse droplet diameter. In studies with droplet clouds, droplet number density is typically reported in number of droplets per unit volume. Numerous studies have been done on group combustion, both experimentally and theoretically, while fewer studies have focused on the ignition characteristics associated with droplet arrays, streams and clouds.

In general, the literature is in agreement that an increase in inter-droplet spacing results in a decrease in ignition delay. Droplet proximity affects the ambient gas environment as well as the diffusion characteristics surrounding individual droplets [11]. Wood and Rosser [41] made direct ignition delay measurements on single droplets, groups of three to five droplets, and a continuous stream of n-hexadecane droplets in air, with droplet diameters of 120-170 µm in ambient temperatures between 590℃ and 740℃. Their results showed a significant dependence of ignition delay on droplet number density. They observed that as the number of droplets increased, the ignition delay reduced. Increasing droplet proximity (or droplet number density) decreased the

ignition delay for a fixed ambient temperature. In addition, increased droplet density was found to decrease the critical temperature below which a droplet failed to ignite as shown in Figure 14.
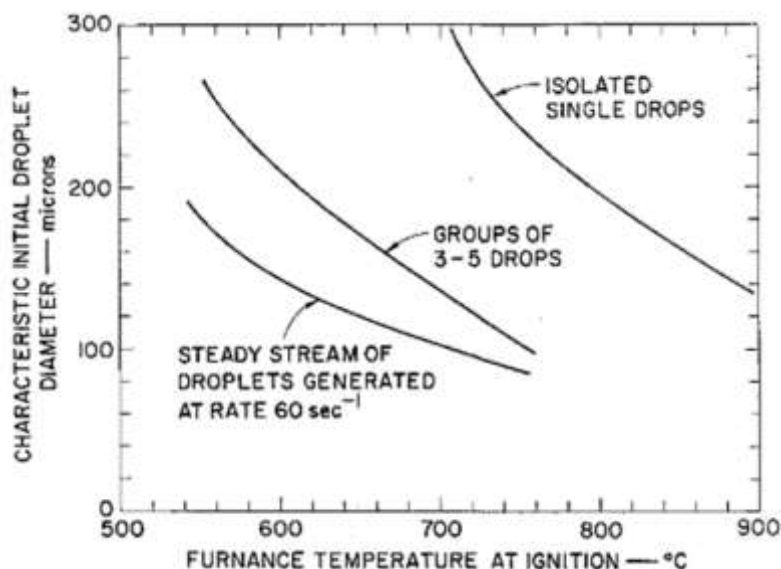
Figure 14. Ignition curves for n-hexadecane droplets (diameter in microns) in air at varying ambient temperatures (degrees C) [25]

Sangiovanni and Kesten [43] investigated the effect of droplet interaction on ignition in monodisperse streams. Continuous streams of 200-300 µm furfuryl alcohol and butyl alcohol droplets were injected into a hot gas environment. The inter-droplet spacing was varied from hundreds of droplet diameters to slightly less than two droplet diameters. Results showed an initial decrease in ignition delay as droplet spacing decreased between 16 and 6 droplet diameters. However, there existed an optimum droplet spacing (in this case between 4 and 6 droplet diameters) below which ignition delay begins to increase again as shown in Figure 15. They attributed the longer ignition delay times for smaller inter-droplet spacings to the lack of gas circulation occurring between the droplets. As droplet spacing increases, ignition delay initially decreases as a result of enhanced convective heating due to the relative velocity between the droplets and the gas. At a certain optimum droplet spacing, the ignition delay begins to increase with increasing droplet spacing.

SYMBOL	BURNER CONDITION	GAS TEMPERATURE T_∞ – DEG K	GAS VELOCITY V_∞ – CM/SEC
○	1	1452	136
□	2	1363	134
△	5	1242	133
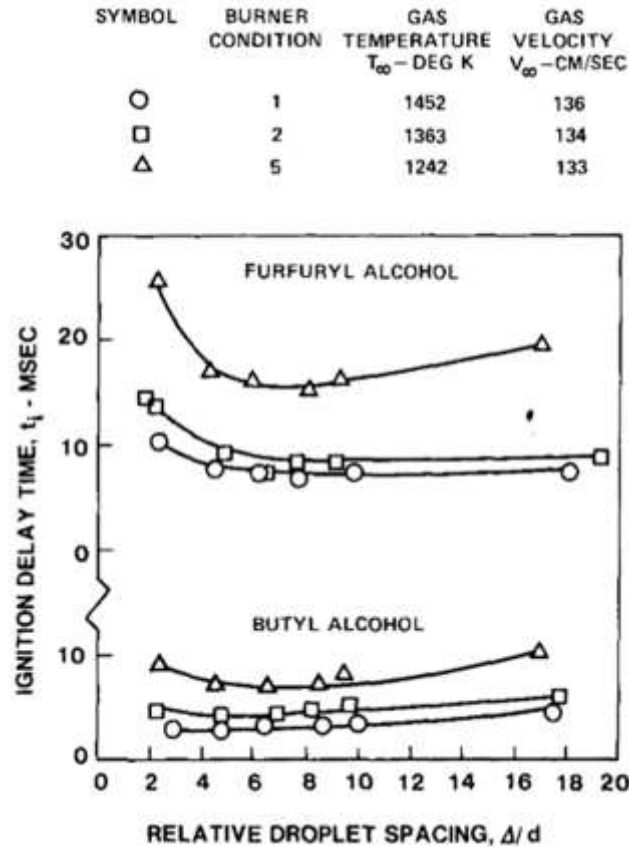
Figure 15. Variation of ignition delay (ms) with inter-droplet spacing for 200 µm droplets [43]

Sangiovanni and Kesten [43] also found that ignition delay times for small droplet spacings are significantly longer than those of isolated droplets. In addition, the effect of droplet interaction on the ignition process was more significant for small droplets, low ambient temperatures and fuels with low volatility. Though the authors additionally conclude that forced convection effects in heating and vaporizing droplets is minimal for high temperatures and small droplet spacings, the negligibility of forced convection effects cannot be readily extended to droplet diameters outside this small range (200-300 µm).

Ogasawara et. al [33] also noted that that in a droplet stream, a preceding droplet has a significant effect on the ignition delay of a droplet falling in a hot gas column, and that this effect varies with inter-droplet spacing. Ignition of the second droplet was promoted by either or both the thermal contribution from the flame of the first droplet, or the increased fuel vapor available in the

environment of the second droplet as a result of the evaporation of the first droplet. In some cases, the second droplet ignited before the first droplet.

One of the most extensive studies on droplet clouds was done by Laster and Annamalai [44] using 100 µm droplets of dodecane (boiling point 216 ℃) and octane (boiling point 125 ℃). Ignition delay for dodecane decreased with increasing droplet number density until a minimum ignition time at a number density of 1×10^{10} drops/m^3, after which ignition delay began to increase. However, a minimum ignition delay was not observed for octane, but instead the ignition delay continued to decrease as droplet number density increased until a more or less constant value was reached. Laster and Annamalai argued that for very dilute clouds, evaporation happens over several layers within the cloud. However, for more dense clouds (small inter-droplet spacing), evaporation happens in a single layer at the surface of the cloud, requiring more heat to be transported to the cloud from the ambient environment for sufficient evaporation to take place before ignition can occur. This in turn reduces temperatures surrounding the cloud, and leads to longer ignition delays as the fuel vapor travels further before it can achieve temperatures sufficient for ignition to take place.

A notable study on ignition delay of droplet arrays was done by Nishiwaki et al. [31] and the results are shown in Figure 16. Two 1 mm cetane droplets were placed side by side at varying distances with a range of ambient temperatures. Results showed that there existed an optimum spacing distance (in this case 4-5 mm corresponding to 4-5 droplet diameters) at which the droplets achieved minimum ignition delay. Moreover, as ambient temperature increased the optimum spacing distance increased. This observation was attributed to the increase in the vapor layer thickness surrounding the droplets at higher ambient temperatures.
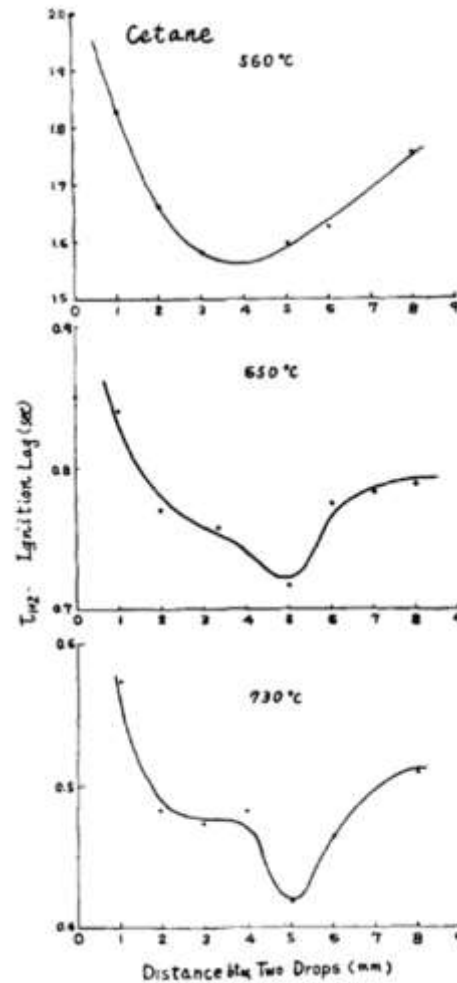
Figure 16. Ignition delay (sec) variation with distance (mm) between two 1 mm cetane droplets in a linear array [31]

The table below summarizes the discussed findings on the effect of ambient conditions and fuel type on the ignition delay of droplets. Because these conditions are coupled with droplet size effects, their effect may be discussed as it relates to the variation of ignition delay with droplet size.

Table 2. Summary of findings on the effects of ambient conditions on droplet ignition

Initial Droplet Size
Depending on the ambient conditions, the behavior of ignition delay with droplet size can be divided into four types: • *Monotonic increase in ignition delay with increasing droplet size.* This can be attributed to the longer heating times required as droplet size increases, which occupies a significant part of the total ignition time. In this type of behavior, the droplet heat-up, vaporization, and transport times all scale with droplet diameter squared. • *Monotonic decrease in ignition delay with increasing droplet size.* This behavior is attributed to a decrease in the system Da number () through a reduction in droplet size as well as a significant decrease in t_{diff}. In other words, the droplet heat-up time and vaporization time become negligibly small compared to the chemical reaction time. • *Initial decrease then increase in ignition delay with increasing droplet size (non-monotonic variation).* This behavior is typical of fuels with moderate to high volatility, low ambient temperatures and relatively small droplet sizes. • *No variation of ignition delay with change in droplet size.* This behavior is typical at very high ambient temperatures and pressures (see discussion on effect of high ambient pressures and temperatures).
Ambient Temperature

• For the same droplet sizes, ambient conditions and fuel, increasing ambient temperature decreases ignition delay. At the lower end of the temperature range, this decrease is drastic, and becomes less significant at higher temperatures. The rate of reaction and thus the reaction time is heavily dependent on the temperature. The reaction rate is increased (reduced reaction time) at higher temperatures, ultimately increasing the Da number and consequently decreasing the ignition delay.
• For fuels that show a monotonic increase (positive slope) or decrease (negative slope) in ignition delay with increasing droplet diameter at relatively low temperatures, increasing the ambient temperature:
  1. Decreases ignition delay values
  2. Decreases the effect of droplet size variation on ignition delay
• For fuels that have an initial decrease (negative slope) then increase (positive slope) of ignition delay time with increasing droplet diameter at atmospheric pressure (e.g n-hexadecane at low temperatures), increasing the ambient temperature:
  1. Gradually eliminates the region of negative slope (shift from ignition in the kinetically-controlled regime to the diffusion-controlled regime).
  2. Decreases ignition delay values in general
  3. Decreases the critical diameter below which ignition does not occur

Table 2 continued

Ambient Pressure
• For fuels that show a monotonic increase (positive slope) or decrease (negative slope) in ignition delay with increasing droplet diameter **at atmospheric pressure**, increasing the ambient pressure: 1. Decreases ignition delay values 2. Decreases the effect of droplet size variation on ignition delay • For fuels that have an initial decrease (negative slope) then increase (positive slope) of ignition delay time with increasing droplet diameter **at atmospheric pressure** (e.g n-hexadecane at low temperatures), increasing the ambient pressure: 1. Gradually eliminates the region of negative slope (shift from ignition in the kinetically-controlled regime to the diffusion-controlled regime). Da number is described as the ratio between the diffusion time scale and the reaction time scale Da ~ . The mass transfer time (or vaporization time) is proportional to d^2/D (where D is the diffusivity), therefore t_{diff} varies as $t_{diff} \sim P$ (pressure). However, t_{rxn} is proportional to (density/chemical reaction rate), and is therefore proportional to P^{-1}. This implies that the Da $\sim P^2$. Therefore at higher pressures, the contribution of the reaction time to the ignition time is less dominant than the diffusion time [14], [34]. 2. Decreases ignition delay values in general 3. Decreases critical diameter below which ignition does not occur. This is attributed to the increase in system Da number with pressure, thus enhancing droplet ignitability at high pressures.

Ambient Oxidizer Concentration
• Some experimental studies report a decrease in ignition delay with increasing oxidizer concentration, while other studies report little or weak variation. • Of the studies that reported a decrease in ignition delay, this behavior was attributed to the increase in chemical reactivity between the reactants. In addition, this effect levels off at high oxygen concentrations (> 50% by volume)

Fuel Type
The main influence here is of the difference in boiling points of different fuels. • For high volatility fuels, the mass transfer rates are generally significantly larger than in low volatility fuels and become larger as droplet size decreases. This results in a short mass transfer time compared to the reaction time. This begins to decrease the system Da number and, and consequently increases the ignition delay time. This is referred to as ignition in the kinetically-controlled regime. For low volatility fuels, the heat up and vaporization times are much longer in general compared to the reaction times. Because the vaporization times also scale with diameter, the ignition delay tends to increase as droplet diameter increases. This is referred to as ignition in the kinetically-controlled regime.

2.4 Flame Structure

In the literature, two kinds of droplet flames have been observed depending on the relative velocity between the droplet and the ambient gas. In general, envelope flames develop in low relative velocity conditions such as low ambient gas velocity for suspended droplets or low injection velocity for free-falling droplets. In contrast, wake flames develop in high relative velocity conditions [45]. In addition, for suspended droplets in low gas velocity streams, droplet shapes tend to be more spherical due to the absence of buoyancy or forced convection. The instant of ignition in this case is identified when a spherically symmetric flame appears in the boundary layer surrounding the droplet. In studies employing the free-falling droplet technique, gas-phase ignition has been shown to occur in the wake of a falling droplet if the conditions are suitable and injection velocities are sufficiently high.

A good example of both wake and envelope flames was observed by Charvonia [46]. In this study, ~3 mm diameter diethylamine droplets were injected into the heated decomposition products of white fuming nitric acid (WFNA), and ignition was identified by the appearance of a bright flame in the gaseous region above the droplet. The flame front would then propagate with a speed greater than the speed of the falling droplet until the flame engulfed and surrounded the droplet. Combustion of the droplet was then observed to continue in the vapors surrounding the droplet. Based on the observations made in this study, two types of ignition mechanisms were defined: vapor ignition (in the wake region of the falling droplet) and droplet ignition (the engulfment of the falling droplet).

Similar observations were made by other investigators. For n-hexadecane droplet sizes on the order of 1 mm, El Wakil and Abdou [47] also observed two different flame types depending on the air stream velocities. For low air stream velocity, a diffusion type flame was observed to initiate at the bottom of the droplet and eventually envelop the droplet. At higher velocities, a detached flame was observed at a distance above the droplet, where the flame stand-off distance was a function of the air stream velocity. For 120-170 µm n-hexadecane droplets falling in air, Wood and Rosser [25] also observed a luminous region indicative of a flame behind the droplet, however no observations were made of the flame overtaking and enveloping the droplets. In these cases, it was concluded that these droplets may not have been burning but rather vaporizing, with the flame

consuming the fuel vapor in the wake region of the droplet. For n-heptane, iso-octane, kerosene and n-octane, Suppramaniam [48] observed a moving droplet leaving a trail of vapor in its wake which mixed with the hot air, after which pre-ignition reactions were observed that led to spontaneous ignition in the wake. In some experiments however, ignition was observed to occur either on impact with the bottom of the chamber vessel or at the leading edge of the droplet at elevated temperatures.

Droplet streams that are injected vertically upwards expectedly yield different flame structures. Sangiovanni and Kesten [43] studied the flame structure development of monodisperse fuel droplet streams injected upward. For all conditions studied, the droplets were observed to first ignite individually with nearly spherical flames surrounding each droplet. Due to the strong effect of upward convection, flame wakes were observed in front of each droplet. For droplet spacing on the order of 20-25 droplet diameters, individual flames were observed to merge and group burning ensued. This behavior was partly attributed to the deceleration of droplets in the upward-moving stream.

A common parameter used to quantitatively describe the flame structure of burning droplets is the flame stand-off ratio. This ratio represents the position of the flame from the droplet center (diameter or radius), non-dimensionalized by the droplet diameter or radius. The classical quasi-steady theory predicts that the flame stand-off ratio remains constant throughout the droplet lifetime. In addition, the theory also overpredicts this value. This outcome is a result of the assumption of constant thermal and transport properties, the use of a unity Lewis number and the neglect of the unsteadiness of the gas-phase surrounding the droplet [48, 49].

In some experimental conditions, the flame stand-off ratio can approach a constant value [49], however other experimental results show an increase in the flame stand-off ratio with time. This increase has been attributed to fuel vapor accumulation effects as the droplet evaporates [26, 50]. An example of this can be seen in Figure 19 (b) for IPN droplets ranging between 0.79 mm and 1.97 mm. The flame stand-off ratios were shown to increase with time for all droplet sizes. In addition, small droplet sizes had higher flame stand-off ratios, as well as showed a larger dependence on time.

2.5   Hybrid Burning Characteristics of Monopropellant Droplets

Droplet combustion can be separated into three categories: bipropellant, monopropellant and hybrid combustion. The majority of hydrocarbon and hypergolic fuels exhibit bipropellant combustion. Whether pure fuels or blends, these fuels do not have any self-oxidizing properties and thus require a separate oxidizer to ignite and burn. Bipropellant combustion is characterized by a diffusion flame surrounding the droplet. In contrast, monopropellant fuels contain both the fuel and oxidizer in the same molecule and exhibit exothermic decomposition and burning in the absence of any external oxidizer. Hybrid combustion is defined as the burning of a monopropellant fuel in an oxidizing atmosphere [1]. In this mode of combustion, the fuel droplet first begins to evaporate and monopropellant vapor diffuses from the surface and decomposes exothermically. The decomposition products then continue to diffuse outward and eventually undergo oxidation with the inward diffusing oxidizer. In the literature, the observation of a dual flame structure has been identified as evidence of hybrid burning. This section provides an overview of studies on hybrid burning of monopropellant droplets.

Several investigations have been conducted on droplet combustion of the monopropellants hydrazine, monomethyl hydrazine (MMH) and unsymmetrical dimethylhydrazine (UDMH) in different oxidizing environments using a variety of experimental techniques. The porous-sphere technique was used by Rosser [52] to study the burning of hydrazine droplets with diameters between 3 mm and 13 mm in varying concentrations of oxygen. Fuel was fed to a porous sphere using a syringe and mass burning rates were calculated from the mass flow rate of the supplied fuel. At oxygen concentrations of slightly greater than 10%, observations were made of a dual flame structure indicative of decomposition of the fuel in an inner (decomposition) flame surrounded by oxidation of the decomposition products in an outer (oxidation) flame. For ambient oxygen concentrations greater than 20%, the oxidation flame seemed to obstruct the decomposition flame. Dykema and Green [53] also did not detect decomposition flames in their study of single suspended droplets of hydrazine in air. The authors concluded that the relatively high ambient oxygen concentration in the air could have obstructed the inner flame as in Rosser's observations. In a study on hydrazine droplet combustion, Lawver [54] investigated the combustion of hydrazine droplets in N_2O_4 vapor at 150 using the suspended droplet technique. Fuel droplets were suspended using a 0.01 in. diameter thermocouple and liquid N_2O_4 was heated and directed into the test vessel.

Lawver found that the ignition of single droplets of hydrazine was initially flameless, but a rise in droplet temperature recorded by the thermocouple was followed by the appearance of a reddish-orange flame. This was followed, a few milliseconds later, by the appearance of a bright yellow flame between the orange flame and the droplet surface. Photographic images showed two distinct regions of combustion, characteristic of the dual-flame or hybrid combustion of hydrazine and hydrazine-based fuels.

In the early 1970s, Allison and Faeth [55] investigated the combustion characteristics of MMH, UDMH and hydrazine droplets at atmospheric pressure. They observed droplets burning in the combustion products of a flat flame burner to simulate combustion chamber conditions. Both the suspended droplet technique and the porous-sphere technique were used to experimentally obtain burning rate data using the variation of droplet diameter with time. Under decomposition conditions (zero ambient oxygen mass fraction) no visible flame front was observed for any of the fuels. However, for all oxidizing conditions (non-zero ambient oxygen mass fraction), two distinct zones of reaction were observed for all three fuels. Figure 17 shows a 1.27 cm diameter hydrazine droplet burning in ~40% oxygen concentration environment. Similar observations were made for MMH and UDMH droplets.
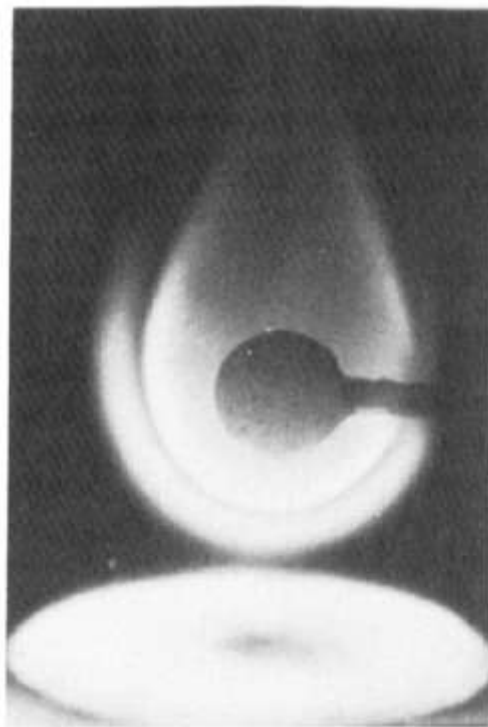
Figure 17. Hybrid burning of a hydrazine droplet (1.27 cm) in ~40% O2 concentration [55]

Another example of a monopropellant that exhibits strong hybrid burning behavior is isopropyl nitrate (IPN). Anirudha et. al [2] studied the combustion characteristics of IPN and its blends using suspended droplets ranging in size between 0.79 and 1.97 mm ignited using a nichrome wire in quiescent air. The investigators observed three different zones forming the flame structure of a burning IPN droplet in air as shown in Figure 18. Zone I referred to the inner dark region surrounding the droplet where IPN vapor was said to diffuse outwards toward a bluish violet region denoted by Zone II. This zone denoted the premixed monopropellant flame where the IPN vapor undergoes decomposition. Lastly, the IPN decomposition products reacted with oxygen in Zone III, producing a luminous diffusion flame.
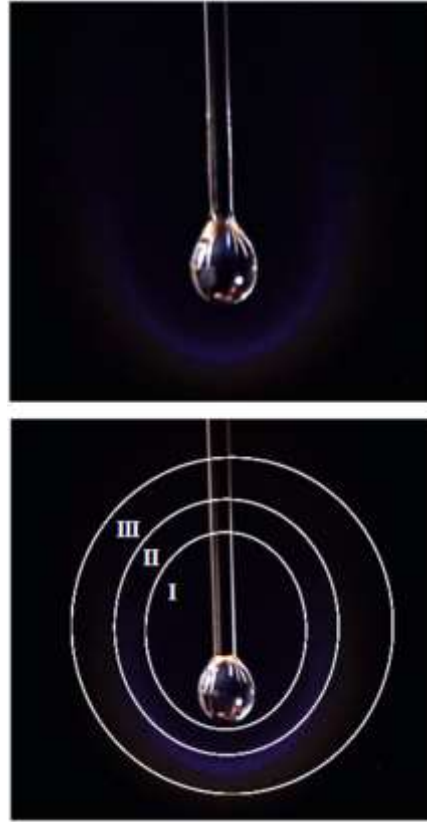
Figure 18. Flame structure of a droplet of pure IPN in air [2]

For IPN droplets with diameters between 0.79 and 1.79 mm, Anirudha et. al [2] found that the burning characteristics were greatly dependent on initial droplet size as shown in Figure 19. Contrary to the classical D^2-law theory, the results showed that for a particular droplet size, the flame stand-off ratio increased in time. Also, the stand-off ratio increased for larger initial droplet diameters. This behavior was attributed to the effects of fuel accumulation in Zone I (vaporization zone), where the fuel vaporization does not balance the rate of fuel consumption. In addition, the burning rate constant was shown to increase with increasing droplet size, with an approximately 280% rise over the modest range of droplet size considered in this study. This observation was primarily attributed to natural convection effects, which increase droplet burning rates and are greater for larger droplet sizes.
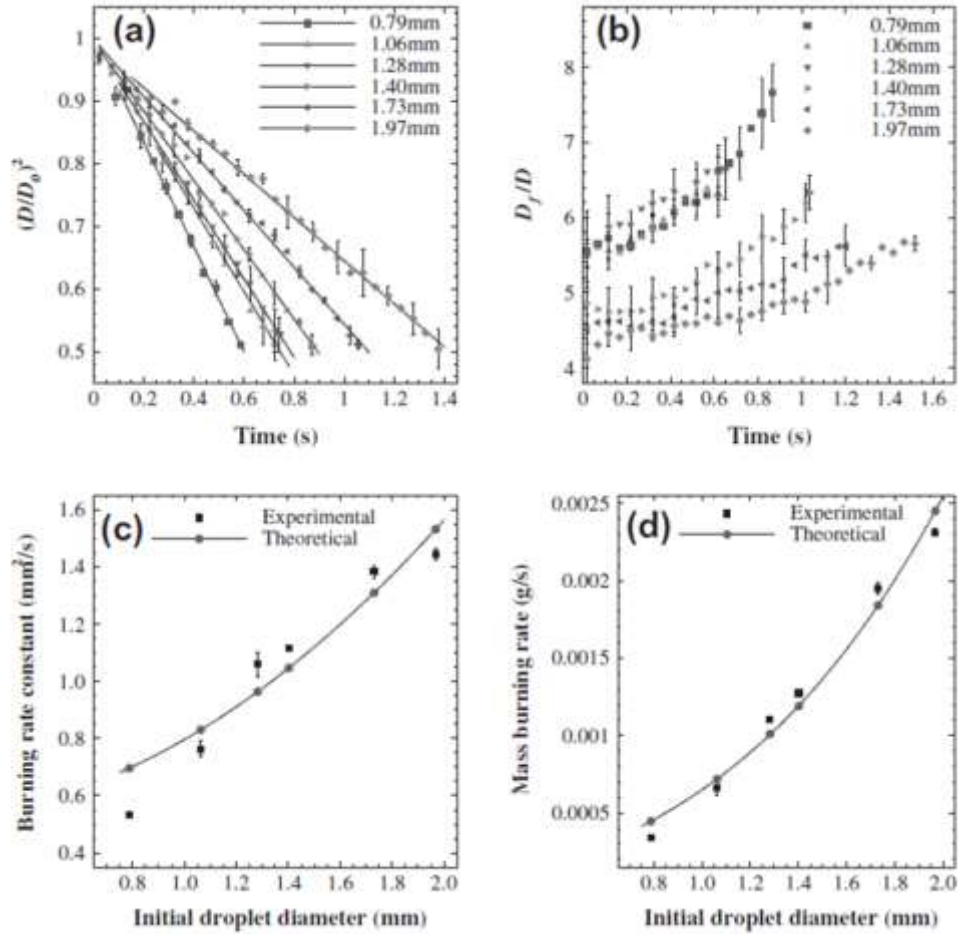
Figure 19. Variation of (a) normalized square of droplet diameter with time; (b) flame stand-off ratio with time; (c) burning rate constant with initial droplet diameter; (d) mass burning rate with initial droplet diameter for pure IPN droplets [2]

2.6   Thermal Droplet Ignition Theory

Droplet ignition theories and analyses in the literature seek to determine ignition limits based on ambient conditions and initial droplet properties. They also have been used to predict ignition delay based on a prescribed ignition criterion, and to describe the effects that ambient conditions and droplet properties have on this parameter. Most ignition theories are based on the competing rates of heat loss and heat generation from reactions and are therefore referred to as thermal ignition theories. Ignition criteria for these theories have been represented, in varying formulations, as a transition from a kinetically-controlled regime to a diffusion-controlled burning regime [56], and will therefore be the main focus of review in this section. Other investigators have also defined ignition criteria based on the concentration of a crucial chain branching intermediate species, such

that when this particular species concentration reaches a critical level in the gas phase, ignition is predicted to occur [5,34].

Droplet ignition analyses can further be divided into quasi-steady analyses and transient analyses. The latter involves numerically solving the partial differential equations that govern the fluid mechanics and heat transfer processes in both the liquid phase and the gas phase surrounding the droplet [14]. Quasi-steady analyses are based on the assumption that processes in the gas phase progress much faster than those in the liquid phase (e.g. droplet surface regression, evolution of species concentration and temperature), and therefore gas phase processes can be assumed to be quasi-steady and time derivatives can be neglected in the gas phase and considered only for liquid phase processes. Predictions of ignition delay and ignitability limits, and the effects of ambient conditions on these parameters, using quasi-steady droplet ignition (QSDI) analyses have been shown to be in reasonable agreement with existing experiment data [5,13,14,31].

The main difference between thermal ignition theories from those of steady state combustion is the inclusion of finite kinetic rates. For simplicity, an Arrhenius one-step irreversible reaction is considered to represent the reaction kinetics. Other assumptions that are typically used in these theories are spherically symmetry of the system and equilibrium between condensed fuel and its vapor at the droplet surface.

In general, two approaches have been used in the theoretical analysis of droplet ignition. In one approach, the dependence on reaction rate on temperature has been approximated by assuming a specific ad hoc form of temperature distribution with the flame zone. Peskin and Wise [56] confined chemical reactions to a single spatial location and represented the distribution of chemical reaction by a Dirac delta function at a hypothetical flame surface. From this model, mass burning rate as a function of ambient temperature could be extracted, and ignition was identified when the system changed from one which required heat from the environment to proceed to one where heat is released to the environment, corresponding to a transition between kinetically-controlled and diffusion-controlled burning modes. The more common approach in the literature is the use of perturbation techniques and asymptotic methods to solve exact conservation equations with varying choices for the perturbation parameter. In general, the analysis domain is divided into three

zones as shown in Figure 20. Kassoy and Williams [57] designated the Da number as the perturbation parameter, analyzing solutions in the limit of zero and infinite Da numbers corresponding to frozen chemistry and infinite reaction rates, respectively. However, this analysis was unable to provide any insight on ignition and extinction phenomena.
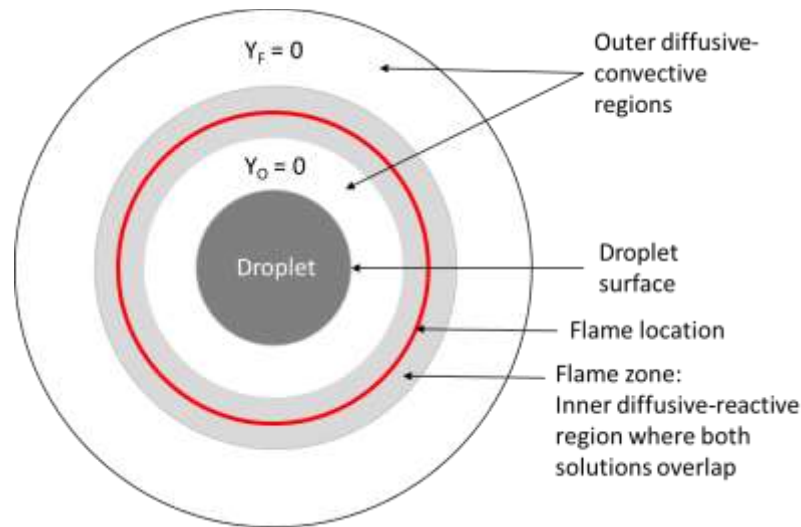
Figure 20. Diffusive-reactive and diffusive-convective zones defined for asymptotic analysis of droplet ignition

Liñán [58] performed asymptotic analysis on counter-flow diffusion flames in the limit of large activation energies, treating the activation energy (or activation temperature) as the large parameters. The analysis produced results for $0 < \mathrm{Da} < \infty$ and four burning regimes were identified in the form of the S-curve similar to the one shown in Figure 21. Law [14,56] extended Liñán's work to the problem of a fuel droplet introduced into a hot oxidizing gaseous atmosphere. In this model, the following additional assumptions were made:

1. Quasi-steady gas phase processes
2. Constant heats of combustion and vaporization
3. Constant heat capacities and thermal conductivities
4. Unity Lewis number
5. Constant pre-exponential Arrhenius factor
6. The reaction is first-order with respect to fuel and oxidizer concentrations

The small perturbation parameter used is ε, defined as $\varepsilon = T_\infty/T_a$, where T_∞ is the ambient temperature and T_a is the activation temperature ($T_a = E_a/R$), and ignition criterion is defined in terms of the Da number. The determination of Da is discussed in greater detail in Appendix A. The governing equations for species and temperature conservation are solved numerically, where at each time step, the system Da number is compared to the ignition Da. Ignition occurs once this threshold is achieved. Theoretical predictions of ignition limits using this model were shown to be in good agreement with hydrocarbon droplet ignition experimental data from Wood and Rosser [25]. With this analysis, Law obtained the characteristic S-shaped curve as shown in Figure 21. Similar to Liñán's analysis, the curve was used to identify four different burning regimes:

1. *Nearly frozen regime*: region between the frozen state (Da = 0) and ignition (Da = Da$_I$), representing weak reactions and in many cases, the kinetically controlled regime.
2. *Partial burning regime*– this region represents a weakly burning flam separating the oxidizer and fuel regions, and allows for leakage of the reactants through the flame [59]
3. *Premixed flame regime*
4. *Near-equilibrium diffusion regime:* region between extinction state (Da = Da$_E$) and infinite kinetic rates (Da = ∞)
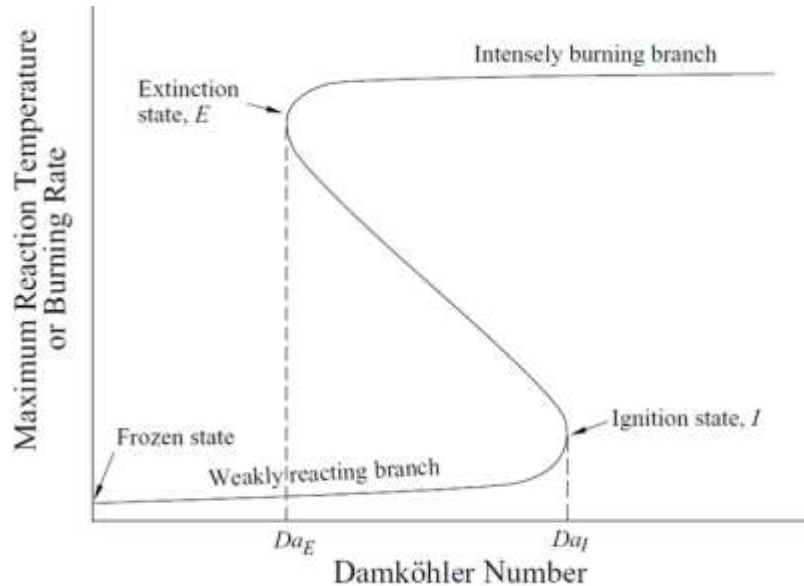
Figure 21. S-curve concept showing ignition and extinction states [60]

Due to its relative simplicity and applicability, Law's quasi-steady droplet ignition analysis, with modifications from Aggarwal [14], will be used to make theoretical comparisons with experimental data obtained in this work. A more detailed fundamental description of the theory and the manner in which it is applied is presented in Appendices A and C, while the specifics of the formulation can be found in references [14], [56] and [14].

2.7 Hybrid Combustion Model

Many investigators have proposed various models for droplet combustion or improvements to existing models through relaxation of one or more model assumptions. Most models may be grouped into three main categories: monopropellant combustion, bipropellant combustion, and hybrid combustion. Both monopropellant and bipropellant combustion have been investigated extensively and excellent reviews exist on the subjects.

Monopropellant combustion is the phenomena used to describe the burning of a monopropellant with a self-sustained flame without any separate oxidation source due to the existence of both the fuel and oxidizer in the same molecule. The most widely known formulation of the monopropellant combustion model was developed by Spalding and Jain [61]. Some assumptions used in this model include: spherically symmetric flow, uniform droplet temperature, constant transport properties, steady-state processes, and neglect of radiation, convection and buoyancy effects. Heat is conducted to the droplet from the atmosphere, causing the liquid fuel to vaporize. The vapor then diffuses outwards from the droplet surface and chemical decomposition takes place at the flame front, after which decomposition products flow outward. A general result of this model is given by the equation:

$$K = \frac{d(d_s^n)}{dt} \tag{4}$$

where is the burning constant, is the droplet diameter and is a parameter that ranges from 1 to 2 depending on the droplet size. Investigators have relaxed several assumptions in an attempt to improve the model, such as considering the influence of forced and natural convection on monopropellant burning. It has been shown that the burning rate is not influenced by convection

below a critical Reynolds number, at which point the burning rate is no longer controlled by chemical kinetics and can be assumed to be equal to the evaporation rate [62].

Bipropellant combustion describes the burning of a fuel droplet in an oxidizing environment. The hot ambient atmosphere heats up the droplet and begins to vaporize it. The fuel vapor then diffuses outward and reacts with the inwardly diffusing oxidizer in an infinitely thin reaction zone. The heat produced is then transported both inward toward the droplet and outward into the ambient environment. The classical droplet combustion model, widely known as the double-film model or the D^2 law, was initially developed by Godsave [63] and Spalding [64] in the 1950s. Though relatively simple, the model has been used to reasonably predict droplet burning rates and burn time in combustors. The main result of the D^2 law is that the square of the droplet diameter decreases linearly with time for both evaporation and combustion processes. Using the assumption that the flame is infinitely thin and that the fuel vapor produced at the surface is entirely consumed at the flame, conservation equations can be written for both the inner diffusive-convective region and the outer diffusive-convective region separately. Equating the droplet gasification rate with the fuel mass consumption rate at the flame, the following conclusive explicit expressions are obtained [10]:

$$K = -\frac{d(d_s^2)}{dt} \tag{5}$$

$$K = \frac{8k_g \ln(1+B)}{\rho_l C_{pg}} \tag{6}$$

$$d_s^2(t) = d_{so}^2 - Kt \tag{7}$$

where and are the thermal conductivity and specific heat of the ambient gas.
The Spalding number, is defined as:

$$B = \frac{C_{pg}(T_\infty - T_s) + (\Delta h_c/v)}{q_{i-l} + h_{fg}} \tag{8}$$

where heat transfer to the interior of the droplet, , q_{i-l}, is neglected, Δh_c is the heat of combustion, and $\nu,$ is the stoichiometric air-fuel ratio.

Several of the assumptions of this model have also been relaxed over the years in an attempt to improve the model and explain differences between experimental measurements and theoretical predictions of burning rates and other parameters such as flame stand-off ratio and droplet lifetime. Though the D^2 law has been useful for initial estimates of mass burning rates and flame temperature among other parameters, several assumptions break down with significant deviations from the assumption of an isolated, symmetric, single component droplet reacting in a stagnant oxidizing medium. Studies have been done on the effects of parameters such as initial droplet heating, fuel accumulation, convection and ambient pressure, among others, have on droplet combustion characteristics. Specifically, convection effects are an important aspect of droplet combustion as it relates to spray combustion processes. Several researchers have formulated corrections to the mass burning rates in conditions of forced or natural convection, and such corrections will be imposed in the results of this work as well. The presence of non-radial convection enhances the transport rates and consequently the evaporation rates and/or mass burning or evaporation rates [62].

Hybrid combustion describes the burning of a monopropellant droplet in an oxidizing environment in which aspects of both monopropellant and bipropellant combustion are present. Common hybrid combustion systems include the burning of hydrazine fuels with oxidizers such as nitrogen tetroxide, and nitromethane or isopropyl nitrate in oxidizing atmospheres. Both the monopropellant and bipropellant models failed to accurately predict experimental mass burning rates for monopropellants burning in an oxidizing environment, forming the premise of Allison's work in postulating the hybrid combustion model in his thesis on hybrid and decomposition combustion of the hydrazine fuels [1]. This model will be used in the analysis of the data obtained during this study, and such, a brief discussion of the model fundamentals is presented here. More detailed discussions can be found in references [48] and [52].

Figure 22 shows a schematic of the hybrid combustion model. It consists of a spherical monopropellant fuel droplet surrounded by a decomposition flame, where the vaporized fuel

decomposes and reacts. A second bipropellant or oxidation flame also exists where all the decomposition products and ambient oxidizer is assumed to react. The monopropellant flame is assumed to be an infinitely thin region where decomposition burning takes place. The decomposition products are then transported radially outwards and react with the oxidizer at the oxidation flame, and afterward the combustion products are transported outward into the ambient environment. Other model assumptions include steady-state conditions, a unity Lewis number, insolubility of all gaseous non-fuel species in the liquid phase, and thermal diffusion and radiation are neglected.
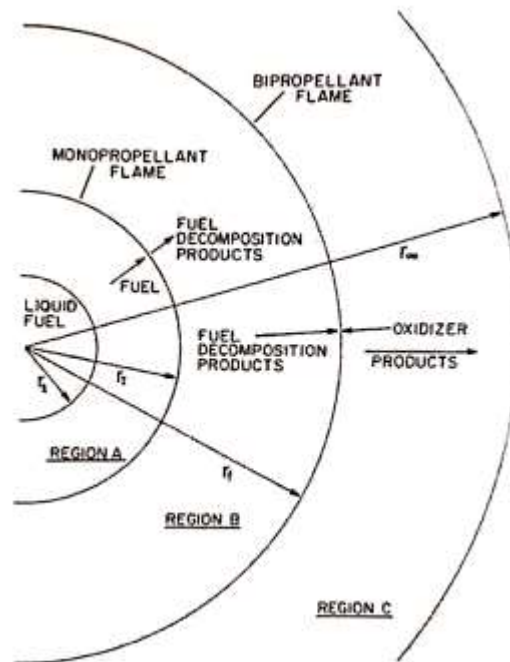
Figure 22. Schematic of the Hybrid Combustion Model [1]

Equations for the conservation of mass, energy and species were obtained for regions A, B, and C in Figure 22. Region A contains only diffusing fuel, region B contains only diffusing decomposition products, and in region C, only oxidizer and oxidation flame products are present. These equations are integrated using their respective governing boundary conditions to obtain a closed set of five equations and five unknowns [1]:

$$\frac{\dot{m}C_F}{\lambda_{Al}r_l}\left(1 - \frac{1}{\beta_I}\right) = \frac{1}{\theta_l}\left[\theta_I - \theta_l - (L^* - \theta_l)\ln\left(\frac{\theta_I - \theta_l + L^*}{L^*}\right)\right] \tag{9}$$

$$\frac{\dot{m}C_{FP}}{\lambda_{Bl}r_l}\left(\frac{1}{\beta_I} - \frac{1}{\beta_f}\right) = \frac{1}{\theta_l}\left[\theta_f - \theta_I - (Q_1 - \theta^0)\ln\left(\frac{\theta_f - \theta^0 + Q_1}{\theta_I - \theta^0 + Q_1}\right)\right] \tag{10}$$

$$\frac{\dot{m}\sigma}{\lambda_{Cl}r_l}\left(\frac{1}{\beta_f} - \frac{1}{\beta_\infty}\right) = \frac{1}{\theta_l}\left[1 - \theta_f - (Q_2 - \theta^0)\ln\left(\frac{1 - \theta^0 + Q_2}{\theta_f - \theta^0 + Q_2}\right)\right] \tag{11}$$

$$\theta_f = \frac{1 - \theta^0 + Q_2}{\left(\frac{\gamma + \gamma_{O\infty}}{\gamma}\right)^{\sigma/C_O}} + \theta^0 - Q_2 \tag{12}$$

$$\dot{m} = \beta_I{}^2 r_l{}^2 A e^{(-E/2R\theta_I T_\infty)} \tag{13}$$

where the unknown parameters are:

1. Non-dimensional decomposition flame radius: $\beta_I = {}^{r_I}/r_l$

2. Non-dimensional oxidation flame radius: $\beta_f = {}^{r_f}/r_l$

3. Non-dimensional decomposition flame temperature: $\theta_I = {}^{T_I}/T_\infty$

4. Non-dimensional oxidation flame temperature: $\theta_f = {}^{T_f}/T_\infty$

5. Mass burning rate for the hybrid case: $\dot{m}$

E

q

u

a

t

i

o

n

s

R

E

F

hydrazine mass burning rate data for a typical oxidation condition (ambient oxygen mass fraction of 0.132). The predictions of mass burning rate using the hybrid combustion model with different activation energies are also plotted and are in good agreement with the experimental data.
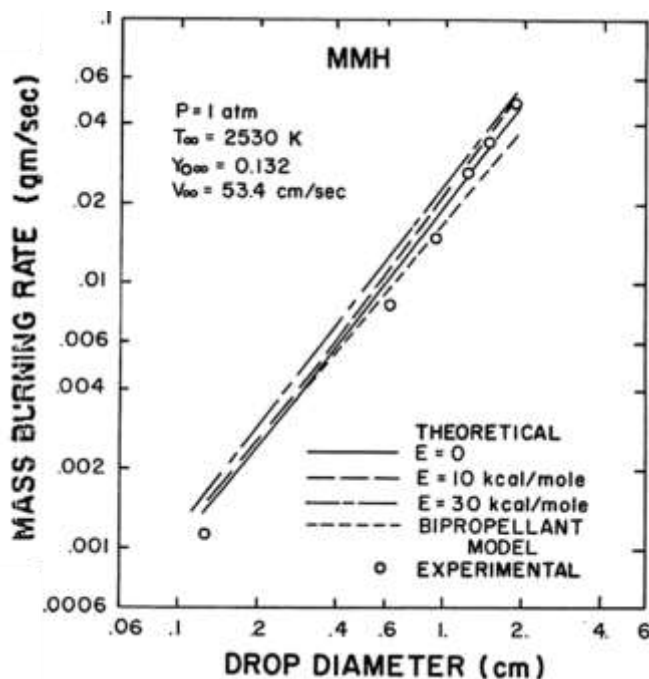
Figure 23. Variation of Experimental MMH burning rates with initial droplet diameter in ambient oxygen mass fraction of 0.132, compared with theoretical predictions [1]

2.8 Hydroxyl Radical (OH*) Chemiluminescence

Chemiluminescence can be described as the process through which electronically excited radicals in a flame undergo 'spontaneous radiative deexcitation'[65]. The generation of radicals occurs during the beginning stages of combustion (ignition) where energy absorbed by these radicals through collisions with other molecules and atoms causes them to become excited. A deactivation or relaxation period ensues shortly after as the radicals transition from their excited state to a ground or lower energy state, during which emission of light occurs and is referred to as chemiluminescence [66]. The hydroxyl radical (OH*) and the methylidyne radical (CH*) have been studied extensively as they are important species in hydrocarbon oxidation due to their

formation in the flame. The OH* radical in particular has been used as an indicator of the location of the flame front and areas of heat release.

In hydrocarbon oxidation, OH* chemiluminescence occurs when the electronically excited hydroxyl radical transitions from its excited state to its ground state, and is therefore a result of the radiative decay of the OH* radical [66]. OH* chemiluminescence detection has gained importance over the years as a diagnostic tool due to its simplicity, non-intrusiveness and potential to provide important flame information without expensive or complex optical equipment.

OH* chemiluminescence detection has been used to characterize ignition delay for various fuels as well as to indicate the location and thickness of flames [65]. In this technique, a camera, commonly used with an in-built intensifier (e.g an ICCD camera) or with a separate intensifier, detects the light emission from chemically excited OH* that are present in the flame. A relevant example of such an experiment would be that designed by Marchese et al. [65]. In their study, an experiment was designed to measure the ignition delay of fatty acid methyl ester fuel droplets in a microgravity experiment facility. A liquid fuel droplet was injected into a hot gas environment and the period between injection and initial observation of a flame from OH* emission was measured. The UV emission from the OH* radical was acquired using an intensified CCD camera and UV transmission lens, while a second camera was used to track diameter variation of the droplet during combustion. Droplets with diameters ranging between 1 and 1.2 mm were produced from 10 microliter syringe and deposited onto small epoxy beads on a 14 µm silicon carbide fibers featuring small epoxy beads onto which the droplets were deposited. Figure 24 shows a 0.95 mm methyl dodecanoate droplet igniting in 1079 K ambient temperature [67].
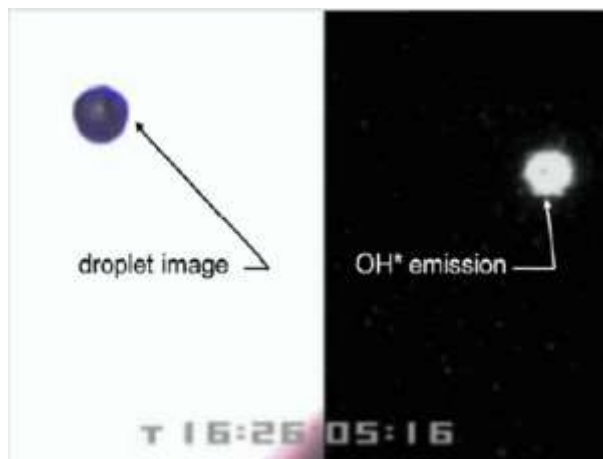
Figure 24. OH* emission of a 0.95 mm methyl dodecanoate droplet igniting in ~1079 K ambient temperature [65]

In the current study, OH* chemiluminescence was selected as the means by which droplet ignition delay data would be obtained. The ignition delay is therefore defined as the time that elapses between droplet exposure to high temperature gases and the onset of UV emission from the OH* radical. OH* has its peak at ~306-310 nm, and therefore a UV lens, and a narrow bandpass filter centered at ~309 - 310 nm are required for this technique.

2.9   Propellant Summary

This work focuses on the ignition and combustion behavior of three fuels. Methanol is chosen as a baseline fuel for comparison with two common monopropellants, NM and IPN. A summary of the physical properties of these propellants are outlined in Table 3.

Table 3. Propellant Properties

	Nitromethane	**Isopropyl nitrate**	**Methanol**
Formula	CH_3NO_2	$C_3H_7NO_3$	CH_3OH
Boiling Point [°C]	101.1	101.5	64.7
Molar Mass [g/mol]	61.04	105.09	32.04
Density (Liquid) [g/cm^3] at 20	1.137	1.04	0.792
Vapor pressure [kPa] at 20	3.7	4.2	13.02
Heat of Combustion [kJ/kg] 20°C	-10540	-18566 [68]	-22652

Nitromethane (CH_3NO_2) is an organic compound and at room temperature is a colorless, oily liquid with a high adiabatic flame temperature of 2400 [69]. It has been used in various propulsion applications as both a monopropellant and as a bipropellant in internal combustion engines and rocket engines. In many of these applications, it has been used in conjunction with methanol in order to reduce flame temperatures and increase its stability for drag racing. The nitromethane fuel used in this study was 99+% pure and was obtained from ACROS Organics [TM].

NM structure   IPN structure
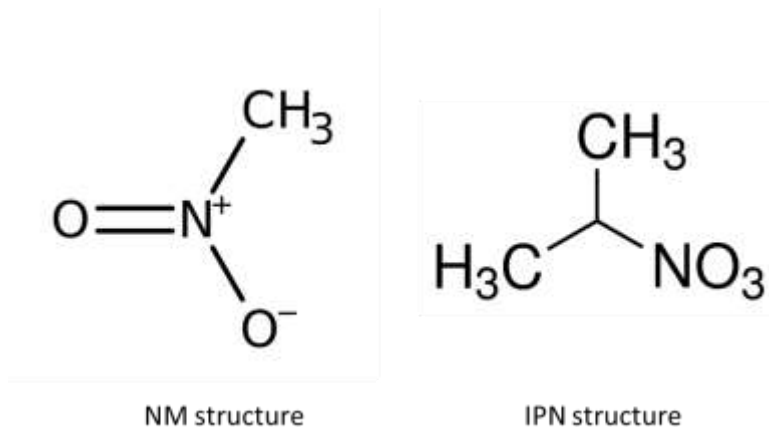
Figure 25. NM and IPN molecular structure [70]

Isopropyl nitrate ($C_3H_7NO_3$) is a colorless liquid, described as having a pleasant odor. In addition to being relatively affordable, other advantages include its non-toxicity and non-corrosiveness. It has been frequently used in blends with other fuels such as gasoline to improve performance. The isopropyl nitrate fuel used in this study was 99% pure and was obtained from Sigma Aldrich.

3. EXPERIMENTAL METHOD

3.1 Overview of Experimental Setup

A schematic of the major components of the experimental setup is shown in Figure 26 and photographs of the actual hardware are shown in Figure 27 and Figure 28. The experiment was conducted in the Applied Laser Spectroscopy Lab (ALSL) at Purdue University. A McKenna burner was used to provide the hot gases in which fuel droplets would ignite and burn. A more detailed description of the McKenna burner and its operation is described in the next section.

Silica fibers were used to suspend NM, IPN and methanol droplets with a range of initial diameters. The 125 µm silica fibers were used to suspend droplets with droplet diameters larger than ~800 µm. Droplets below this size were suspended on 80 µm fibers. Silica fibers were chosen due to their low thermal conductivity (1.4 W/mK) as well as their ability to maintain shape and strength in high temperature environments such as in the combustion gases of a flat flame burner. A 4.5" by 10" ultra-high-temperature moldable ceramic flame shield was used to initially shield the suspended droplets from the flat flame before the beginning of each test. The flame shield was positioned 1" above the burner surface. This height was chosen to make the lighting of the burner underneath the flame shield easier, as well as to reduce the thermal loading on the flame shield for the duration that it sat above the flat flame. The flame shield was attached to a pneumatic cylinder, which was powered by a solenoid valve and operated at 60 psi to quickly withdraw the flame shield when a 12 V trigger signal was applied to the solenoid valve during a test. The droplet would then be exposed to the hot combustion gases, after which the flame shield would return into position above the burner 10 seconds after the trigger after the flame was extinguished and the test was completed. The silica fibers were attached to a Teflon rod fitted on an optical post to easily alter the height of the droplets above the flat flame if needed. A delay generator was used to trigger the flame shield to withdraw from its initial position above the burner, as well as two orthogonally positioned high-speed cameras to begin recording simultaneously. During tests, relevant personal protective equipment (PPE) consisted of fire resistant lab coats, safety glasses and nitrile gloves, as well as fire resistant gloves when coming into contact with the burner during shutdown procedures.
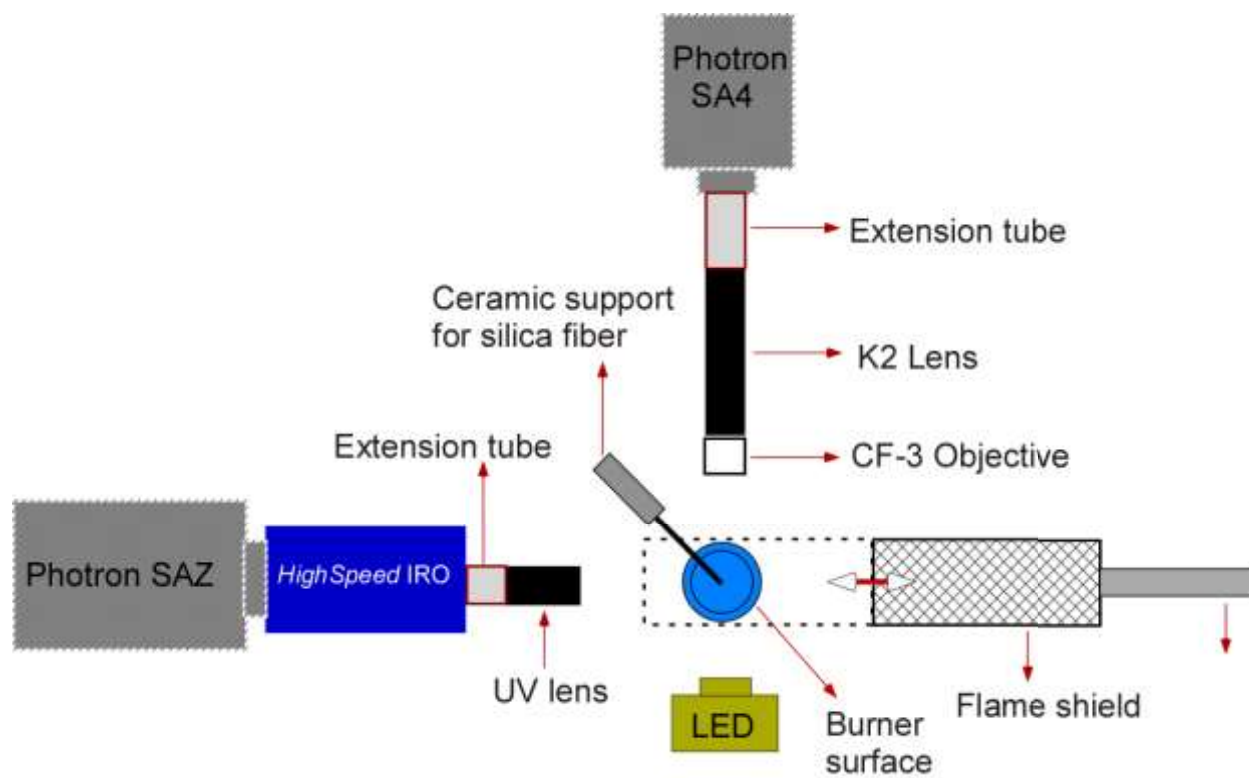
Figure 26. Schematic diagram of the major components of the experimental setup (Top view)
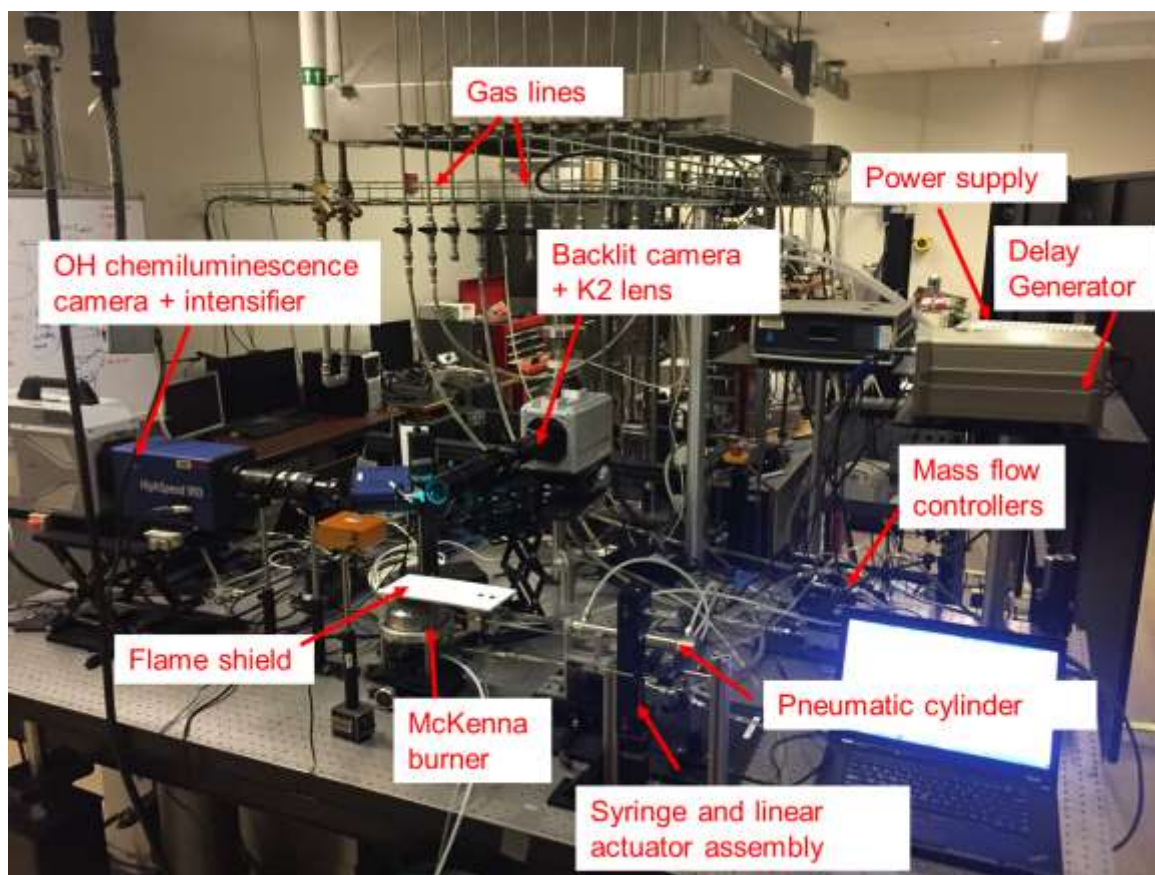
Figure 27. Droplet ignition and combustion experimental setup
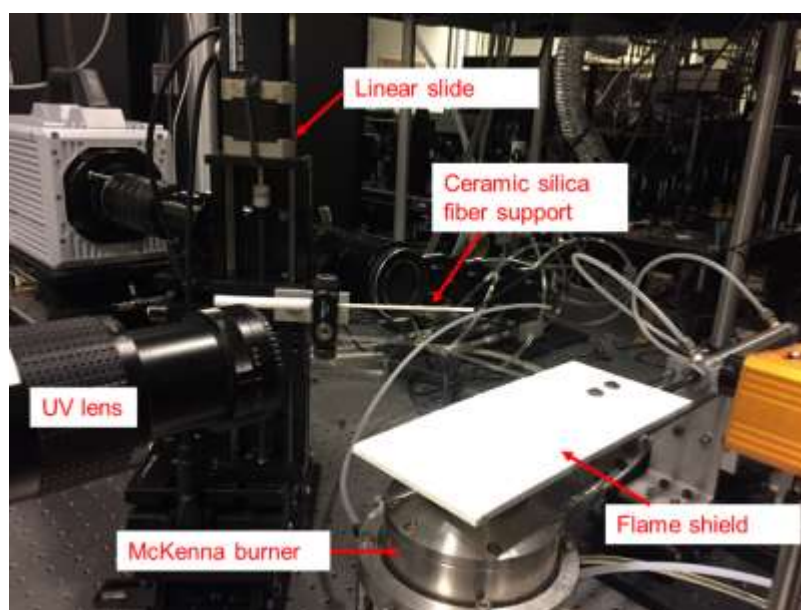
Figure 28. Droplet ignition and combustion experimental setup showing positioning of the McKenna burner, flame-shield and fiber support

The overall procedure consisted of starting with the flame shield in position above the surface of the burner. The lights were then turned off for operation of the intensifier used on one of the high-speed cameras. The gases were run at the desired flowrates, and a droplet was produced from the movement of a 10 µl syringe plunger using a linear actuator and was deposited on the tip of the silica fiber, and thereafter the burner flame was lit. The delay generator then received an external trigger to withdraw the flame shield and allow the fuel droplet to be exposed to the combustion gases, and also simultaneously triggered the two high speed cameras to begin recording the ignition and combustion event. The flame shield stayed withdrawn for a maximum of 10 s before it was pushed back into position above the flat flame burner by the pneumatic cylinder.

3.2   McKenna Burner

A McKenna burner was used to provide the high temperature environment for the ignition and combustion of the fuel droplets. An internal schematic of the premixed burner is shown in Figure 29. The McKenna burner was chosen due to its high repeatability and flame stability. The surface of the burner onto which the flame stabilizes is 6 cm in diameter. The burner also features a bronze sintered disk 15 mm in thickness, having an average pore size of 100 µm - 150 µm and a porosity of 30% - 40% [71]. These values were used when calculating the required convective velocities of the premixed gases. The minimum required convective velocity of the gases is the calculated laminar flame speed to maintain a stable flame and prevent flash back. The McKenna burner also features an external annular surface for the flow of a shroud gas. The shroud gas, in this case nitrogen, is used to improve stability of the flame, as well as prevent entrainment of air from the ambient environment which could alter oxygen concentration surrounding the droplet. The burner was actively cooled using a flow of water at a flowrate of approximately 1.8 gallons/hour. More detailed information on the construction of the burner can be found in [72].
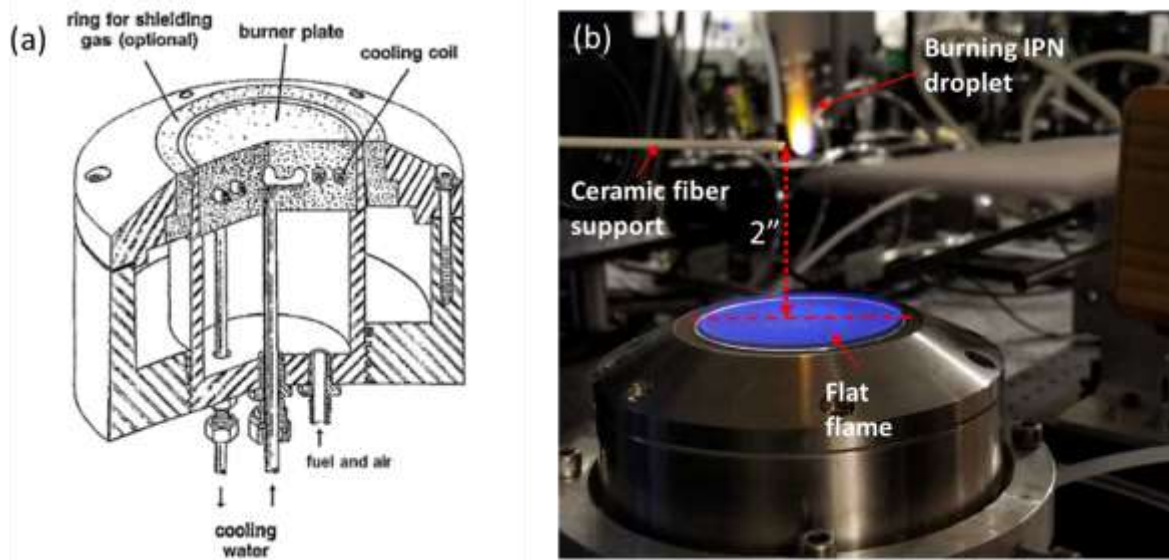
Figure 29. Internal Schematic of a standard McKenna burner [73]; (b) IPN droplet burning with burner operation at $\varphi = 0.51$

A series of mass flow meters were used to provide the premixed gases to the burner as shown in Figure 30. All the flow meters were calibrated with their respective gases before operation of the burner. For the current study, the equivalence ratio (φ) of the burner flame was maintained at $\varphi = 0.51$ because out of the most stable flat flames, this condition represented the highest oxygen concentration that could be achieved. The premixed gases consisted of 70.8 % nitrogen and 29.2% oxygen as the oxidizer, run at flow rates of 18.1 lpm and 7.5 lpm respectively. Methane was chosen as the fuel and run at a flow rate of 1.9 lpm. Nitrogen was chosen as the shroud gas and run at a flow rate of 5.6 lpm and 37.7 lpm depending on the droplet height above the burner.
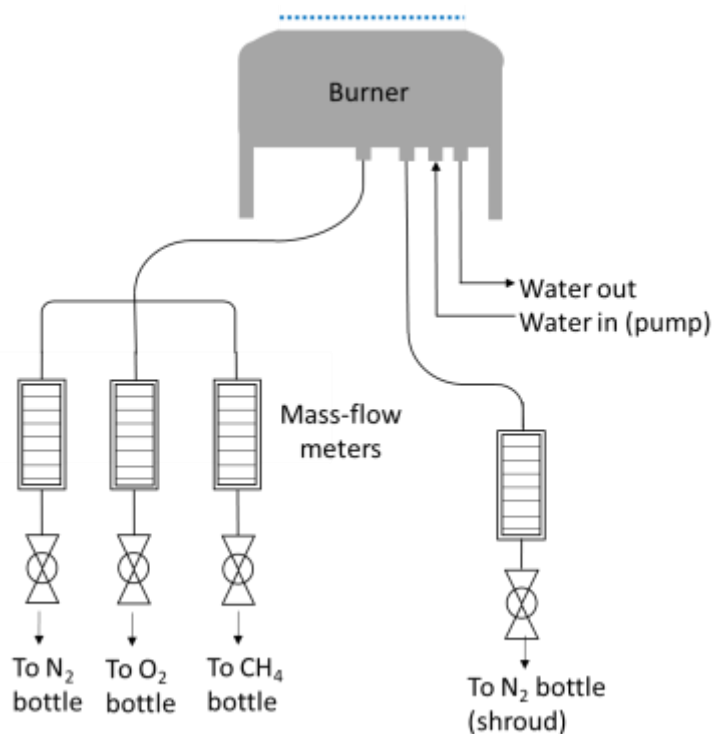
Figure 30. Schematic of the McKenna burner setup

3.3 Visualization

Two cameras simultaneously triggered by a delay generator and positioned orthogonally as shown in Figure 26 were used to visualize the ignition and combustion of the fuel droplets. A Photron SA4 camera coupled with an Infinity K2/DistaMax Long Distance Video Microscope and a CF-3 (close-focus) objective was used to record the change in diameter of the droplets at a framerate of 3600 fps, capturing any deformation, bubble formation, or micro-explosions during the ignition and combustion process. The droplets were backlit using a green LED light source (~532 nm) to prevent interference with the OH* detection of the second Photron camera. The Photron SA4 camera shown in Figure 32 (a) camera maintains a resolution of 1024 X 1024 pixels up to 3600 fps, and a reduced resolution up to 500,000 fps, making it beneficial for use with the K2 long-distance microscope employed in this study. The CF-3 objective fitted onto the K2 lens has a working distance of 95 mm - 122 mm, making it suitable for zooming and magnification of the droplets, while simultaneously maintaining a safe distance from the flat flame on the burner.
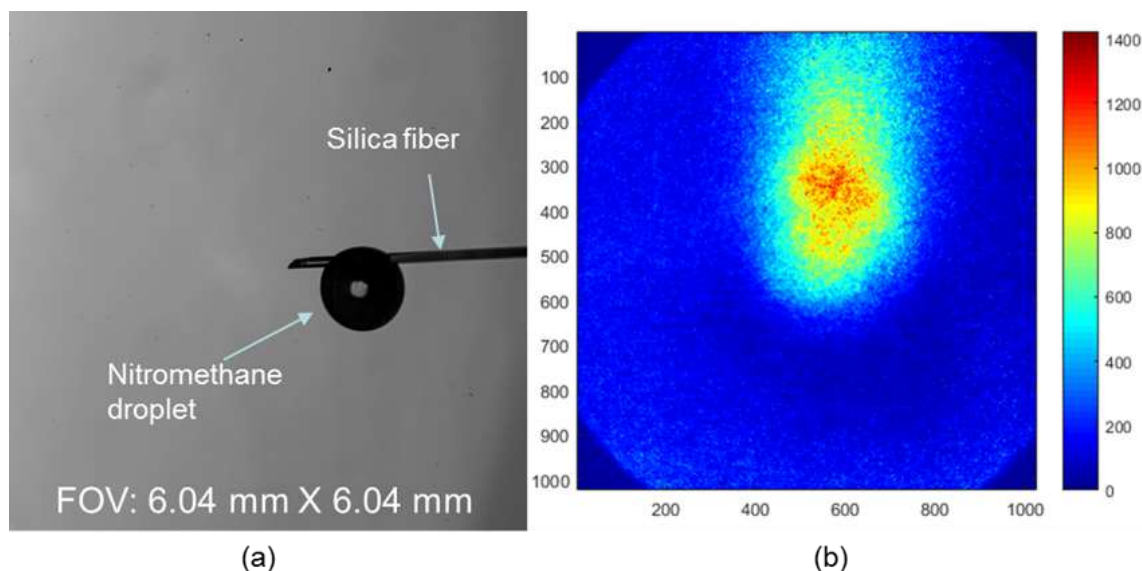
Figure 31. (a) Direct back-lit imaging of a burning NM droplet and (b) corresponding OH chemiluminescence imaging of a burning NM droplet

A second Photron SA-Z high-speed camera was used along with a LaVision High-speed IRO intensifier for OH* chemiluminescence. At maximum resolution (1024 X 1024), the Photron SA-Z camera offers frame rates up to 21000 fps, and higher frame rates are achievable (greater than 2 million fps) at reduced resolutions. The LaVision high-speed IRO coupled to the SA-Z camera is suitable for both low light and high speed imaging and is capable of gating times down to 10 ns and a spectral range of 190 – 800 nm. The coupled system was used with a UV lens and OH filter centered at 309 nm 20 nm to detect OH at the onset of droplet ignition and during droplet combustion. With the high-speed camera frame rate set to 3600 fps and a shutter speed of 276 µs, a high-speed controller was set to a constant gain of 65% and provided intensifier gates between 100 µs and 120 µs depending on the fuel being tested. To observe the flame structure of the droplets separately, a Nikon D500 digital single lens reflex (DSLR) camera was used along with a K2/DistaMax Long Distance Microscope fitted with a CF-3 objective lens at a frame rate of 60 fps.

Figure 32. Photron high-speed cameras used for (a) shadow back-lit images for droplet sizing and qualitative droplet behavior [74] (b) coupling with a high-seed intensifier for OH* chemiluminescence imaging [75]

3.4 Test Series

The test campaign focused on the effects of varying droplet diameter and temperature on the ignition and burner characteristics. Droplet diameters were changed by varying the distance that the syringe plunger was accurately pushed by a linear actuator, allowing a range of droplet diameters between 400 µm and 1.3 mm to be studied. Temperature was changed by adjusting the height of the droplet location above the center of the burner surface. This was done using a linear actuator to accurately raise the supporting silica fiber by the desired distance. The burner flame was maintained at an equivalence ratio of 0.51. At 2 in. above the burner, the droplets sustained a flame from ignition until the end of the droplet lifetime. At 5 in., the droplet exhibited occasional extinction and re-ignition. The shroud flow on the burner was adjusted to make the flow of combustion products as steady as possible. The test series also includes a preliminary study of the effects of unsteady flow on the ignition and combustion of the droplets. These tests were conducted at 8 in. above the burner, and droplets at this height showed cycles of ignition and extinction events throughout the droplet lifetime.

Table 4 summarizes the tests reported for this study. Test series 1 consisted of tests conducted at 2 in., 5 in., and 8 in. above the burner for each fuel. For this test series, the shroud flowrate was maintained at 5.6 lpm. At this shroud flowrate and 2 in. above the burner, droplets ignited and

burned steadily throughout the droplet lifetime. However, at 5 in. and 8 in. and a flowrate of 5.6 lpm, droplets exhibited a high frequency of ignition and extinction cycles during their lifetime. This behavior was attributed to the unsteadiness of the temporal temperature profile at these conditions evidenced by the unsteadiness of the CARS spectra measurements. Further discussion on the CARS measurements and effects of unsteady flow can be found in section 4.1 and section 4.6 respectively.

Test series 2 consisted of additional ignition and combustion tests for all fuels at 2 in. above the burner. In addition, the shroud flowrate was increased systematically to stabilize the temperature profiles at 5 in. and 8 in. above the burner. It was determined that at 5 in. above the burner, a shroud flowrate of 37.7 lpm provided the most stable temperature profiles. Though much fewer and further apart, ignition and extinction events were still observed for all fuels at this height. This condition was therefore termed 'quasi-steady'. At 8 in. above the burner, shroud flowrates higher than 37.7 lpm were found to have no effect on the unsteadiness of the flow. The shroud flowrate was therefore maintained at 37.7 lpm at this height, however since the temperature profiles were unstable, this condition was designated 'unsteady'.

Table 4. Test Series Summary

Test Series		Fuel	Height above burner (in)	N_2 Shroud gas (lpm)	Designation	Total # Tests
1	(a)	NM	2	5.6	steady	5
	(b)	NM	5	5.6	unsteady	6
	(c)	NM	8	5.6	unsteady	5
	(d)	IPN	2	5.6	steady	5
	(e)	IPN	5	5.6	unsteady	8
	(f)	IPN	8	5.6	unsteady	5
	(g)	Methanol	2	5.6	steady	5
	(h)	Methanol	5	5.6	unsteady	7
	(i)	Methanol	8	5.6	unsteady	5
2	(a)	NM	2	5.6	steady	6
	(b)	NM	5	37.7	quasi-steady	12
	(c)	NM	8	37.7	unsteady	13
	(d)	IPN	2	5.6	steady	5
	(e)	IPN	5	37.7	quasi-steady	13

Table 4 continued

	(f)	IPN	8	37.7	unsteady	13
	(g)	Methanol	2	5.6	steady	8
	(h)	Methanol	5	37.7	quasi-steady	12
	(i)	Methanol	8	37.7	unsteady	12
3,4,5	(a)	NM	2	5.6	steady	26
	(b)	IPN	2	5.6	steady	26
	(c)	Methanol	2	5.6	steady	22

3.5 Data Analysis

The data collected in this study consist of simultaneous high-speed back-lit videos and intensified high-speed OH* emission videos. The calibration of the fields of view is taken prior to each test series using a 0.25 mm spacing dot-card. Ignition delay was defined as the time that elapsed between when the flame-shield reached the middle of the burner above which the silica fiber was located, and the first observed signal of OH emission before a full flame was established around the droplet.

The back-lit images were analyzed using a MATLAB script originally developed at the Hypergolic Propellants Lab and modified for this experiment. For each image, an arbitrary crop window is specified by the user which eliminates the silica fiber from the images, also allowing sizing of the droplets during bubbling and deformation. The image is then processed using a canny filter and the edges of the droplet are detected as shown in Figure 33. The droplets vary in eccentricity, therefore an equivalent diameter is calculated as the diameter of a circle with the same surface area as the elliptical droplet. Figure 33 is an example of the typical sizing output showing a nitromethane droplet with a reported equivalent diameter of 1.38 mm and an eccentricity of 0.79.
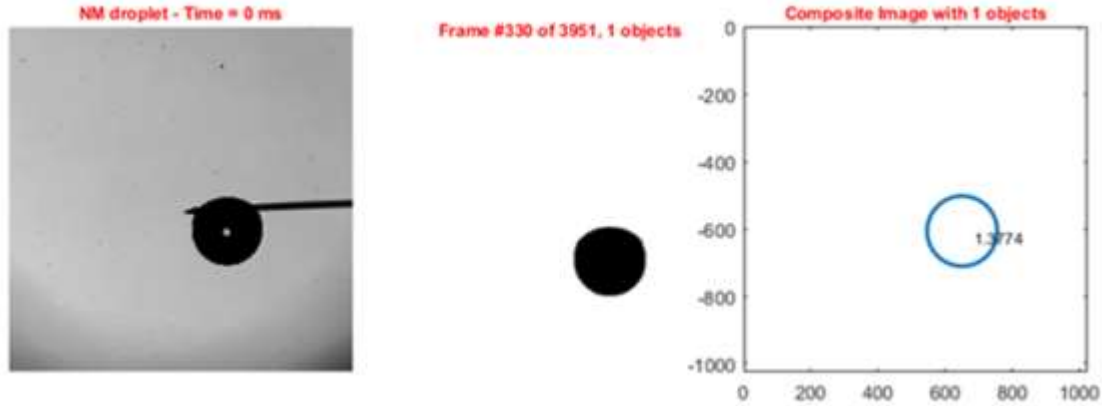
Figure 33. Example of the droplet sizing analysis output of a nitromethane droplet reporting a droplet size of 1.38 mm and an eccentricity of 0.79.

3.6   Uncertainty

The primary method of data collection in this study was high-speed imaging. The high-speed cameras were used to measure droplet sizes and ignition delay times. The sources of uncertainty in this study were therefore of two kinds: droplet sizing uncertainty and temporal uncertainty.

Droplet sizing uncertainty arose solely from the resolution of the high-speed videos. Using macro-extension tubes, K2 lens and CF-3 objective lens, calibrations of 0.0066 mm/pixel, 0.0055 mm/pixel and 0.0059 mm/pixel were achieved for test series 1, test series 2-3 and test series 4-5 respectively. This resulted in the droplet diameters having an uncertainty of ± 1 pixel corresponding to the appropriate calibration. The uncertainty in the droplet sizing resulted in uncertainty in the calculations of the burn rate (mm^2/s) from the slopes of the variation of the square of the droplet diameter with time.

The uncertainty in the ignition delay time, U_{IDT}, had three sources as shown in equation 14: the video framerate, the flame-shield withdrawal speed and the silica fiber location above the center of the burner.

$$U_{IDT} = \sqrt{\left(U_{fr}\right)^2 + \left(U_{fs}\right)^2 + \left(U_{fiber}\right)^2}$$

(14)

As mentioned previously, ignition delay was defined as the time elapsed from exposure of the gases (represented by the flame-shield reaching the location of the silica fiber above the center of the burner surface) and the detection of an OH signal. To characterize the flame-shield withdrawal, 10 high-speed videos of the flame-shield crossing the location of the edge of the silica fiber were taken between test series. The times and uncertainties in the time it took for the flame-shield to cross the edge of the silica fiber, U_{fs}, were 92.1 ms $\pm$ 306 µs for test series 1, 93.4 ms $\pm$ 291 µs for test series 2 and 3, and 96.9 ms $\pm$ 304 µs for test series 4 and 5.

Secondly, two different diameter silica fibers were used to suspend the droplets depending on the size, requiring a change of the silica fiber during the tests. Though a conscious effort was made to ensure that the silica fiber remained in the exact position each time, a slight offset from the center location may have occurred and was assumed in this study to be $\pm$ 1 pixel. This offset would have slightly further affected the time it took for the flame-shield to cross the location of the silica fiber. This added uncertainty, U_{fiber}, was assumed to be $\pm$ 9 µs (9 µs/pixel), calculated from the average speed of the flame-shield across the field of view. Lastly, the uncertainty in the temporal measurements from the high-speed videos, U_{fr}, was assumed to be $\pm$ 1 frame. With both high-speed cameras operated at 3600, the uncertainty is $\pm$ 278 µs. In general, the uncertainty in the ignition delay measurements was less than $\pm$ 600 µs. The uncertainties in the ignition delay as well as the droplet sizes are absorbed into the size of the symbols used.

4. RESULTS AND DISCUSSION

This chapter discusses the experimental results as they relate to the objectives of this study. Section 4.1 discusses the process of the characterization of the McKenna burner for the droplet experiments. Section 4.2 summarizes qualitative observations of the flame structures of IPN and NM. Section 4.3 discusses the findings on the effect of droplet size on the ignition delays and burning rates of methanol, IPN and NM droplets, while Section 4.4 examines the effect of ambient temperature. Qualitative droplet behavior is discussed in Section 4.5 and the effect of unsteady flow at 5 in. and 8 in. heights above the burner is examined in Section 4.6. Comparison of the experimental results with theoretical ignition delay and burning rate models is presented in Sections 4.7 and 4.8, respectively.

4.1   Burner Characterization

As discussed previously, a McKenna burner was used to provide the hot gases in which the fuel droplets ignited and burned. A number of methods were considered for producing the high temperature environment required for this study including the use of a nichrome wire. However, it was determined that the controllable environment provided by the McKenna burner would be most suitable, as it has the potential to provide steady and unsteady flow with varying mean temperature.

The equivalence ratio of the flat flame could be varied to obtain different oxidizer concentrations in the post-combustion gases. By keeping the nitrogen and methane flow rates constant and changing the oxygen flow rates, a series of conditions could be tested to select a suitable flame and equivalence ratio based on the flame stability and oxidizer concentration in the post-combustion gases. In Table 5, conditions 1 through 8 were found to produce stable flat flames. Conditions 9 – 14 exhibited instabilities in the flame as shown in Figure 34, which increased with an increase in the oxygen flow rate. Condition 7 was selected for the current study ($\varphi = 0.51$), because out of the most stable flat flames, this condition represented the highest oxygen concentration that could be achieved. Calculations using COSILAB and CEA predicted an oxygen concentration of ~13% in the post-combustion gases at this condition.

Table 5. McKenna burner conditions

Condition	%O_2-N_2	N_2 (lpm)	O_2 (lpm)	CH_4 (lpm)	ϕ	T_{ad} (CEA)	%O_2 (CEA)
1	21-79	18.17	4.83	1.93	0.8	1994	3.705
2	23.2-76.8	18.17	5.5	1.93	0.7	1953	6.242
3	24.8-75.2	18.17	6	1.93	0.64	1923	8.068
4	25.7-74.3	18.17	6.3	1.93	0.61	1909	9.102
5	27.5-72.5	18.17	6.9	1.93	0.56	1886	11.04
6	28.4-71.6	18.17	7.2	1.93	0.53	1857	12.21
7	29.2-70.8	18.17	7.5	1.93	0.51	1846	13.14
8	30-70	18.17	7.8	1.93	0.49	1829	14.07
9	30.6-69.4	18.17	8	1.93	0.48	1826	14.62
10	31.3-68.7	18.17	8.3	1.93	0.46	1805	15.61
11	32.1-67.9	18.17	8.6	1.93	0.44	1781	16.63
12	32.8-67.2	18.17	8.9	1.93	0.43	1781	17.33
13	33.6-66.4	18.17	9.2	1.93	0.42	1780	18.05
14	35.5-64.5	18.17	10	1.93	0.38	1727	20.46
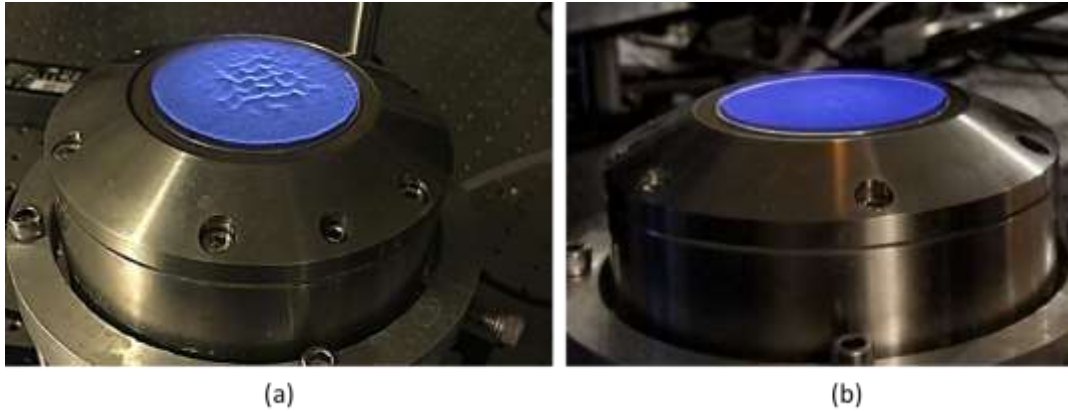
Figure 34. (a) Example of flat flame instabilities observed for conditions 9 – 14; (b) Example of stable flat flames observed for conditions 1 - 8

In the literature, droplet ignition and combustion characteristics have been shown to have a strong dependence on ambient temperature, therefore having an accurate measurement of temperature is critical. Previous droplet ignition and combustion experiments have exclusively used thermocouples to measure either the ambient temperature surrounding a droplet or the droplet temperature. Therefore, to initially characterize the temperature in the post-combustion gases, R-type and K-type thermocouples were positioned approximately 0.59 in. to 1.18 in. above the

surface of the burner. However, thermocouple readings corrected for radiation losses were consistently too low (~1400K – 1500 K) for that proximity to the flat flame. Consequently, an important objective of this study was to obtain accurate and repeatable temperature measurements of the post-combustion gases above the flat flame of the burner. To this end, coherent anti-Stokes Raman spectroscopy (CARS) was selected to characterize the temperature at specific locations above the burner surface where the droplets would be positioned. Since the burner is not enclosed, it is convenient to apply laser diagnostics to investigate the droplet environment.

CARS is a nonlinear spectroscopy technique that has been extensively employed for temperature and species concentration measurements in various applications due to its excellent accuracy and precision [76]. In this study, a vibrational CARS system similar to that described by Han et. al [77] was used for temperature measurements in the post-combustion gases of the McKenna burner. At each measurement location above the burner surface, 1000 single-laser shots were obtained and processed to obtain mean temperature and temperature statistics.

For each height above the burner, experiments were repeated multiple times on different days to assess the repeatability of the results. In addition, the flow rate of the shroud gas (nitrogen) was adjusted systematically for the 5 in. and 8 in. positions to obtain the most stable conditions, represented by the degree of the standard deviation of the CARS measurements obtained. A standard deviation of up to 3% is expected from the intrinsic noise of the laser system, therefore the degree of standard deviation above this value determined the designations shown in Table 4.

At 2 in. height above the burner, shroud flowrates of 5.6 lpm and 10 lpm showed no difference in the stability of the CARS spectra and the standard deviation of the CARS temperature measurements was very small (4% of the mean temperature). This condition was therefore designated as 'steady', and a shroud flow rate of 5.6 lpm was chosen for the droplet tests. Figure 35 (a) shows the histogram of the temperature obtained from 1000 CARS spectra acquired at 10 Hz, 2 in. above the burner surface. Each shot or spectrum obtained was fitted and a temperature extracted from the shape of the spectrum to form the histogram shown. The unimodal shape of the histogram shows the stability of the temperature at this height. In Figure 35 (b), the 1000 raw spectra were first averaged, then fitted to extract an average temperature of all 1000 shots. The

mean temperature obtained (1660 K) was well within the standard deviation of the mean temperature obtained from the histogram.
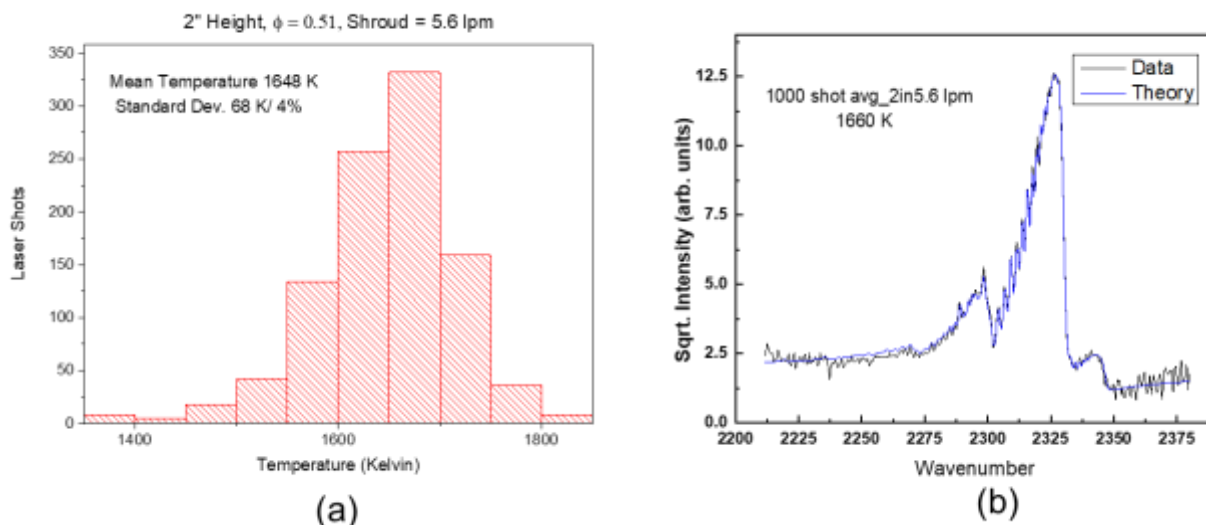
Figure 35. (a) Temperature histogram (1000 shots) at 2" above the burner; (b) Fit of the average spectra of 1000 shots at 2" above the burner

For the 5 in. height, shroud flowrates ranging from 5.6 lpm to 50 lpm were tested, and it was determined that the most suitable shroud gas flowrate for that height was 37.7 lpm, because it had the smallest variability in the temperature, with a standard deviation of 17.5% and a mean temperature of 1337 K. Figure 36 shows the histogram of temperature measurements from each individual spectrum and the fit for the average spectra. Once again, the histogram has a narrow unimodal shape indicative of relatively steady CARS measurements at that height. This flowrate minimized the unsteadiness of the flow resulting from entrainment of the ambient air. However, based on the relatively large standard deviation compared to the 2 in. case, this condition was termed 'quasi-steady'. After a similar procedure was performed for 8 in. above the burner, maintaining the shroud flowrate at 37.7 lpm was found to be most suitable, however this height above the burner showed the most unsteady behavior. Therefore, droplet tests performed at this height were used to investigate the effect of flow unsteadiness on the combustion characteristics of the droplets. Unsteady effects are discussed in more detail in section 4.6.
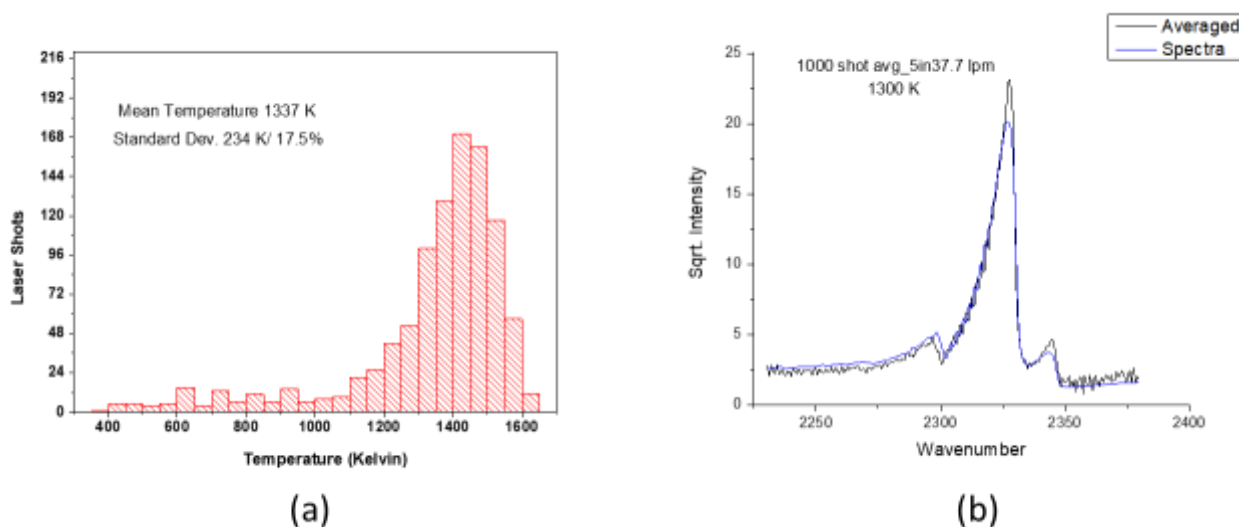
Figure 36. (a) Temperature histogram (1000 shots) at 5 in. above the burner; (b) Fit of the average spectra of 1000 shots at 5 in. above the burner

4.2   Flame Structure Observations of IPN and NM

Qualitative observations of flame structure were made using a Nikon DSLR camera and a K2 lens. Though clear intensity jumps could be observed at the flame location, attempts to extract flame stand-off ratio were unsuccessful due to the difficulty in obtaining droplet size measurements from the videos obtained at a frame rate of 60 fps.

After the quick withdrawal of the flame shield, IPN droplets ignited and burned with a white-yellow luminous flame. The videos also showed three regions as described by Ambekar et. al [78] for IPN droplet combustion tests for droplet diameters between 0.79 mm and 1.9 mm as shown in Figure 18. For the current study, the three regions are shown in Figure 37 (a), beginning with a dark inner zone where vaporization of the droplet occurs. However, rather than a bluish-violet inner flame [4], a whitish-colored inner monopropellant flame was observed for IPN, marking zone II where IPN decomposition occurs. Separated from the inner flame by a thin dark region, a second outer blue-violet bipropellant flame (zone III) was observed. In a study on the flame decomposition of propyl nitrates, Powling and Smith [79] measured the major IPN decomposition products to be CH_3CHO, CH_3NO_2, CH_3OH, H_2CO, NO, CO and CH_4. In a later study, Morin and Bedjanian [80] observed that the thermal decomposition of IPN begins with the breaking of the $O-NO_2$ bond, forming NO_2 and the isopropoxy radical $(CH_3)_2CHO$, which then

decomposes to form CH_3 and CH_3CHO (acetaldehyde). The bipropellant flame is a result of the decomposition products of the inner monopropellant flame reacting with the ambient oxygen.
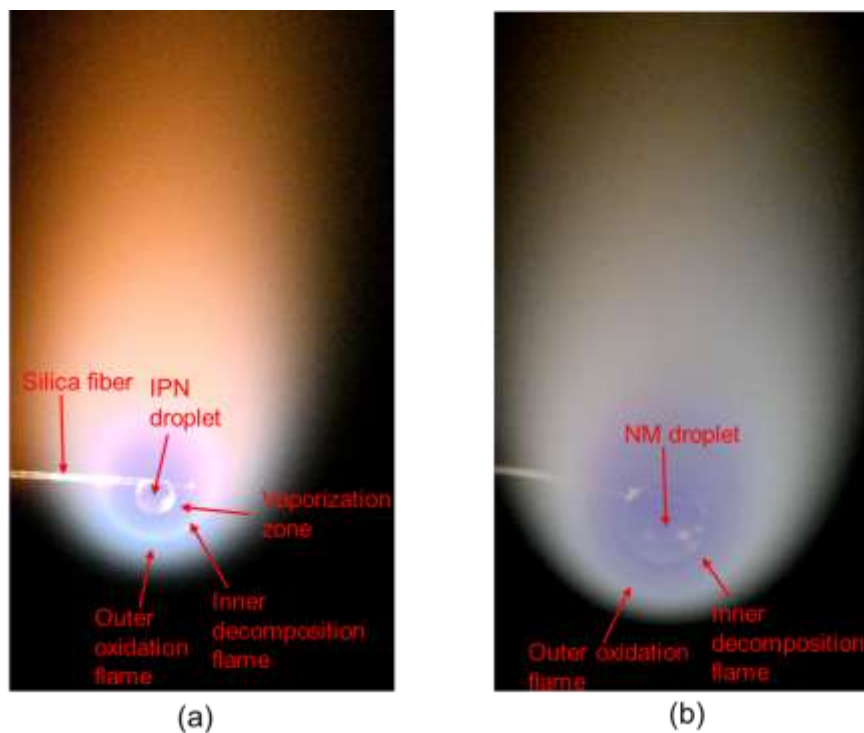
Figure 37. (a) Double flame structure of a burning IPN droplet; (b) Double flame structure of a burning NM droplet

NM droplets visibly exhibited a yellow flame, but less luminous compared to IPN. Similarly to IPN, NM showed a double flame structure as seen in Figure 37(b), not previously observed by other investigators [78]. A dark inner region marks the presence of NM vapor as the NM droplet evaporates. This region is followed by a bluish-violet inner decomposition flame, separated by a thin dark region from a second outer more luminous monopropellant flame. Research on the kinetics of NM decomposition postulate that the decomposition process proceeds from the bond fission of C-N to form CH_3 and NO_2. Studies on the decomposition of NM have shown that the main NM decomposition products are NO, HCN, CO_2, CH_2O and H_2O, with smaller quantities of CO, CH_4 and N_2O. These decomposition products then proceed to react with the ambient oxygen at the bipropellant flame.

4.3   Effect of Initial Droplet Size on Ignition and Combustion Characteristics

For each of the three fuels, droplet sizes in the range 0.35 mm to 1.4 mm were tested. The following sections discuss the ignition delay and burn-rate results from varying the initial droplet size. Since the effect of initial droplet size was to be isolated, the ambient temperature for these tests and location of the droplet above the burner surface was kept constant at ~1650 K and 2 in. above the burner surface respectively. In Table 4, the tests reported in this section correspond to test series 1(a), 1(d) and 1(g), test series 2(a), 2(d), and 2(g), and test series 3, 4, and 5.

4.3.1   Ignition Delay Trends

Ignition delay times were measured with the apparatus shown in Figure 27. After the flat flame was lit, the delay generator simultaneously triggered two cameras and the flame shield to withdraw and expose the suspended droplet to the post-combustion gases of the flat flame. The ignition delay time was defined as the time that elapsed between when the flame shield passed the center of the burner over which the tip of the silica fiber was suspended, and the first appearance of the OH signal recorded by the intensifier and high-speed camera. The time it took for the flame shield to pass the center point of the burner was approximately 92 ms. As discussed in section 3.6, the uncertainty in the ignition delay measurements was less than ± 600 µs. In addition, both the uncertainties in the ignition delay as well as the droplet sizes are absorbed into the size of the symbols used. Figure 38 shows the ignition sequence of an IPN droplet with an initial diameter of 1.01 mm. At 2 in. above the burner surface, droplet ignition was observed to always occur below the droplet for all fuels. This has been attributed to natural convection effects, where hot fuel vapor evaporating from the droplet descends downwards, causing reactions to be initiated between fuel vapor and ambient oxidizer below the droplet.
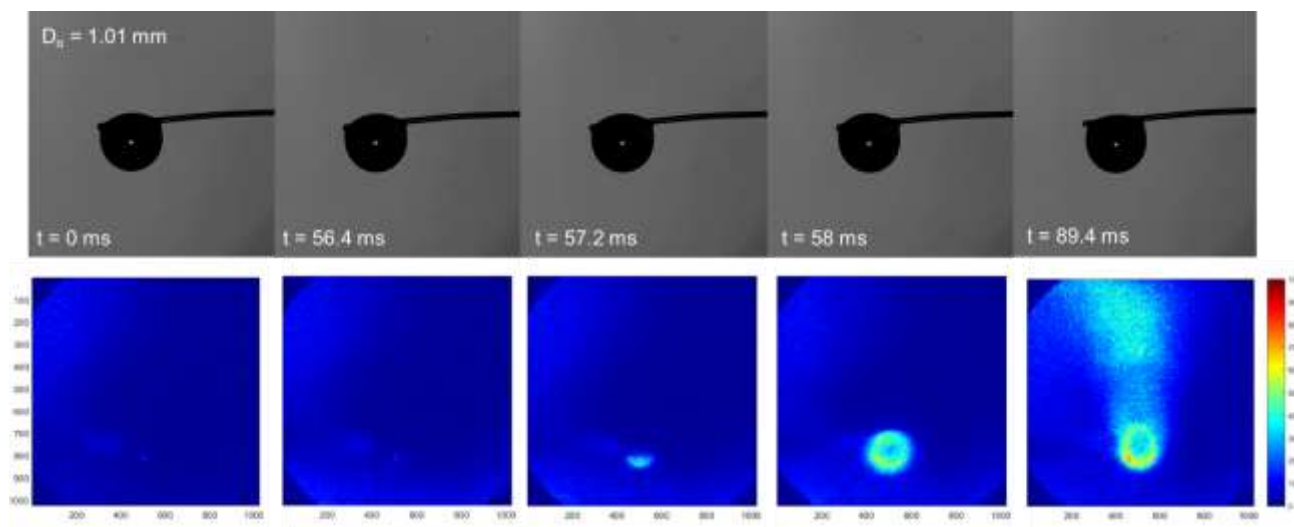
Figure 38. Sequence of shadow and OH signal images showing the ignition of an IPN droplet
(D_o = 1.01 mm) and an ignition delay of 56.6 ms

Figure 39, Figure 40 and Figure 41 show measured ignition delays for suspended methanol, NM and IPN droplets respectively, at ~1650 K average ambient temperature and atmospheric pressure. As mentioned before, the different test series were performed on different days to assess the repeatability of the experiment. Test series 1 reported here was preliminary and conducted a month before the rest of the test series, and there may have been an experimental error associated with the results from that test series. As observed in majority of the data presented for droplet ignition delay versus initial droplet diameter, there is a slight scatter in the data for all three fuels, suggesting that the scatter is likely a function of the ambient conditions. The scatter at this height (2 in.) could be largely due to the small possible range of ambient temperatures that may have been experienced by reacting droplets. Though the CARS measurements were very stable, the droplets may have experienced ambient temperatures within 4% (68K) of the recorded mean temperature. A comparison can be made to n-heptane (boiling point 371.5 K), which has a comparable boiling point to both NM (373 K) and IPN (374 K). Results by Saitoh et al. [32] on 1-2 mm n-heptane droplets shown in Figure 5, and by Takei et. al [23] for 0.5-1.4 mm n-heptane droplets in Figure 2 show that a difference in ambient temperature as small as 25 K or C can have a notable effect on the ignition delay for similar droplet sizes.
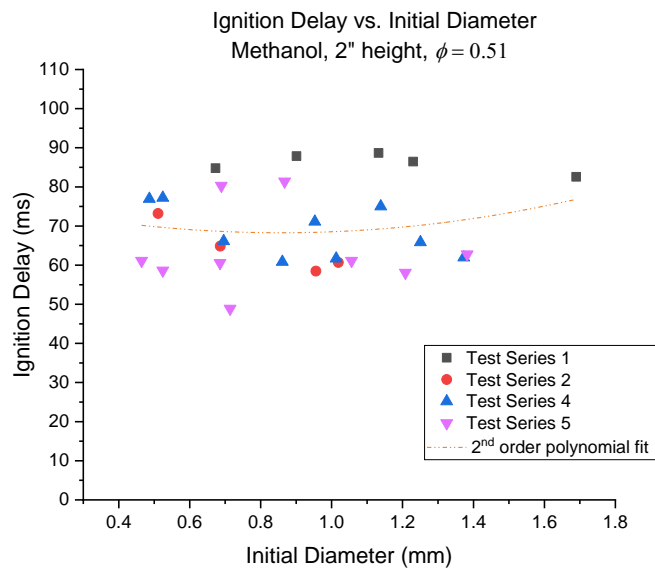
Figure 39. Ignition delay variation with initial droplet diameter for suspended methanol droplets at 2 inches above the burner surface
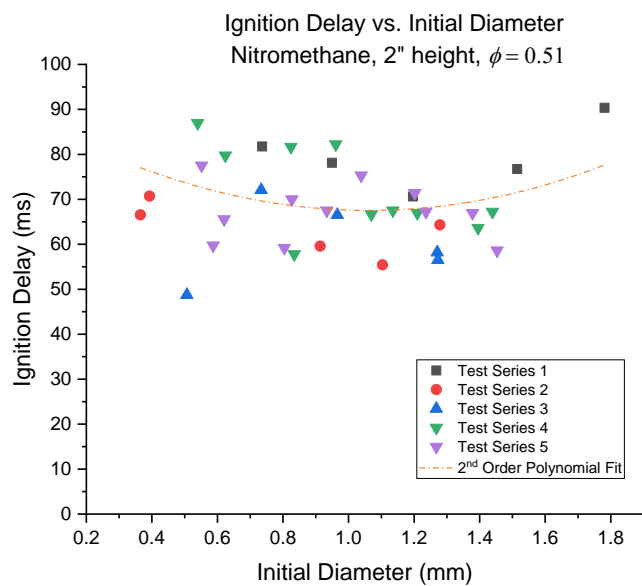
Figure 40. Ignition delay variation with initial droplet diameter for suspended nitromethane droplets at 2 inches above the burner surface
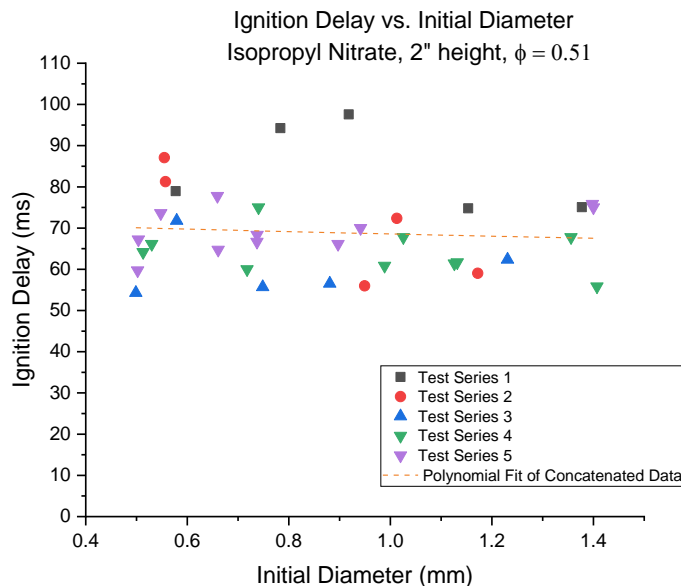
Figure 41. Ignition delay variation with initial droplet diameter for suspended isopropyl nitrate droplets at 2 in. above the burner surface

Ignition delay results from all the test series for all three fuels at this height (2 in. above the burner surface) and mean temperature showed no significant variation in the ignition delay with increasing droplet diameter. A similar trend was observed by Takei et. al [23] for 0.5-1.4 mm n-heptane droplets igniting in an ambient temperature of 1023 K. This could be attributed to the fact that at higher temperatures, reaction rates are extremely fast compared to vaporization or diffusion rates. Therefore, high temperatures are associated with ignition and burning in the diffusion-controlled regime. However, at very high temperatures, very little heating up of the droplet occurs before it ignites, and the physical processes of droplet heating and vaporization do not play a very important role. Consequently, ignition delay becomes invariant with changes in the initial droplet diameter. This could also explain the lack of significant difference between the ignition delays observed by the fuels despite the lower boiling point of methanol (64.7) compared to NM (101.1°C) and IPN (101.5°C). For the range of droplets studied for all three fuels at this condition, the ignition delays measured were between approximately 55 ms and 90 ms, showing no significant difference between the fuels.

Because $t = 0 \, s$ was taken as the time at which the flame shield reached the middle of the burner surface as it drew back, there may exist a small delay between when the flame shield is withdrawn and when the hot combustion gases come into contact with the droplets. However, because density drastically decreases across the flame due to significantly higher temperatures, gas velocity also significantly increases, therefore this delay is assumed negligible in this study. Additional diagnostics such as CARS at faster frequencies can be used to measure the temporal evolution of the temperature profile at a location just below the droplet.

Though several large scale ignition studies have been done for gaseous IPN and NM in reactors and shock tubes [81–84], to the author's knowledge, no experimental data on NM and IPN droplet ignition has been reported. Though it is difficult to make direct comparisons with other experiments due to differences in experimental techniques and conditions, a brief summary of selected studies have been outlined in Table 6.

Table 6. Summary of selected ignition studies and fuels

Ref	Authors	Fuels	Droplet sizes (mm)	ID	Exptl. Method	Ambient Conditions
[6]	Faeth and Olson	n-heptane	0.9 mm -1.65 mm	~0.6 s - 0.8 s	Suspended, gf;	950 K
[6]	Faeth and Olson	n-hexadecane	0.9 mm -1.65 mm	~0.5 s - 1.2 s	Suspended, gf;	950 K
[28]	Long and Grens II	n-heptane	0.2 mm - 0.6 mm	~124 ms - > 2 s	Suspended	773 K - 1013 K
[32]	Saitoh et al.	n-heptane	0.8 mm - ~ 2 mm	~0.4 s - 2 s	Suspended	923 K - 1023 K
[32]	Saitoh et al.	n-hexadecane	~0.6 mm - ~2 mm	~0.3 s - ~1s	Suspended	973 K - 1073 K
[23]	Takei et al.	n-heptane	~0.4 mm - 1.4 mm	~0.3 s - ~0.7 s	Suspended	949 K - 1023 K
[23]	Takei et al.	n-hexadecane	~0.4 mm - 1.4 mm	~0.3 s - ~0.8 s	Suspended	950 K - 1023 K
[34]	Nakanishi et al.	n-hexadecane	0.35 mm - 1.4 mm	~0.45 s - ~1.7 s	Suspended	850 K - 950 K
[34]	Nakanishi et al.	n-heptane	0.8 mm - 1.4 mm	~0.4 s - 1.5 s	Suspended	900 K - 950 K
[35]	Sangiovanni and Kesten	butyl alcohol	0.2 mm - 0.3 mm	0.005 s - 0.020 s	injection	1240 K - 1680 K
[35]	Sangiovanni and Kesten	furfuryl alcohol	0.2 mm - 0.3 mm	0.005 s - 0.030 s	injection	1241 K - 1680 K
[85]	Faeth et al.	PGDN	0.8 mm - 2 mm	~0.6 s - ~2.4 s	Suspended	813 K
[46]	Wood and Charvonia	triethylamine (in WFNA vapor)	2.6 mm - 4.2 mm	~0.03 - 0.04 s	free-falling	623 K - 773 K
[29]	Gregory and Calcote	RFNA (in hydrazine vapor)	~1.84 mm	~0.083 s	free-falling	408 K
	Current Study	IPN	0.35 mm - 1.4 mm	~0.055 s - ~0.190 s	Suspended	~1330 K, ~1650 K
	Current Study	NM	0.35 mm - 1.4 mm	~0.055 s - ~0.190 s	Suspended	~1330 K, ~1650 K
	Current Study	Methanol	0.35 mm - 1.4 mm	~0.055 s - ~0.260 s	Suspended	~1330 K, ~1650 K

*gf: gravity-free
*PGDN: propylene glycol dinitrate

In the literature, there is scarce experimental data on droplet ignition at very high ambient temperatures (> 1200 K). For droplet sizes in the same range as the current study, n-heptane and n-hexadecane droplets in the literature report ignition delays an order of magnitude higher than those in the current study for slightly lower temperatures. For a larger range of droplet sizes and lower ambient temperatures (< 800 K) than the current study, ignition delays for hypergolic droplets were found to be on the same order of magnitude with the ignition delays obtained in the current study [28, 45].

As droplet diameter decreases beyond the range studied, and therefore more closely resembles droplet sizes in the dilute regions of a practical spray, two possible trends could be observed. The first would be that ignition delay would remain invariant with droplet size as droplet size decreases, until a critical droplet size is reached where ignition would not take place, due to the insufficiency of fuel vapor near the droplet for reactions with the ambient oxygen to occur. The second possible trend would be that as droplet size decreases beyond a certain size, ignition delay would begin to decrease until a critical droplet size beyond which ignition would not take place. A plausible argument for this trend is that since mass flux increases with decreasing droplet diameter, a sufficient amount of fuel vapor for reaction will be available quicker for smaller droplet sizes, causing a reaction (and eventual ignition) to be initiated sooner. The likelihood of ignition delay to begin to increase below a certain droplet size in these conditions is low due to the high ambient temperature surrounding the droplets at this height, in which kinetic effects can be considered negligible.

Having a comparable boiling point to both NM and IPN, computational results by Awasthi et al. [86] for n-heptane droplets at atmospheric pressure and an ambient temperature of 1600 K, predicted a more or less constant ignition delay time of approximately 0.5 ms for droplet sizes between 0.4 mm and 1 mm as shown in Figure 42. This value is approximately two orders of magnitude below the current methanol, NM and IPN results. Below ~0.4 mm, ignition delay was predicted to decrease until a critical droplet size was achieved at this ambient temperature. Though a one-to-one comparison cannot be made, the computational ignition delay results also report ignition delays approximately two orders of magnitude lower than those reported in the current study at a similar ambient temperature (1600 K).
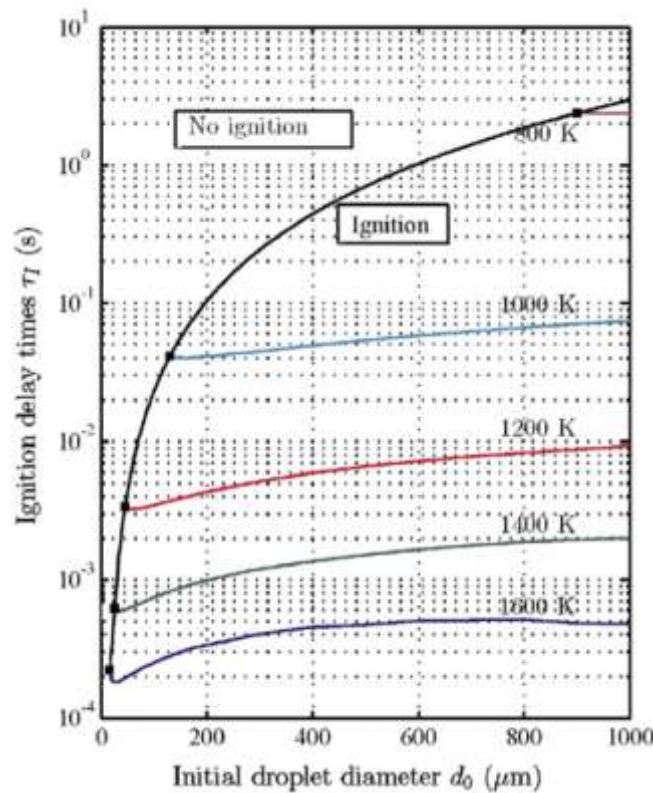
Figure 42. Computational ignition delay vs. initial droplet diameter results for n-heptane droplets in varying ambient temperatures at atmospheric pressure [86]

4.3.2   Burn rate Trends

Typical trends for non-dimensionalized droplet diameter history for nitromethane are shown in Figure 43. These trends were typical for all the fuels investigated in this study, except for periods of bubbling and deformation towards the end of the droplet lifetimes, where equivalent square droplet diameter varied nonlinearly with time. Overall, in the size range studied, the droplets exhibited D^2 Law behavior where after a short droplet heat-up period, the square of the droplet diameter decreased linearly with time.
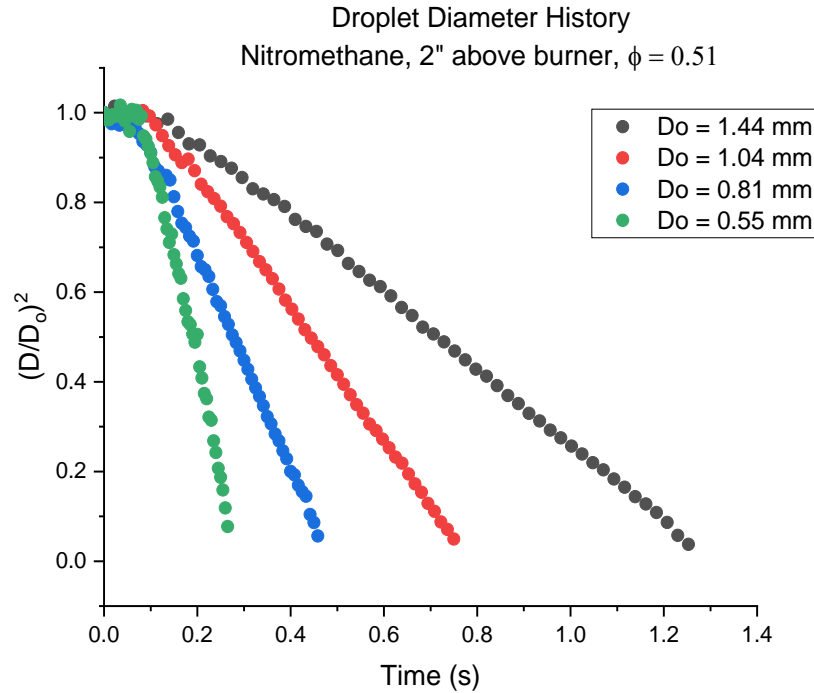
Figure 43. Trends for non-dimensionalized square of droplet diameter with time for selected representative droplet sizes for pure nitromethane at 2 in. above the burner surface

The experimental burning rate constant for each droplet was obtained from the linear region of these curves. Figure 44,Figure 45 andFigure 46 show the variation of burn-rate constants with initial droplet diameter for methanol, NM and IPN, respectively, at ~1650 K ambient temperature and atmospheric pressure. The correlation coefficient, , is used here to determine the strength of the linear relationship between droplet diameter and burning rate constant, while the coefficient of determination is used to determine the variation in the burning rate constant data from a linear fit of burning rate constant vs. initial droplet diameter. In general, for all three fuels, burning rate constants were shown to increase with initial droplet diameter in the size range studied as expected. Monaghan et al. [37] suggested two major contributing factors to this observation. It was suggested that initially larger droplets absorb more heat from the hot ambient environment, causing them to burn faster than initially smaller droplets. Another major contributing factor is the influence of natural convection. Because initially smaller droplets have a shorter burning time as well as a smaller volume of combustion products surrounding the droplets, the effect of natural convection on the burning rate will be low to negligible compared to larger droplets. The influence of natural

convection effects is much greater for initially larger droplets, causing burning rates to increase as droplet size increases.

The majority of the tests series for methanol showed good repeatability except for test series 1, where slightly higher burning rate constants were measured. As mentioned previously, test series 1 was a preliminary test series conducted a month prior to the rest of the test series, and this discrepancy is suspected to be a result of a systematic error associated with the test series. For test series $2-5$, the methanol burning rate constants for droplet diameters between 0.4 mm and 1.4 mm were observed to increase approximately linearly from ~1 mm^2/s to ~1.4 mm^2/s. A linear fit through test series $2-5$ for methanol droplets reported an r value of 0.78 and an r^2 value of 0.61, showing a strong linear relationship and a moderate variation in the data from the linear fit. A slope of 0.44 mm/s was also reported for this linear fit. A separate linear fit through test series 1, reported r and r^2 values of 0.95 and 0.91 respectively, as well as a slope of 0.6 mm/s indicating that the rate of increase of the burn-rates with droplet diameter were higher for test series 1 than for the rest of the test series. The burning rate constant values obtained for test series 2, 4 and 5 were comparable to those obtained by Ambekar et. al [78] for pure methanol droplets ignited using a spark. For droplet sizes between 1 mm and 2 mm, Ambekar et. al obtained pure methanol burning rate constant values ranging between 0.7 mm^2/s and 1.2 mm^2/s. However, they did not report ambient temperature measurements for their experiments.
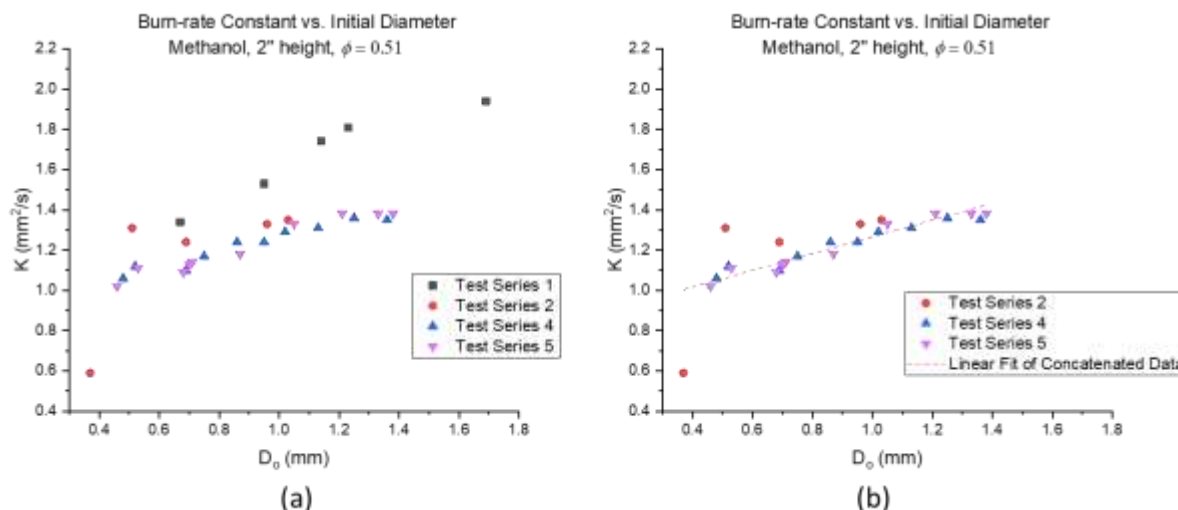
Figure 44. Burn-rate constants for methanol droplets burning 2 in. above the burner surface (a) test series 1-5 (b) linear fit through test series 2-5

NM droplets also exhibited a moderate increase in burning rate constant with increasing initial droplet diameter as shown in Figure 45. In general, good repeatability was shown between the different test series with the exception of test series 1 and 3, which showed slightly higher burning rate constants. Tests 2, 4 and 5 showed good agreement with each other, reporting burning rate constants ranging between ~1.2 mm^2/s and ~1.8 mm^2/s for the droplet size range tested as shown in Figure 45. A linear fit through test series 2 - 5 reported an r value of 0.9 and an r^2 value of 0.81, showing both a good linear correlation and a relatively small variation of the data from the linear fit. The slope of the linear fit was 0.34 mm/s. A second linear fit through test series 1 and 3 reported an r value of 0.78 and an r^2 value of 0.61. Though a strong linear correlation is found between the burning rate constant and the initial droplet diameter as expected, there is a moderate variation form the linear fit. The slope of the linear fit for test series 1 and 3 was 0.4 mm/s, showing that though the burning rate constants for test series 1 and 3 were significantly higher than the rest of the test series, the rate of increase of burning rate with increasing initial diameter was consistent. Burning rate comparisons with existing data from the study of the combustion of droplets of pure NM and NM blends [78] showed that the current study's burning rates were almost double those reported by Ambekar et. al. For a range of droplet sizes between 0.8 mm and 2.2 mm, burning rate constants between ~0.8 mm^2/s and ~1.2 mm^2/s were reported in [78]. However, as stated before, the ambient temperatures were not reported for those experiments. One possible explanation for

the large difference in burning rates could be the effect of forced convection from the post-combustion gases produced by the burner in the current study. In the study by Ambekar et. al, a spark created between two steel electrodes was used to ignite droplets in quiescent air, providing a localized hot temperature region in which the droplets ignited and burned. In the spark ignition setup, convection effects were limited to natural convection. In the current study, forced convection effects from the post-combustion gases more closely simulated the conditions in a combustor and are known to contribute significantly to the increase in burn-rates of fuel droplets.
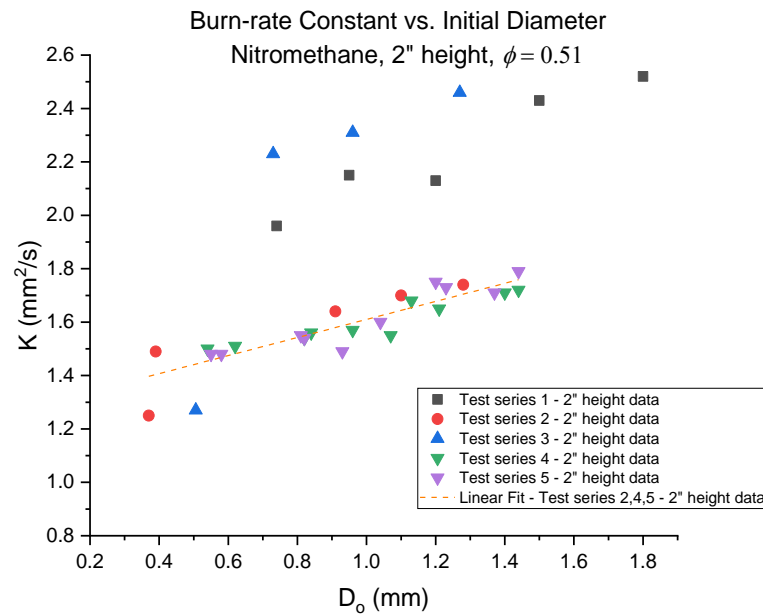
Figure 45. Burn-rate constants for NM droplets burning 2 in. above the burner surface

The burning rate constant trends for IPN droplets are shown in Figure 46. For IPN, all the test series showed good agreement with each other. For initially smaller droplets (D_o < ~0.8 mm), droplets prematurely detached from the silica fiber during combustion due to deformation. When the droplets became very deformed and only a small area of the droplet was attached to the silica fiber, droplet surface tension forces caused the droplet to form a sphere detached from the silica fiber. Deformation behavior is discussed in more detail in Section 4.5.3. Simultaneous shadow and OH videos showed that the droplet continued to burn as it moved upwards with the post-combustion gases and out of the field of view. Though ignition delay measurements could be

obtained, burning rate constants could not be calculated for these tests where the droplets detached. For droplets with initial diameters between ~0.8 mm and 1.4 mm, burning rate constant trends showed a significant increase with increase in initial droplet diameter, and ranged between ~1.4 mm^2/s and ~2.2 mm^2/s. A linear fit of the data from test series $1 - 5$ reported an r value of 0.85 and an r^2 value of 0.72 showing a strong linear correlation. The slope of the linear fit was reported to be 0.8 mm/s. Comparisons with Ambekar et. al [2] showed that the current study measured significantly higher values of burning rates compared to their spark ignition study. For droplet diameters between 0.8 mm and 2.2 mm, Ambekar et. al obtained burning rate constants between 0.5 mm^2/s and 1.4 mm^2/s. As mentioned before, this is likely due to the effects of forced convection from the post-combustion gases in the current study and a possible difference in the ambient temperature surrounding the droplets.
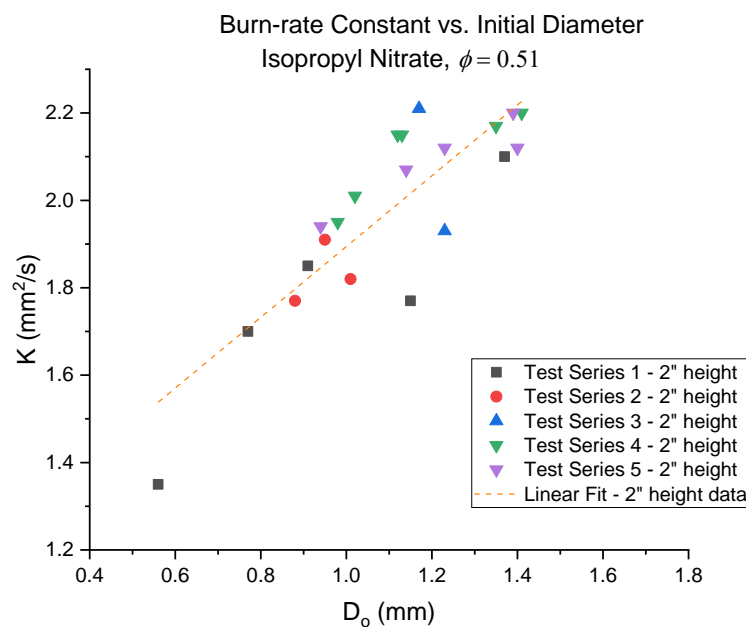
Figure 46. Burn-rate constants for IPN droplets burning 2" above the burner surface

Out of all three fuels, IPN droplets were shown to have the highest burning rate constant values for the range of droplet sizes studied here, as well as almost double the rate of increase in

burning rates with increasing droplet diameters (0.8 mm/s in comparison with 0.44 mm/s and 0.34 mm/s for methanol (test series 2-5) and NM (test series 2-5) respectively). A significant increase in the burning rate constant with increasing initial diameter was also observed by Ambekar et al. for IPN [2]. The investigators also found that IPN burning rates were strongly influenced by initial droplet diameters, and increased by ~280% for a range of diameters between 0.79 mm to 1.97 mm. No qualitative explanation however, was given for these observations. These results suggest that not only do IPN droplets burn faster than both NM and methanol droplets, but in addition, the effect of natural convection to increase the burning rate for larger droplets is greater for IPN than it is for methanol and NM. NM burning rate constants were found to be slightly higher than those obtained for methanol. A similar observation was reported by Ambekar et al. [78] for a droplet diameter of 1.24 mm.

4.4   Temperature Effects

As mentioned previously, the ambient temperature was varied by changing the height of the droplet above the center of the burner. The following sections compare the ignition delay and burn-rate results for droplet heights of 2 in. at a mean temperature of ~1650 K with the results at 5 in. at a mean temperature of ~1337 K.

4.4.1   Ignition Delay Trends

Ignition delay measurements for methanol, NM, and IPN, are shown in Figure 47,Figure 49 and Figure 50, respectively, at droplet heights of 2 and 5 in. As mentioned previously, because was taken as the time at which the flame shield (maintained at a height of 1 in. above the burner surface) reached the middle of the burner surface as it draw back, there may exists a small delay between when the flame shield is withdrawn and when the hot combustion gases come into contact with the droplets at the different heights. Additional diagnostics would be required to measure the temporal evolution of the temperature surrounding the droplet after the defined $t = 0\ s$. Results for all three fuels showed a significant increase in the ignition delay at the lower ambient temperature as expected. Lower ambient temperatures mean that there is less energy available for the initiation and sustainment of reactions that lead to ignition, causing longer ignition delays [7], [30]. In addition, as the ambient temperature decreases, kinetic effects start to become dominant due to their high sensitivity to temperature variation.

As discussed in section 4.3.1, ignition delay results at 2 in. with a mean temperature of ~1650 K for all three fuels showed that ignition delay was independent of initial droplet diameter. At 5 in. and a mean temperature of ~1337 K, a clear dependence on ignition delay with initial droplet diameter was observed for methanol as shown in Figure 47.
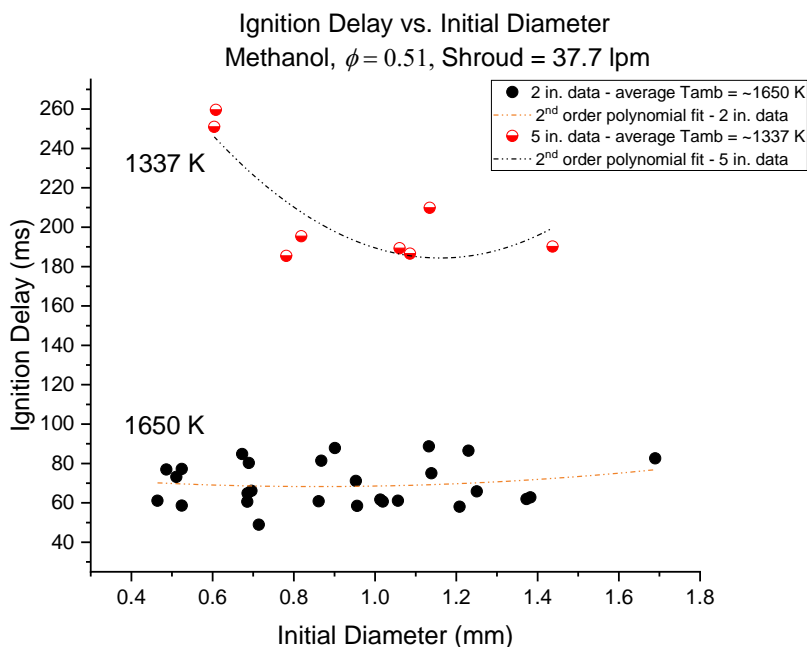
Figure 47. Temperature effects on the ignition delay of methanol droplets as a function of initial droplet size

At this temperature, the methanol data suggested the existence of a critical droplet size for minimum ignition delay within the range of droplet sizes studied. A similar trend was observed for n-heptane droplets by Nakanishi et al. [34] for droplet sizes between 0.8 mm and 1.4 mm igniting in ambient temperatures of 900 K and 950 K as shown in Figure 48. In the literature, the existence of this region has been attributed to an increase in the system Da number, which is proportional to the square of the instantaneous droplet diameter. An increase in Da number in this region indicates an increasing dominance of kinetic effects where the reaction time becomes longer than the diffusion time, thus increasing the ignition delay. Ignition delay for methanol droplet sizes between 0.4 mm and 1.4 mm at ~1337 K ambient temperature ranged between 180 ms and 260 ms, approximately up to three times the ignition delay values measured at an ambient temperature of

~1650 K. Studies on the effect of ambient temperature for different fuel droplets suggest that a change as small as 25 K may result in a significant change in the ignition delay time. In addition, the influence of ambient temperature is greater at lower temperatures.
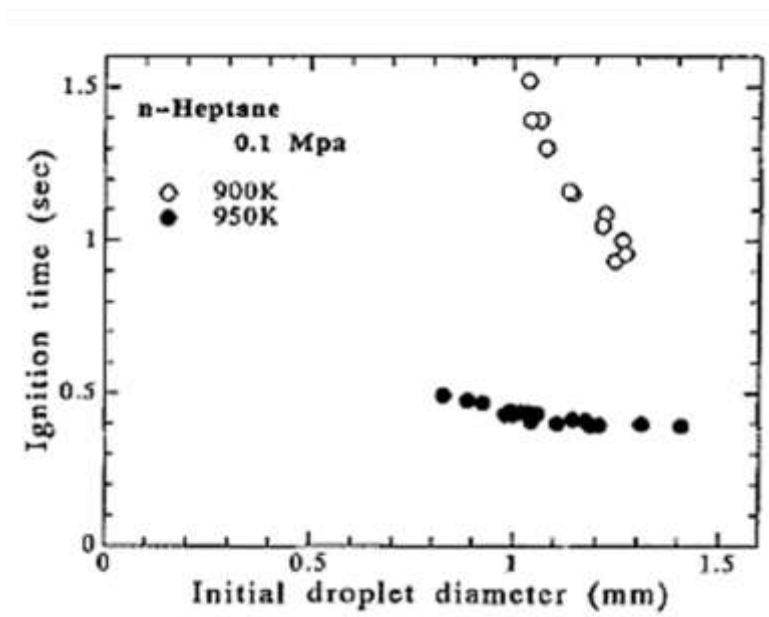
Figure 48. Ignition delay time for n-heptane droplets at 1 atm [34]

There is some scatter in the data for both NM and IPN at 5 in. above the burner, for an average ambient temperature of ~1337 K as shown in Figure 49 and Figure 50 respectively. As discussed previously, this could be due to the range of temperatures that could be experienced by the droplet in the 'quasi-steady' case. Despite the scatter, results at 5 in. for NM suggested a slight decrease in the ignition delay with increasing droplet diameter for the range studied. This trend could be due to kinetic effects, which have an increasing influence as ambient temperatures decrease, and are more dominant for fuels with relatively low boiling points, such as n-heptane. In comparison, no specific trend was observed for IPN droplets igniting in similar conditions. This suggests that for IPN, the ambient temperatures may still be too high to cause any variation in the droplet diameter. Other than ambient temperature, fuel volatility and droplets size, other parameters such as fuel molecular weight and reaction rates have an influence the ignition delay, and the combined influence of these parameters results in the variation in ignition delay with droplet size in different ambient conditions.

For the droplet size range tested at 5 in. (~1300 K), ignition delay results for nitromethane were found to range between ~140 ms and ~220 ms as shown in Figure 49. In similar conditions, IPN results were comparable to NM, reporting ignition delay values between ~140 ms and ~190 ms as shown in Figure 50. The monopropellant ignition delay results at the lower ambient temperature were slightly lower than those obtained for methanol.

Figure 49. Temperature effects on the ignition delay of NM droplets as a function of initial droplet size
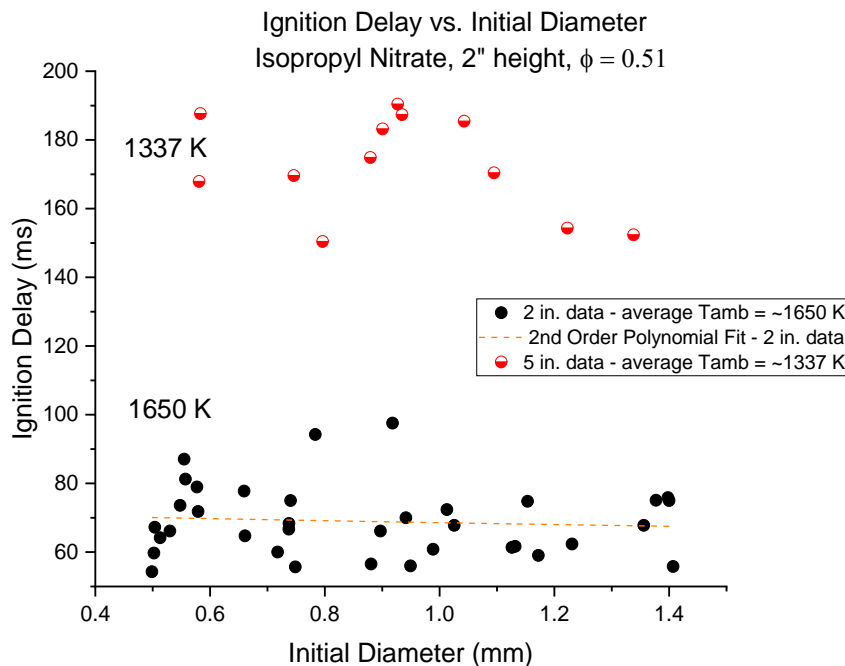
Figure 50. Temperature effects on the ignition delay of IPN droplets as a function of initial droplet size

4.4.2 Burning Rate Trends

Burning rate constants for droplet heights of 2 in. and 5 in. were obtained as a function of initial droplet diameter for all three fuels. For all three fuels, the data shows consistently lower burning rate constants at a droplet height of 5 in. with an average ambient temperature of 1337 K versus 2 in. with an average ambient temperature of ~1650 K, as expected. Higher temperatures increase the vaporization rate and reactivity of the fuels, resulting in faster burning rates compared to lower ambient temperature environments.

Methanol burning rates for at 2 in. (test series 2-5) and at 5 in. are shown in Figure 51. Test series 2-5 were selected because they had very good agreement with each other. Results and discussion including test series 1 can be found in section 4.3.2. Test series 2 − 5 at 2 in. above the burner were shown to have a moderate increase in burning rate constant, and in the literature, this trend is attributed to the influence of convection effects with increasing droplet diameter. Results at 5 in. above the burner, in an average temperature of 1337 K also showed some scatter. In addition, the data suggested a very slight increase in the burning rate constant, after which it remained somewhat

constant for droplet diameters beyond ~0.8 mm. The slight decrease in the methanol burning rate constant at 5 in. below ~0.8 mm also coincided with the increase in ignition delay in similar conditions as shown in Figure 47.
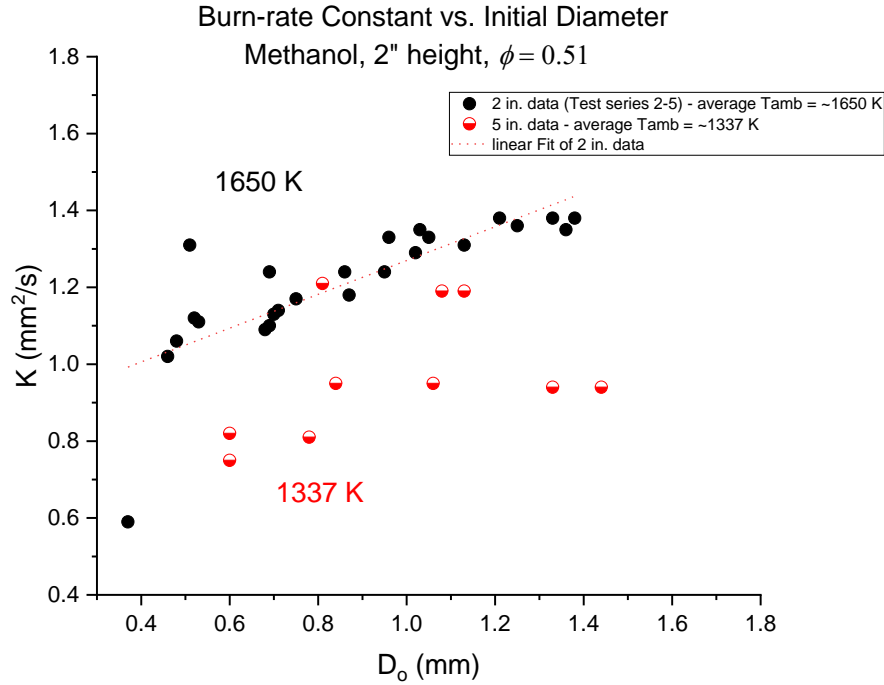
Figure 51. Temperature effects on the burn-rate constant of methanol droplets as a function of initial droplet size

A similar trend was observed by Awasthi et al. [87] for computed average burning rates constants of methanol with initial droplet diameter as shown in Figure 52. For a range of droplet diameters between 10 µm and 1 mm burning in 1200 K ambient temperature, results showed that the average burning rate constants increased until approximately 0.8 mm^2/s, and then either remained constant or slightly decrease. The authors described the initial increase to be as a result of the transition from kinetically controlled combustion (small Da) to diffusion-controlled combustion (large Da). When radiation effects were neglected, the constant average burning rate constant after $D_o = 200$ µm indicated that the diffusion-controlled combustion limit had been achieved.

At 5 in., methanol burning rate constants ranged between 0.7 mm^2/s and ~1.2 mm^2/s. These results were comparable to those obtained by Ambekar et al. [78]. For droplet sizes between 1 mm and 2 mm, Ambekar et al. obtained pure methanol burning rate constant values ranging between 0.7 mm^2/s and 1.2 mm^2/s. However, no ambient temperatures were reported for this study.
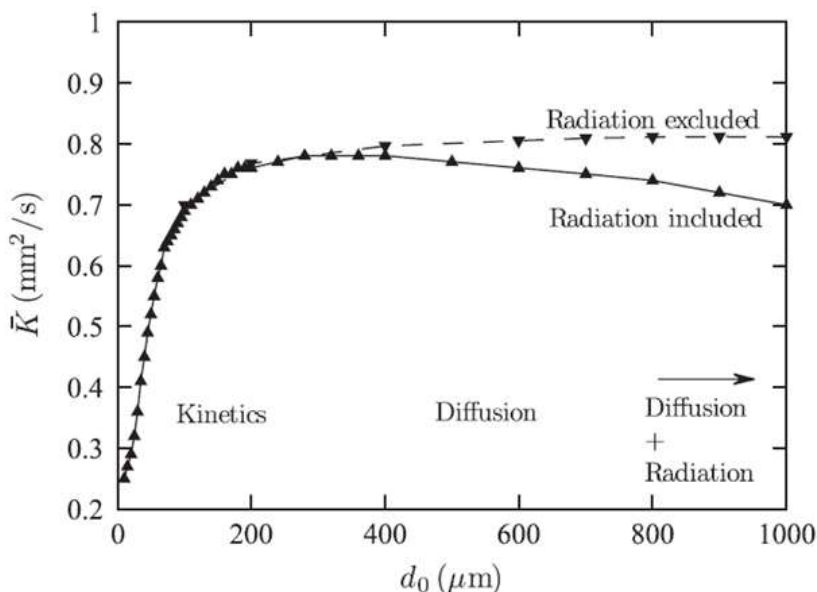
Figure 52. Computed average burning rate constants vs. initial droplet diameter, $T_{amb} = 1200$ K [87]

Burning rate results for NM at both 2 in. and 5 in. are shown in Figure 53. Burning rate constants for nitromethane were also found to be significantly lower at 5 in. (T_{amb} ~1337 K) as expected, however a somewhat slightly decreasing trend between burning rate constant could be observed for increasing initial droplet diameter. Burning rate constants across the range of initial droplet diameters were comparable to methanol, and ranged between ~0.9 mm^2/s and ~1.2 mm^2/s. The values are consistent with those measured by Ambekar et. al [78]. However, Ambekar et al. reported an increase in burning rate with initial droplet diameter, opposite to the trend found in the current work. The observed negative slope in the current results could be attributed to radiative heat losses. In the literature, decreasing burning rate constant values with increasing droplet diameter have been attributed to the effect of thermal radiation from the droplet flame. Saitoh et al. [88] noted that radiation heat losses have a significant influence on droplet combustion, reducing the maximum flame temperature of n-heptane droplets by more than 25%. Computational

results by Awasthi et al. [87] show a slow decrease in methanol burning rate constants after approximately 400 µm when radiation effects are included in the computational analysis. The authors also noted that since radiative heat losses are volumetric, the rate of decrease of the burning rate constant increases with increasing droplet diameter. As mentioned, since the spark-ignited NM droplets in the study by Ambekar et al. [78] did not exhibit this trend, a conclusive explanation for the burning rate behavior for NM at 5 in. could not be ascertained.

Results for burning rate constant versus initial droplet diameter for IPN are shown in Figure 54. IPN burning rate constants at 5 in. were found to be lower than those of 2 in. as expected. Similarly to the 2 in. height results, the burning rate constants at this height were found to be consistently higher than those of both NM and methanol. For the droplet size range between 0.6 mm and 1.4 mm, IPN burning rate constants reported ranged between ~0.8 mm^2/s and ~1.8 mm^2/s. In addition, burning rate constants were observed to increase with an increase in initial droplet size. These results were similar to Ambekar et al. [2] for droplet sizes ranging between 0.8 mm and 2 mm, where IPN burning rate constants were measured to be between ~0.5 mm^2/s and ~1.4 mm^2/s.

In general, a decrease in ambient temperature was found to decrease the burning rate values for all three fuels. There is more scatter in the 5 in. data compared to the 2 in. results which is attributed to the larger standard deviation (17%) of the ambient temperature from the average value (1337 K). Similarly to the 2 in. case, IPN droplets were shown to have the highest burning rate constant values for the range of droplet sizes studied, and maintained an increasing trend with increasing initial droplet diameters. An opposite trend was observed for NM burning rate constants at 5 in., which could be attributed to radiation heat losses from the flame, and this effect is larger for larger droplet sizes. Ignition delay and burning rate results suggest that in similar conditions, IPN droplets may ignite faster and burn faster compared to NM and methanol droplets.
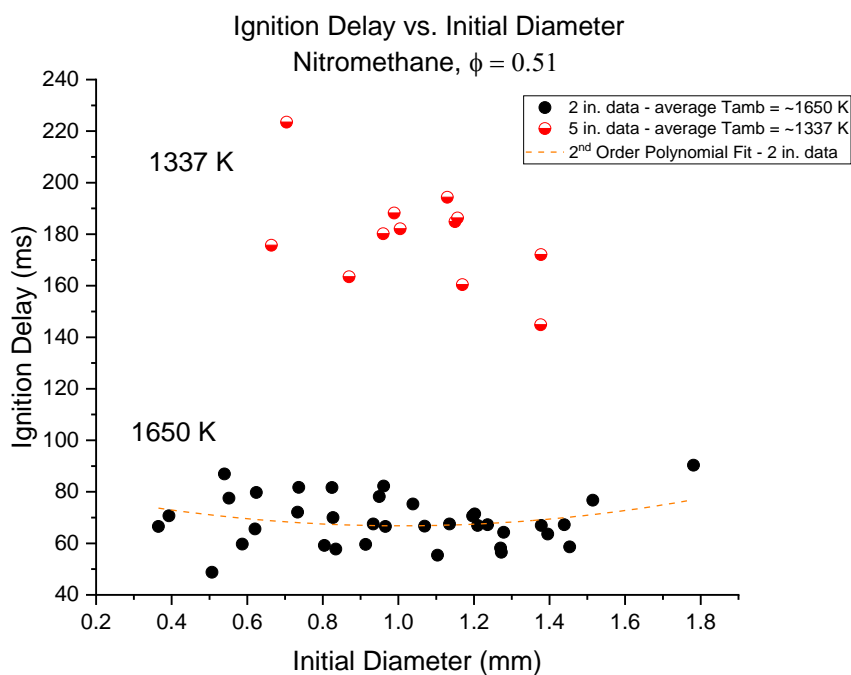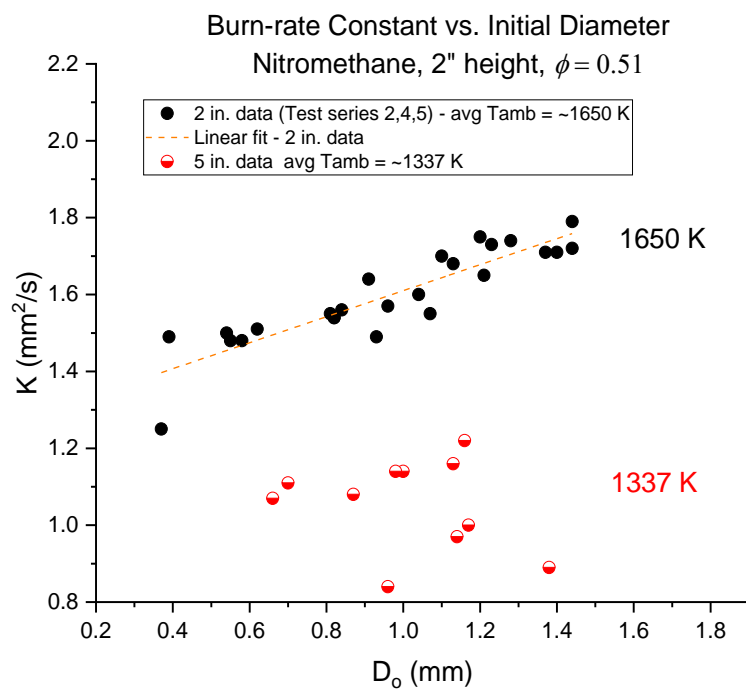
Figure 53. Temperature effects on the burn-rate constant of NM droplets as a function of initial droplet size
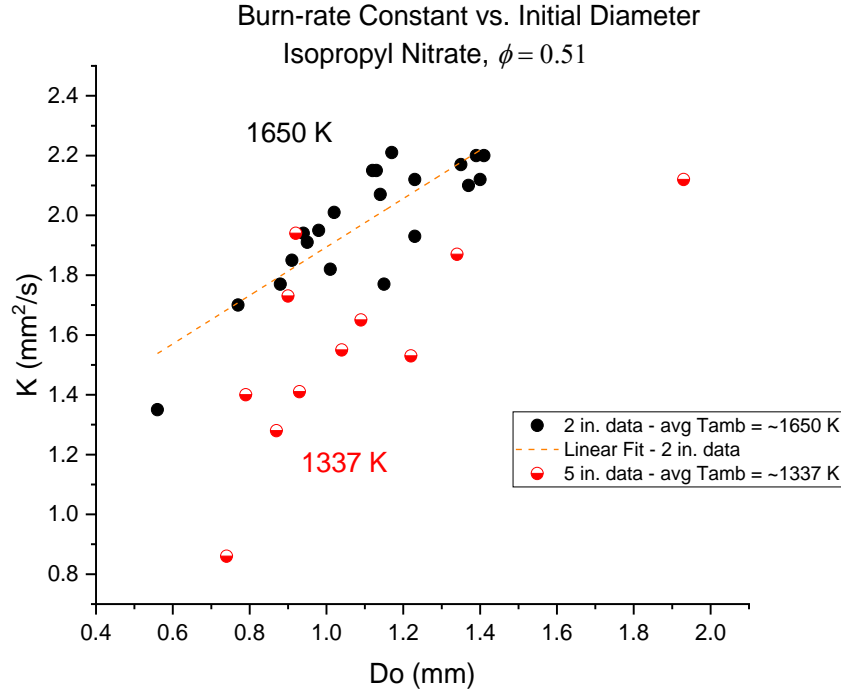
Figure 54. Temperature effects on the burn-rate constant of IPN droplets as a function of initial droplet size

4.5 Observed Droplet Behavior

Three different types of droplet behaviors were observed during the lifetimes of the droplets at both 2 in. and 5 in. heights, namely: puffing, stripping and deformation, which gave rise to micro-explosions. At 2 in. however, these behaviors were more aggressive in nature, and this could be because in addition to higher temperatures at 2 in., the droplets may also have experienced a slightly higher relative velocity at 2 in. compared to 5 in. height. In general, these behaviors typically occurred during the last ~50% of the droplet lifetimes.

4.5.1 Stripping and Droplet Deformation

High-speed flows such as those found in combustors give rise to secondary atomization of droplets in sprays, which occurs in the form of droplet deformation and breakup. In the literature, a nondimensional number known as the Weber number, We, which represents the ratio of the inertial force to the surface tension of a liquid drop, has been used characterize different droplet breakup regimes [89]. Weber number is given as:

$$We = \frac{D\rho(\Delta U)^2}{\sigma} \tag{15}$$

where D is the characteristic length represented by the initial droplet diameter, ΔU is the relative velocity between the droplet and the surrounding gas, ρ is the density and σ is the droplet surface tension. In general, droplet breakup can be divided into five regimes depending on the We number: vibrational $(We \leq 12)$, bag $(12 < We \leq 50)$, bag-and-stamen $(50 < We \leq 100)$, sheet stripping $(100 < We \leq 350)$, and catastrophic breakup $(We > 350)$. Significant deformation begins at a We number of 1, where aerodynamic forces have an effect on the droplet shape [80, 81]. A more detailed description of each breakup regime can be found in [89]. In the current study, droplet behavior most resembling vibrational and stripping breakup was observed.

In the literature, stripping has been described as 'mass removal from the surface of a droplet by aerodynamic shearing'[90]. Borisov et al. [91] described it as the ambient gas flow tearing liquid shrouds off of the liquid boundary layer of the droplet. The shrouds then rapidly transform into a fine cloud of droplets as they leave the droplet surface. Stripping in spray droplets is favorable because it produces fine atomization [91]. Droplet behavior believed to be stripping was observed for all three fuels and was characterized by small liquid fuel ligaments rapidly breaking off the surface of the droplet as it continued to burn. Figure 55 typifies the stripping behavior observed for an IPN droplet. Though a small amount of mass was ejected from the droplet during stripping, a change in the burning rate of the droplets was not evident as indicated by a constant slope of the square of the diameter vs. time. In addition, no indication of the ligaments burning as they broke off the droplet was evident from the OH videos. This behavior became more aggressive as the droplets decreased in size and began to deform. It was observed that out of all the behaviors, stripping occurred first and appeared to persist for the remainder of the droplet lifetime.
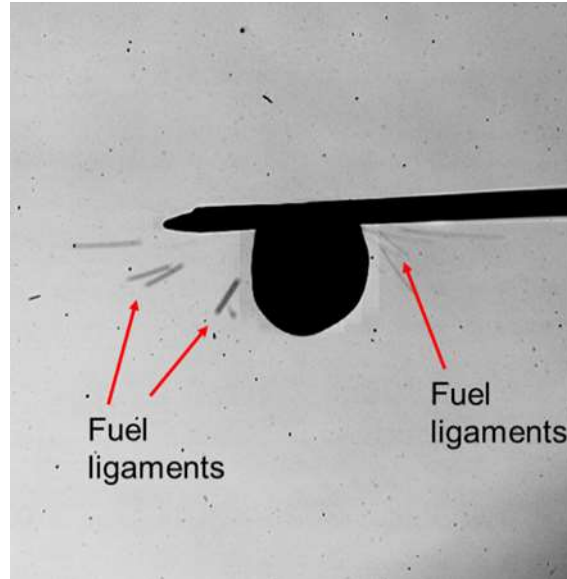
Figure 55. Stripping behavior of a burning IPN droplet suspended on a 125 µm silica fiber

Another type of droplet behavior similar to vibrational breakup was observed primarily for relatively large NM and IPN droplets ($D > \sim 800$ µm) and was observed to be more severe for IPN. In the literature, vibrational breakup is observed for relatively small We number ($We \leq 12$), and occurs when oscillations in the flow field occur at the natural frequency of the drop [89], causing the eventual decomposition of the droplet into a few large fragments. In the current study however, this behavior did not result in the actual secondary breakup of the droplets, but rather for some of the IPN droplets, it resulted in the droplets detaching from the silica fiber. Figure 56 shows an IPN droplet with an initial droplet diameter of 1.23 mm suspended on a 125 µm silica fiber, undergoing severe droplet deformation and finally detaching from the supporting silica fiber.
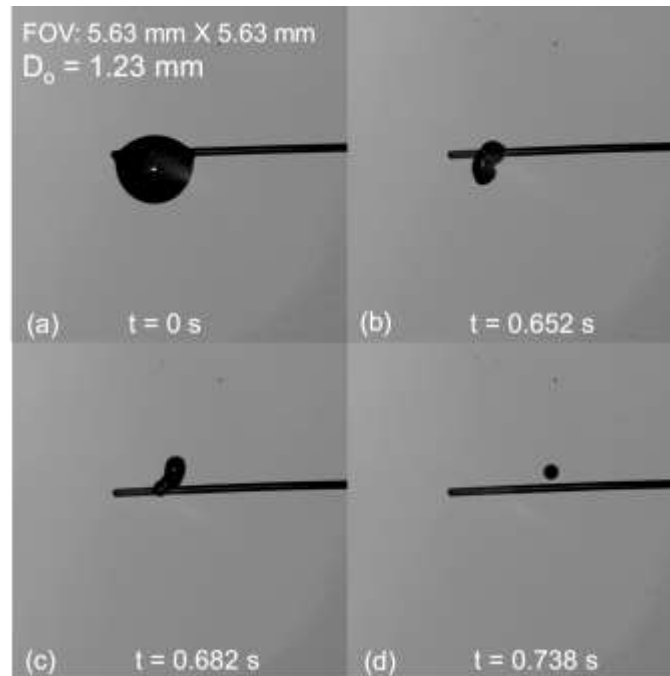
Figure 56. Sequence of IPN droplet showing (a) droplet at ignition; (b)-(c) droplet deformation during burning; (d) detachment of the burning droplet from the silica fiber

A simple theoretical analysis of the range of We numbers for the droplet sizes and liquid fuels in this study is shown in Figure 57 for a convective velocity of ~94 cm/s calculated from a momentum conservation across the flat flame for the McKenna burner post-combustion gases. The calculation shows that based on the theory, the dominant modes of droplet breakup are the bag-and-stamen breakup ($50 < We \leq 100$), as well as stripping break up ($100 < We \leq 350$) which was evident from video data across all fuels. Though the gas velocities may be significantly underpredicted in these preliminary calculations, the calculations suggest that in general, IPN droplets have larger We numbers than NM and methanol, which may explain the severity of the vibrational deformation observed for IPN. For reference, the Reynolds number for the post-combustion gases, calculated from the density and viscosity of the post-combustion gases was found to be approximately 300, suggesting a laminar flow. In addition, Nusselt number (representing the ratio between convective to conductive heat transfer) for the droplets ranged between 2 and 3, representative of laminar flow.
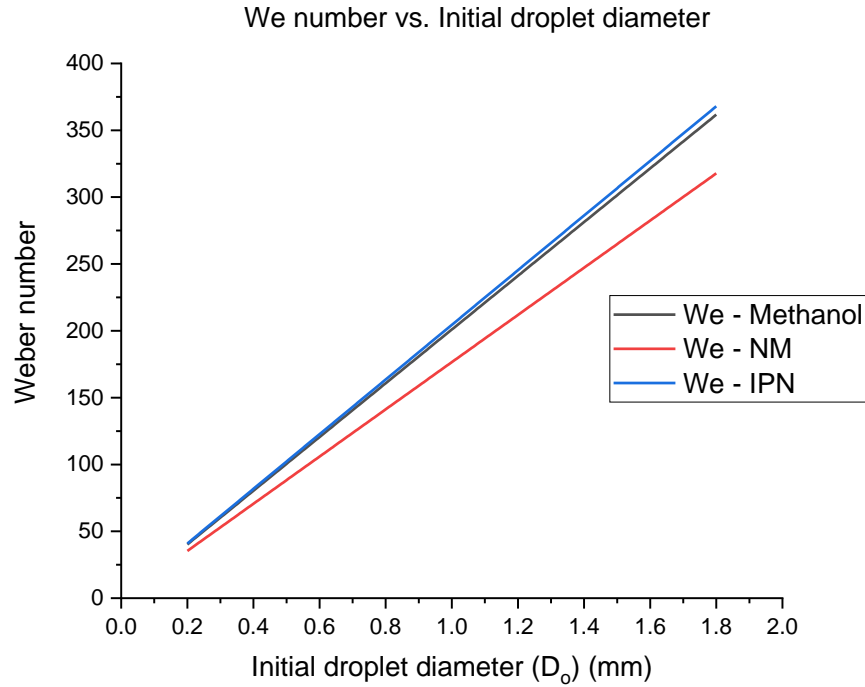
Figure 57. Analysis of We numbers for Methanol, IPN and NM droplets between 0.2 mm and 1.8 mm

4.5.2 Puffing

In the literature, puffing is defined as the 'rapid expansion of vapor inside a droplet', which may result in either a total or partial disintegration of a droplet [92]. Puffing behavior was observed for some methanol droplets and only for a few of the monopropellant (NM and IPN) droplets towards the end of their droplet lifetimes. This behavior was characterized by a series of bubble formation and disruption events on the surface of the droplet. With each of these events, a small mass of the liquid appeared to be ejected from the droplet.

In the literature, this behavior has been observed for both multicomponent miscible and emulsion fuels [80–84]. In multicomponent and emulsion fuels, there exists two or more liquids with largely different volatilities present in the same droplet. As the droplet is exposed to a hot environment and gasification begins, the lower boiling point liquid (high volatility fuel) present on the surface of the droplet evaporates quickly, and leaves the higher boiling point fuel at the droplet surface. However, there is still the presence of the higher volatility fuel within the droplet. As the droplet continues heat up, the surface of the droplet consisting of the lower volatility fuel, may heat up

beyond the boiling point of the higher volatility fuel, causing it to superheat. The superheating of the higher volatility fuel trapped in the interior of the droplet causes it to vaporize inside the droplet, leading to internal pressure build-up within the droplet, observed as puffing as shown in Figure 58.

For methanol droplets, one of the major combustion products is water, which is completely soluble in methanol. The hygroscopic nature of methanol causes it to absorption water either from the environment or generated at the flame [97], resulting in boiling and bubbling as a result of the volatility differences between water and methanol. The propensity of NM or IPN to absorb water is much lower compared to methanol, which could explain this behavior being observed almost exclusively for methanol droplets.

Figure 58 shows a typical series of bubble formation and disruption on the surface of a methanol droplet with an initial diameter of 1.03 mm. In this case, the bubble growth led to partial fragmentation of the droplet as the pressure was released through the surface of the droplet, leaving a smaller mass of fuel to continue burning. In other instances, puffing and disruption in methanol droplets has been known to cause flame extinction [97]. This did not happen in the current study at 2 in. above the burner, possibly due to the high ambient temperatures that sustained a flame throughout the droplet lifetime.
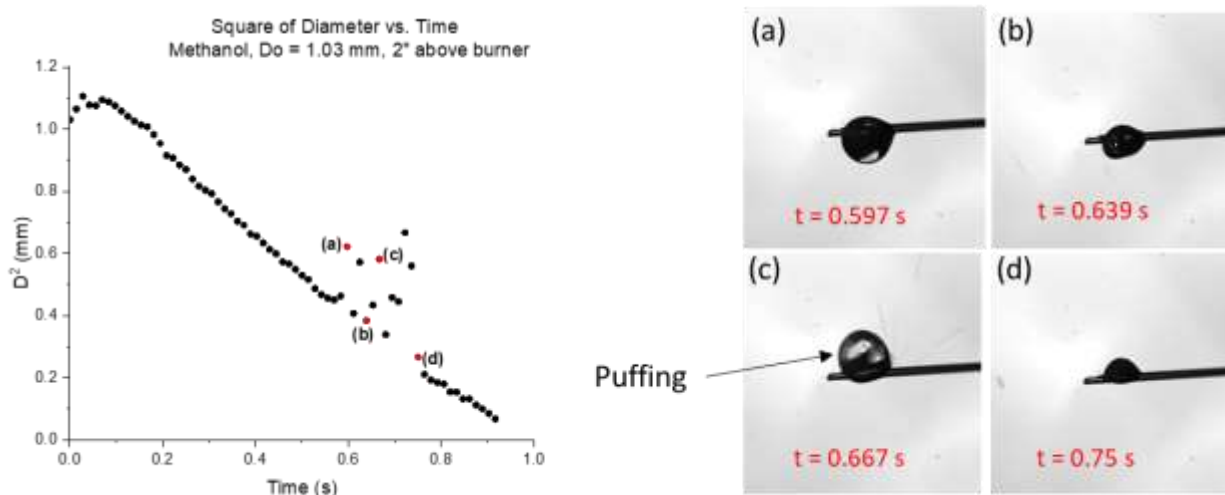
Figure 58. Series of bubble formation (puffing) and disruption during combustion of a methanol droplet, D_o = 1.03 mm (FOV: 3.5 mm X 3.5 mm)

4.5.3 Micro-explosions

In the literature, micro-explosive behavior has been defined simply as the sudden and violent disruption of a droplet into much smaller multiple droplets or fragments [92]. This behavior has again been observed for multicomponent and emulsion fuel droplets. For these droplets, micro-explosions occur following the puffing of a droplet due to the expansion of high volatile fuel components, and rather than partial disruption of the droplet, micro-explosions result in complete and catastrophic fragmentation of the droplet [95], occurring in the order of microseconds. Micro-explosions in liquid fuel droplets are favorable as they enhance secondary atomization by breaking the droplet up into smaller fragments. In fuel sprays, this behavior is beneficial because it allows for further penetration of droplets into combustors (favored by initially large droplets), as well as better vaporization and mixing (favored by smaller droplets obtained after micro-explosions of initially large droplets) [94]. As a result, studies focusing on the control of the micro-explosion of multi-component and emulsion fuel droplets have become important.

In the current study, micro-explosions were observed for some droplets for all three fuels and in general, the micro-explosive behavior appeared to result from a combination of deformation, puffing and aggressive stripping. This behavior typically occurred towards the end of the droplet lifetimes, and occurred in a series of rapid micro-explosion events, corroborated by a series of sudden changes in the OH signal intensity. At the end of this series of micro-explosion events, the droplet was either too small to sustain a flame or completely disappeared. An analysis of simultaneous shadow and OH* videos showed that the micro-explosions observed in the OH* signals occurred during aggressive sputtering and deformation behavior of the droplets. For methanol, some droplets were also observed to explode at very end of their droplet lifetime. Typical micro-explosion behavior is shown in Figure 59. At t = 1.0108 s, the OH* signal is weaker than it was at a larger droplet size. This could be because at this small size, there is less available fuel vapor surrounding the droplet, and therefore reaction may be less intense. At t = 1.011 s, a micro-explosion of the droplet occurs as corroborated by a sudden increase in the intensity of the OH* signal, which then proceeds to reduce in intensity until the next micro-explosion event where the OH* signal significantly increases again. Corresponding shadow images of the droplet show the droplet undergoing deformation and stripping.
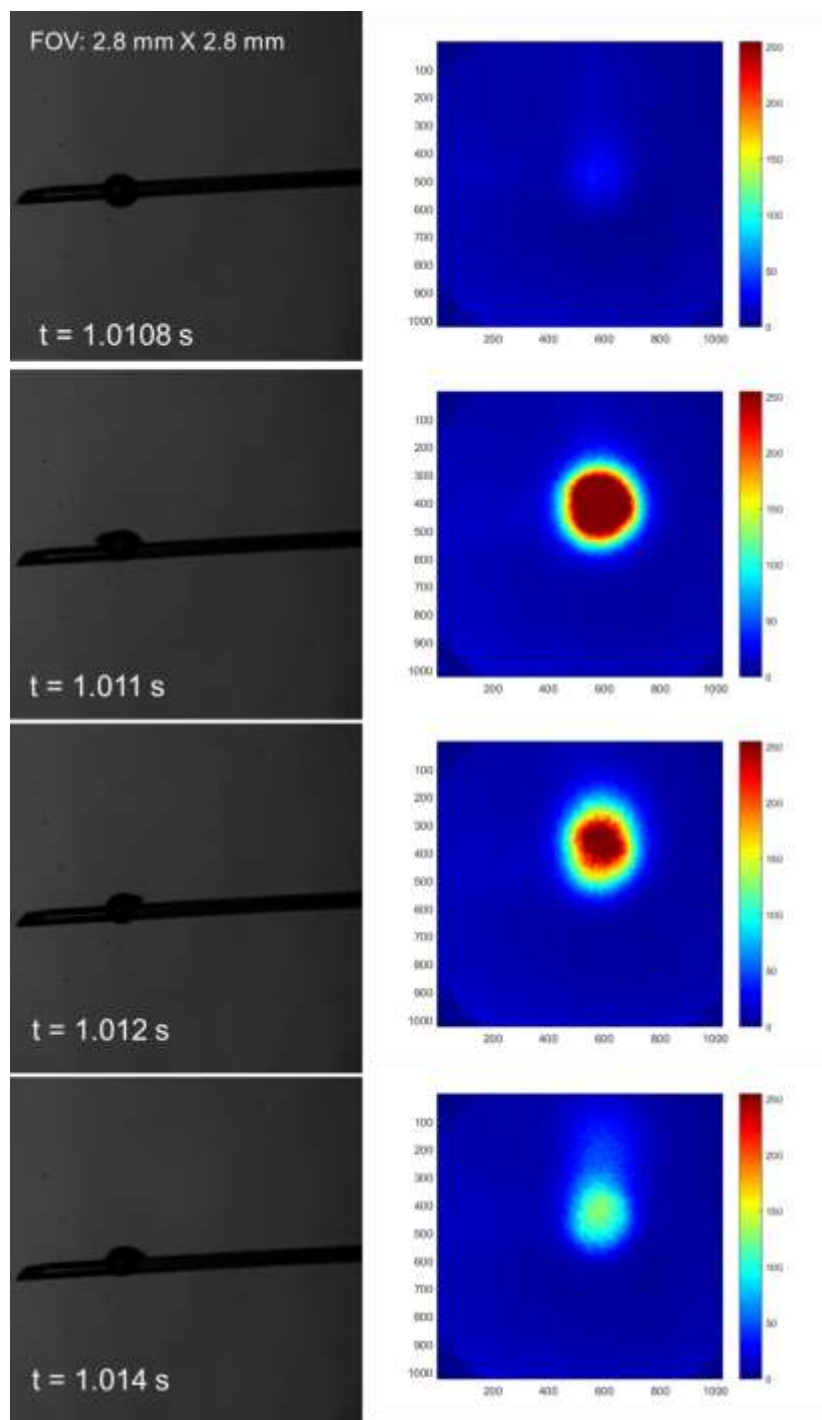
Figure 59. Example sequence of a micro-explosion event of a pure NM droplet towards the end of its droplet lifetime showing shadow images and corresponding OH signal images

An analysis of simultaneous OH* signal and shadow videos was performed to extract the droplet diameter at the onset of microexplosions for each of the three fuels shown in Figure 60 (a). There is significant scatter in the data, however for all three fuels, the majority of the microexplosions occurred for droplet diameters below ~500 µm. $D_{mexp} = 0$ represents droplets that only exploded at the end of their droplet lifetime. In addition, results showed no variation of D_{mexp} with initial droplet diameter or fuel. Figure 60(b) shows the percentage of droplet lifetime that had elapsed at the time microexplosions began for a range of droplet sizes for each of the three fuels. Though results show no variation with either initial droplet size or fuel, the majority of the micro-explosion behavior was observed after ~80% of the droplet lifetime had elapsed. For some droplets, methanol exhibited earlier onset of micro-explosions due to the puffing and disruption behavior described in Section 4.5.2.
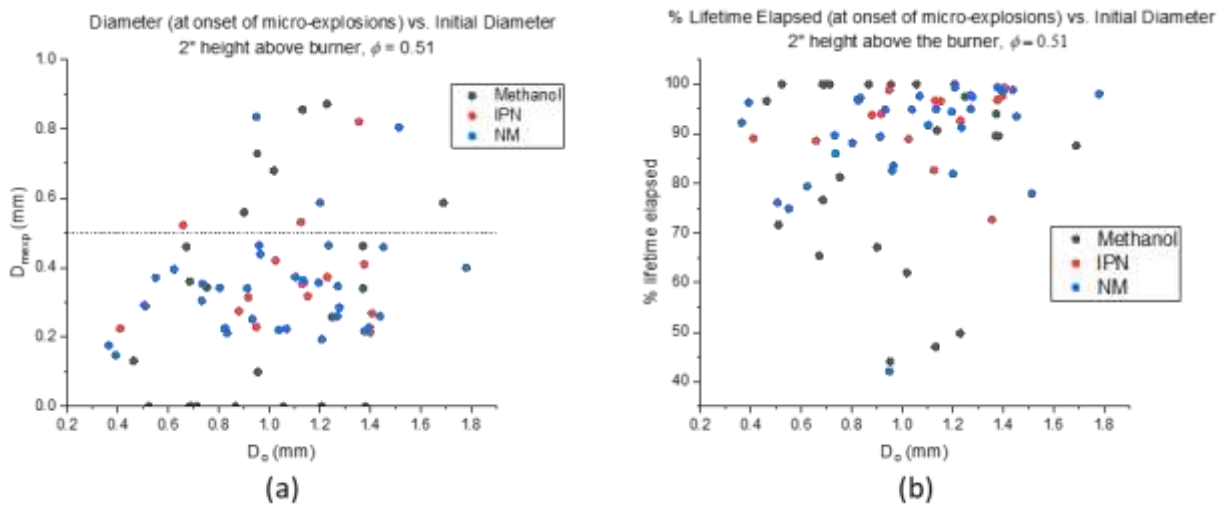
Figure 60. (a) Diameter at onset of micro-explosions (b) Percentage of droplet lifetime elapsed at onset of micro-explosions

4.6 Effect of Flow Unsteadiness

As shown in Table 4, CARS temperature measurements at 5 in. and 8 in. heights with a shroud flow rate of 5.6 lpm exhibited 'unsteady' behavior. Figure 61 shows that for the unsteady conditions, droplets reacting in these flows may have experienced a wide range of temperatures during their lifetime, ranging between room temperature and ~1500 K and ~1000 K for the 5 in. and 8 in. cases, respectively.
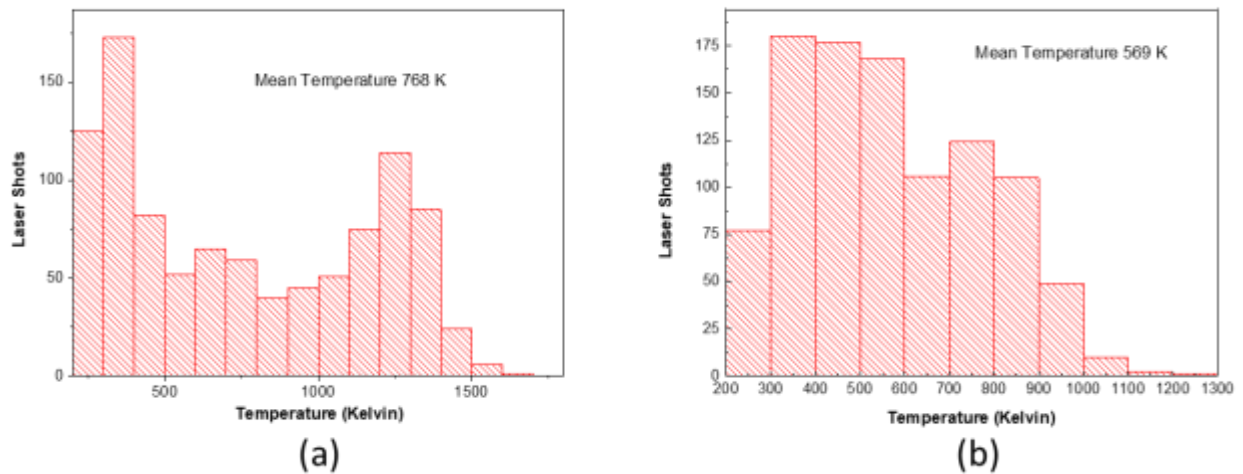
Figure 61. Histogram of CARS temperature measurements for a shroud flow rate of 5.6 lpm (a) 5 in. above the burner; (b) 8 in. above the burner

In the current work, a very preliminary study of the effect of flow unsteadiness on droplet burning was performed. For all three fuels, droplets reacting in unsteady flow exhibited cycles of ignition and extinction, likely due to the temperature oscillations of the surrounding flow. The ignition and extinction cycles observed can be explained by the competition between heat generation from reaction and heat loss from diffusion and convection. A high ambient temperature environment surrounding the droplet favors the progression of the reaction between fuel vapor and ambient oxidizer. When heat generation from the reactions is greater than heat loss through diffusion and convection of heat away from the reaction zone, a flame is sustained. When the rate of heat loss exceeds the rate of heat generation at the reaction zone, either due to a reduction in ambient temperature and/or high convective velocities surrounding the droplet, the flame is extinguished.

The ignition and extinction cycles are evident in the square diameter histories of the burning droplets. An example case is given in Figure 62, which shows the square diameter history of a nitromethane droplet (initial diameter 1.58 mm) positioned at 5 in. above the burner experiencing ignition and extinction cycles as it decreases in size. In general, these cycles were largely a result of unsteadiness in the surrounding flow and not on any characteristics of a particular fuel.
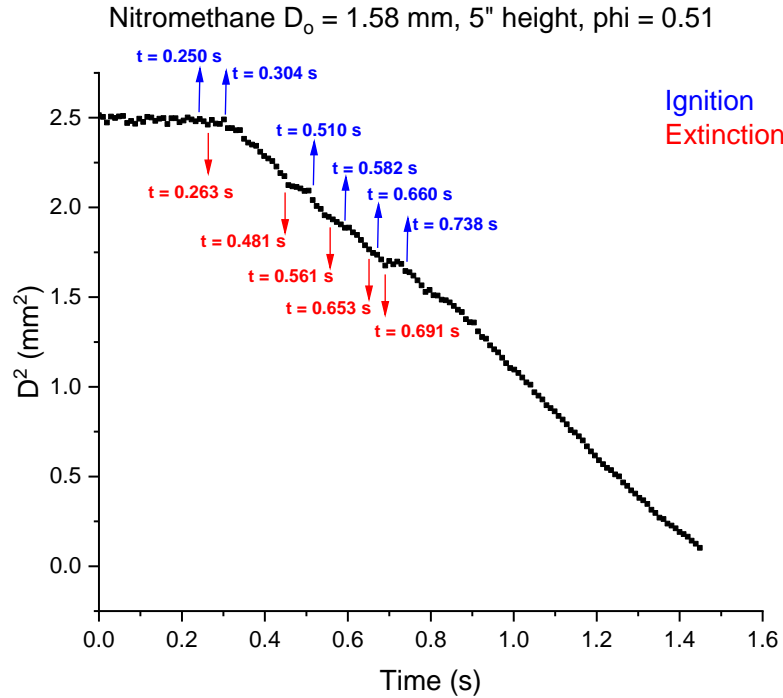
Figure 62. Square diameter history of a nitromethane droplet showing instances of ignition and extinction during droplet lifetime

It was also observed that flow unsteadiness can have a significant effect on the burn rate of droplets of comparable sizes. An example is shown in Figure 63, which compares two methanol droplets of similar initial diameter reacting in a 'quasi-steady' flow and an 'unsteady' flow at 5 in. above the burner surface. At ignition, the two droplets ignite and burn at the same rate, however the droplet in the unsteady flow experienced flame extinction early in the droplet lifetime, and proceeds to evaporate until the end of its droplet lifetime. These observations suggest that droplets in the dilute regions of a spray experiencing turbulent flows may undergo oscillations of ignition and extinction or early droplet extinction, which may significantly affect the burning rate and contribute to overall unsteadiness of the combustion.
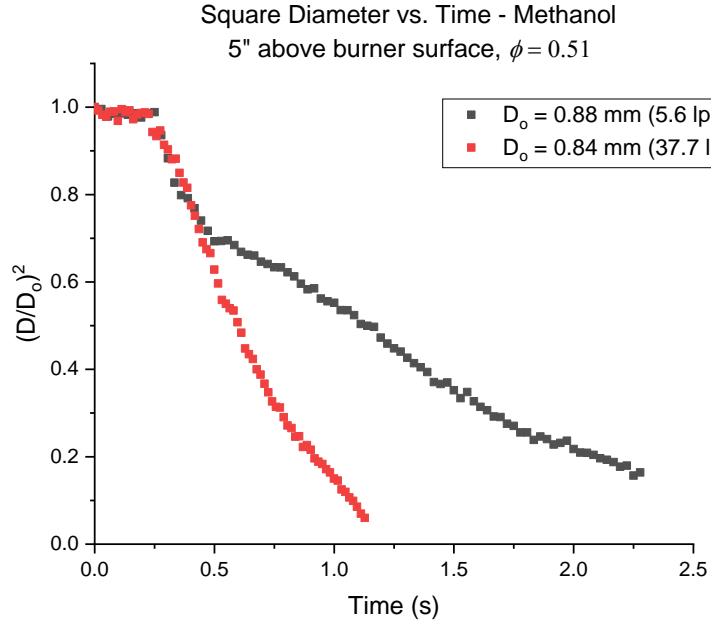
Figure 63. Comparison of a methanol droplet reacting in unsteady and quasi-steady flow at 5 in. above the burner surface

4.7 Theoretical Mass Burning Rate Comparison

The experimental mass burning rates measured in this work were compared to theoretical predictions of the hybrid combustion model, formulated by Allison and Faeth [55], as well as the classical quasi-steady model, or the D^2 law. The experimental burning rate constants for the steady case (2 in. above the burner) were converted to mass burning rates (g/s) using Equation 16 for comparison with theoretical predictions:

$$\dot{M} = K\pi\rho_l r_l/2 \tag{16}$$

Properties of the ambient conditions used in both models were obtained from the NASA Chemical Equilibrium with Applications (CEA) code, and can be found in Appendix B. Thermophysical properties used in the D^2 Law are listed on Table 7.

Table 7. Thermophysical properties used in the D^2 Law model

Property	Methanol	IPN	NM
k_F [W/m-K]	0.0141	0.0592	0.1195
ν	6.4	4.25	1.69
C_{pg} [J/kg-K]	1549	2349	1920
h_{fg}[J/mol]	38.28e3	38.79e3	33.99e3
Δh_c[J/mol]	-725e3	1950.9e3	709.19e3

Methanol, IPN and NM experimental mass burning rates were compared to the D^2 Law model. Convection effects were included using film theory. The introduction of convection effects both from buoyancy and a relative velocity between the droplet and the free stream has the effect of enhancing droplet burning rates. Stronger convection produces steeper temperature and species concentration gradients, resulting in accelerated chemical kinetics [98]. The mass burning rates with convection effects were calculated using Equation 17 as given by Turns [10].

$$\dot{m}_F = \frac{2\pi k_g r_s Nu}{C_{pg}}\ln(1 + B_{o,q}) \tag{17}$$

where the correlation for Nu is given by:

$$Nu = 2 + \frac{0.555 Re^{1/2} Pr^{1/3}}{\left[1 + \frac{1.232}{RePr^{\frac{4}{3}}}\right]^{1/2}} \tag{18}$$

The gas phase thermal conductivity, k_g, was approximated using Equation 18, where k_F is the fuel thermal conductivity and k_∞ is the thermal conductivity of the post combustion gases obtained from NASA CEA. The gas phase specific heat capacity at constant pressure, C_{pg}, was estimated as the fuel vapor heat capacity at the fuel boiling point.

$$k_g = 0.4 k_F(T_{boil}) + 0.6 k_\infty \tag{19}$$

Additional properties used in the Hybrid Combustion Model for IPN and NM are listed in Table 8. For an assumed activation energy of 0 kcal/mole as recommended by Allison [1], the pre-exponential factor, A, was selected to best fit the experimental data using a root mean square error minimization [55]. The rms error values presented here are normalized using the mean of the data and reported as a percentage of the mean.

Table 8. Thermophysical properties used in the Hybrid Combustion Model

Property	IPN	NM
[cal/gK]	0.528	0.5
[cal/gK]	0.355	0.355
[cal/gK]	0.7043	0.425
[cal/cm-s-K]	1.414e-4	3.29e-5
[cal/cm-s-K]	4.86e-4	4.33e-4
[cal/cm-s-K]	3.27e-4	3.27e-4
[cal/g]	349	-167
[cal/g]	-1610	-7093
[g/cm^2-s]	0.86	0.0420 (test series 2,4,5) 0.1020 (test series 1,3)
[kcal/mole]	37	50

Similarly to Allison, values of C_P were obtained from the specific heats of the products of the stoichiometric reaction of the monopropellant fuels with oxygen, while values for C_{FP} were obtained from those of the decomposition reactions of the monopropellant fuels. C_O was estimated to be the specific heat at constant pressure of the post-combustion gases obtained from NASA CEA. The thermal conductivity of the gases in region A (Figure 22), λ_{Al}, was estimated as the fuel vapor conductivity. The thermal conductivity for region B (Figure 22), was obtained from the thermal conductivities of fuel decomposition products, while that of region C (Figure 22), was estimated to be the thermal conductivity of the ambient gases obtained from NASA CEA. The decomposition products used for nitromethane [99] and isopropyl nitrate [79] for the computation of the aforementioned thermophysical properties are shown in Equation 20 and Equation 21, respectively. A more detailed formulation of the hybrid combustion model can be found in [55] and [1].

$$CH_3NO_2 \rightarrow 0.6NO + 0.6H_2O + 0.4CO_2 + 0.3C_2H_6 + 0.2N_2 \tag{20}$$

$$C_3H_7NO_3 \rightarrow 0.25CH_3CHO + 0.5CH_3NO_2 + 0.5NO + 0.25CH_3OH + 0.25H_2CO + 0.75CO + 0.75CH_4$$

(21)
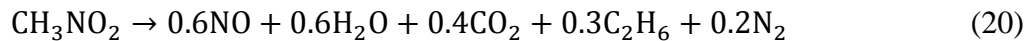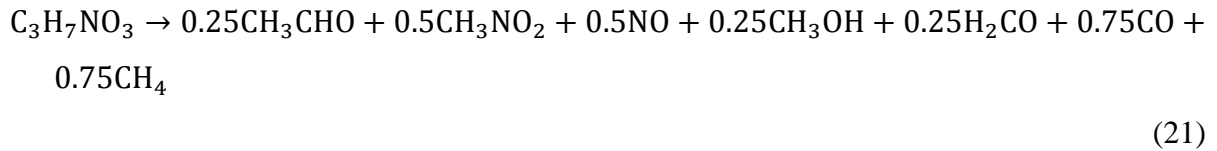
Methanol experimental mass burning rates at 2 in. above the burner (T_{avg} ~1650 K) were compared with D^2 Law theoretical mass burning rates as shown in Figure 64. For methanol, the D^2 Law was found to overpredict the experimental data. The inclusion of convection effects again significantly overpredicted the experimental data. Other than the simplicity of the D^2 Law model, one possible explanation for the deviation of the experimental data from the theory, is the effect of water absorption of methanol. Law [19] noted that water vapor from the environment and from the methanol droplet flame could condense and dissolve into the methanol droplet, and contribute to either the increased or decreased gasification rate of the droplets depending on the amount of water absorption. In an experimental investigation into the vaporization and combustion of methanol and ethanol droplets, Lee and Law [97] suggested that the initial effect of water absorption is to augment the gasification rate using the heat release from the condensation of water vapor on the surface of the droplet. However, as the water content increases, the overall volatility of the droplet decreases, leading to a reduced droplet gasification rate.
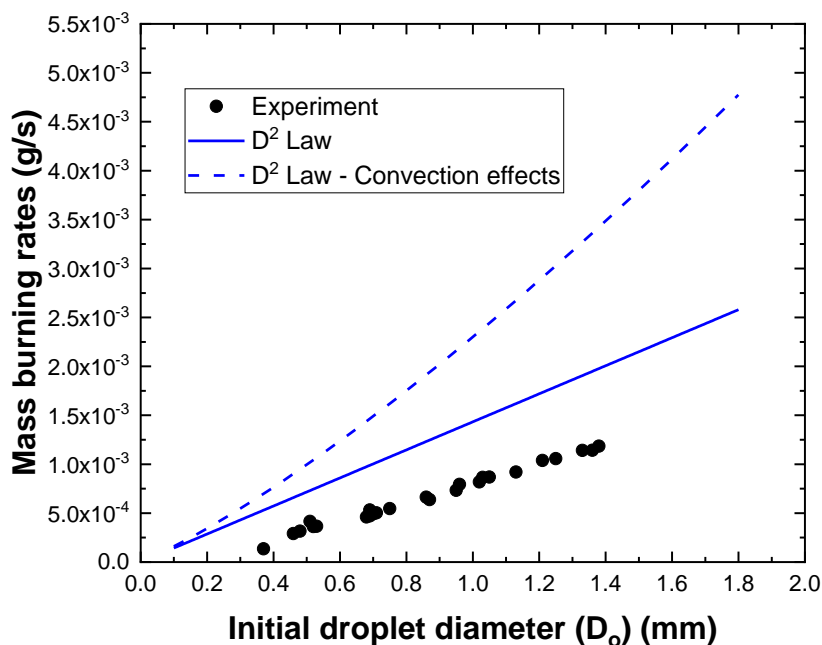
Figure 64. Experimental and theoretical mass burning rates for methanol

Experimental mass burning rates for NM and IPN for the steady conditions were compared to both the D^2 Law models and the Hybrid Combustion Model. Mass burning rate results for NM are presented in Figure 65. Test series 2, 4 and 5 were compared separately from test series 1 and 3 with theoretical predictions, as the test series in these two groups were in very good agreement with each other. For comparison with the hypergolic fuels MMH, UDMH and hydrazine burning in the post combustion gases of a flat flame burner, Allison [55] assumed an activation energy of 0 kcal/mole. However, for the fuels used in this study, the activation energies of the decomposition reactions were used for the model. In the literature, the majority of experimental studies on NM decomposition have reported activation energies between 50 kcal/mole and 53 kcal/mole [100]. Therefore, in this study, an activation energy of 50 kcal/mole was used for comparison with the NM experimental data. Being a semi-empirical model, the hybrid combustion model fit the NM experimental data well. For the selected activation energy value (50 kcal/mole), a pre-exponential factor of 0.042 g/cm^2-s was found to best fit the experimental mass burning rate data for test series 2, 4, and 5, with an rms error value of ~6.9%. A second fit was done on test series 1 and 3, and a

pre-exponential factor of 0.1020 g/cm^2-s was found to best fit the test series 1-3 data with an rms error value ~7.4%.

Similarly to methanol, the D^2 law was found to be in good agreement with NM mass burning rate results for test series 2, 4 and 5 at relatively smaller droplet sizes, but predicted slightly lower burning rates for the larger droplet sizes, reporting an rms error value of ~18.4%. The addition of convection effects significantly improved the mass burning rate predictions of the D^2 Law, and was in good agreement with the experimental data for the entirety of the range of droplet sizes for test series 2, 4 and 5, reporting an rms error value of ~7.4%. In general, the D^2 law predicted mass burning rates of NM reasonably well considering the simplified approach of the model and its limitation to bipropellant fuels with single diffusion flames.

Results for IPN are shown in Figure 66. While the D^2 Law again underpredicts the mass burning rates for the relatively larger droplet sizes (rms error value ~25.4%), the inclusion of convection effects increases the predicted mass burning rates, which are in better agreement with the experimental data, reporting an rms error value of ~11.7%. However, even with convection effects, the D^2 Law slightly underpredicts mass burning rates for the larger droplets in the range studied. The Hybrid combustion model however, best predicts the experimental data for IPN. Experimental studies have reported a range of activation energies ranging from 26 kcal/mole to 43 kcal/mole, however for consistency with IPN droplet work, the activation energy used by Ambekar et al. [2] in their study on IPN droplet combustion (obtained by Krause et al. [101]) of 37 kcal/mole was chosen for use in this model. Using this value for activation energy, a pre-exponential factor of 0.86 g/cm^2-s (with an rms error of ~1.3%) was found to best fit the experimental data.

In general, the theoretical comparisons in Figure 65. Experimental and theoretical mass burning rates for nitromethane and Figure 66 for NM and IPN, respectively, show that in high temperature environments, the bipropellant model (D^2 Law) and the hybrid combustion model merge. A similar observation was made by Allison et al. [55] in comparisons of MMH and hydrazine with the hybrid combustion model. This observation suggests that for monopropellants burning in high temperature oxidizing atmospheres, the effect of the presence of a double-flame structure to augment the droplet mass burning rate decreases as droplet size decreases. The majority of the

experimental mass burning rate results for MMH are for droplet diameters above 0.6 cm, however theoretical predictions from the hybrid combustion model suggest that mass burning rates for droplet diameters between 1 mm and 2 mm were comparable to those obtained in this study for NM and IPN. Predicted MMH droplet mass burning rates for 1-2 mm diameter droplets reacting in a calculated ambient temperature of 2530 K, ranged between ~0.001 g/s and 0.004 g/s.
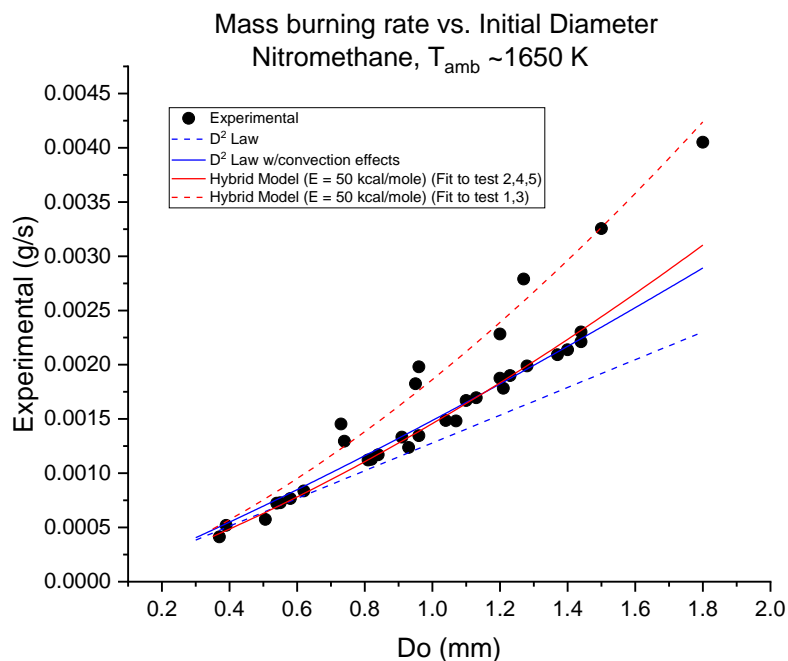
Figure 65. Experimental and theoretical mass burning rates for nitromethane
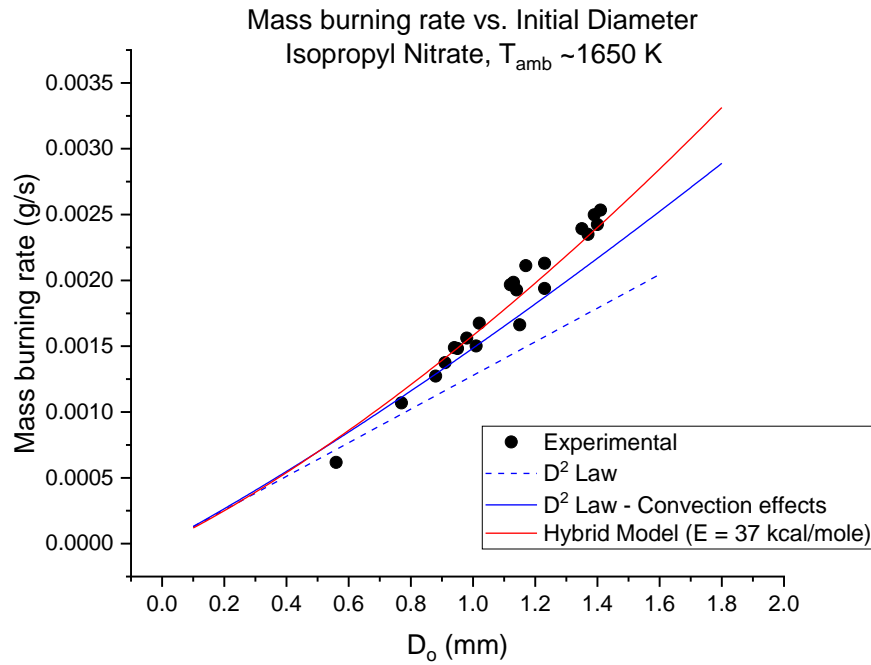
Figure 66. Experimental and theoretical mass burning rates for isopropyl nitrate

4.8 Thermal Droplet Ignition Model Comparison

As mentioned in Section 2.6, due to its relative simplicity and applicability, Law's quasi-steady droplet ignition analysis, with modifications from Aggarwal [14], was used to make theoretical comparisons with experimental ignition delay data obtained in this work. A more detailed fundamental description of the theory and the manner in which it is applied is presented in Appendices A and D. Specifics of the formulation can be found in References [14], [56] and [14].

In summary, the droplet size and droplet temperature are traced in time using the rapid mixing model, which assumes that the droplet temperature is spatially uniform but varies temporally. The modified system Da number (Δ) (also varying in time for a particular initial droplet diameter), is then calculated using Equation 22. The ignition Da number (Δ_I) is computed analytically using Aggarwal's [14] correlation in Equation 23. Ignition is then predicted to occur when $\Delta = \Delta_I$.

$$\Delta = \left\{ \frac{B'(W'_f)^{(1-a_f)}}{\lambda'_\infty / C'_{p\infty}(W'_O)^{a_O}} \left(\frac{p'C'_p}{R'_u Q'}\right)^{a_O+a_f} \right\} \times \left\{ \frac{(Y_{O\infty})^{a_O}\exp(-T'_a/T'_\infty)(M'r'_s)^2}{\left(\frac{C'_p T'_\infty}{Q'}\right)^{a_O+a_f}\left(\frac{C'_p T'^2_\infty}{T'_a Q'}\right)^{3-a_f}} \right\} \tag{22}$$

$$\Delta_I = 0.9865\exp(6.463\beta + 0.35) \qquad \text{for } \beta \leq 0.30 \tag{23}$$

Figure 67 shows an example of the evolution of both the modified system and ignition Da numbers with time. The intersection of the two curves denotes the point of ignition of the droplet. If the two curves do not intersect, the droplet is predicted to evaporate completely without igniting.
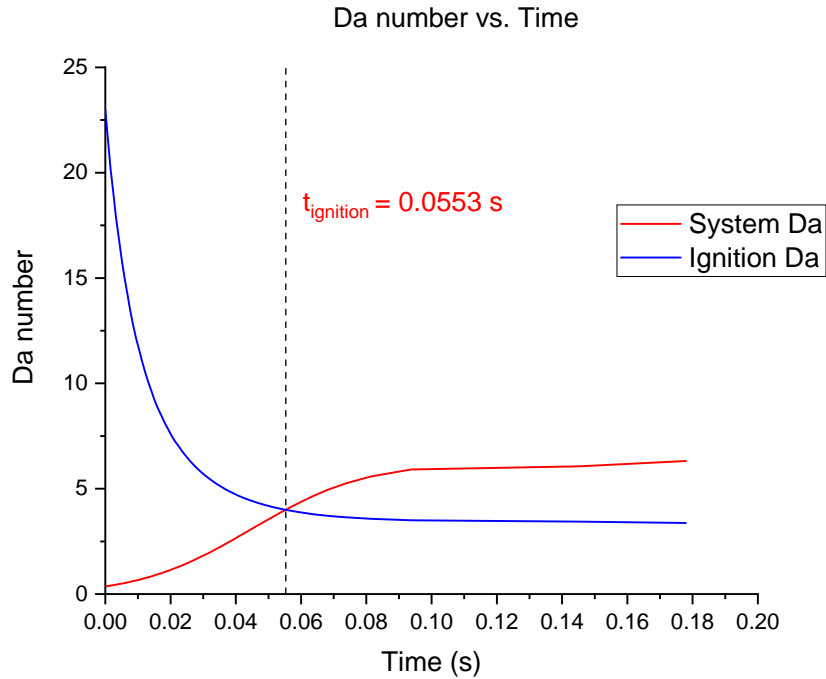
Figure 67. Evolution of system and ignition Da numbers for ignition prediction in QSDI model

The QSDI model predictions were compared to experimental ignition delay results for an average ambient temperature of 1650 K. The global activation energies used for the QSDI model have been obtained from either existing literature or have been extracted from the relevant ignition delay data with which the model is being compared. The second method requires data on the variation of ignition delay with ambient temperature. As discussed in Section 2.3.3, for a particular droplet

size, the slope of a plot of the logarithm of ignition delay versus inverse temperature ($\ln \tau$ vs. $1/T$), gives the ratio of apparent activation energy to universal gas constant (E_a/R_u), from which the apparent activation energy can be computed. Since in the current study the average ambient temperatures were limited to two (1337 K and 1650 K), activation energies obtained from the literature were used in the QSDI model comparisons. Similarly to the procedure used by Wong et al. [103], the overall activation energy used for methanol (33 kcal/mole) was obtained from Williams [104]. For NM and IPN, the decomposition activation energies used in the hybrid combustion model discussed in Section 4.7 were used here (50 kcal/mole for NM and 37 kcal/mol for IPN). The pre-exponential factors were then estimated from the best fit of the model predictions to the ignition delay data. An analysis of the results using activation energies obtained from both methods showed that the difference in the activation energies only changed the pre-exponential factors obtained from the best fits, however the trends predicted by the QSDI curves were consistent. Fuel-specific thermophysical and kinetic constants used in the model are summarized in Table 9. For consistency, the property notation is similar to Law [22] and Mawid and Aggarwal [24].

Table 9. Thermophysical and kinetic constants used in the QSDI model

Property	Methanol	IPN	NM
Q'[cal/g-K]	5415	4440	2776
L'[cal/g]	279	88.29	134.95
$E_a{}'$[kcal/mol]	33	37	50
B' [cm^3/mol-s]	2.26e10	2.67e10	2.91e13

Figure 68, Figure 69 andFigure 70 show model comparisons for methanol, NM and IPN, respectively. For all three fuels, the QSDI model was unable to predict the experimental trend, where no apparent variation of ignition delay with initial droplet diameter could be observed. For methanol, the model predicted an initial decrease of ignition delay with initial droplet diameter (kinetically-controlled regime) until a droplet diameter of ~1.08 mm which represented the minimum ignition delay (~51 ms). Beyond this droplet size, ignition delay was predicted to increase. Based on the best fit of the curve to the data, the model predicted that droplet diameters

below ~0.95 mm would evaporate completely without igniting (infinite ignition delay). However, at this ambient temperature, all methanol droplets in the range studied (~0.4 mm to 1.4 mm) were observed to ignite. A similar observation was made by Wong et al. [102] in their analysis of the validity of the ignition criteria derived for gas-phase quasi-steadiness. For n-heptane droplets igniting in an ambient temperature of 950 K and 1023 K, their analysis using the QSDI model did not predict the experimental data trend from both Faeth and Olson [6] and Takei et al. [23] as shown in Figure 71. They concluded that in the QSDI analysis, the reaction rates are significantly overestimated due to the neglect of fuel vapor accumulation processes, and in addition, the QSDI model is better used to determine minimum ignitable temperatures (though underestimations may exist) rather than ignition delays.
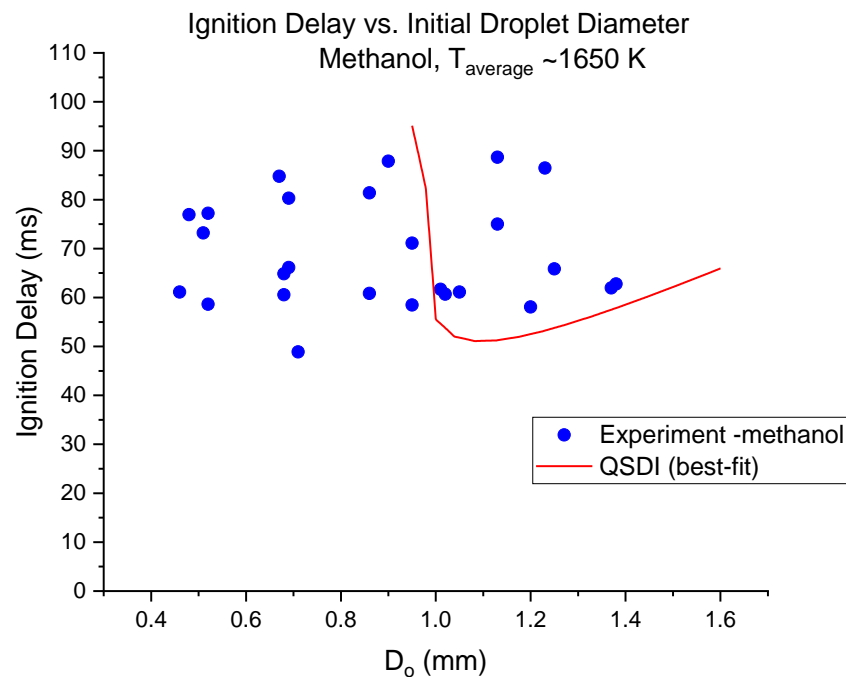
Figure 68. Comparison of QSDI ignition delay predictions with experimental ignition delay for methanol in T_{amb} ~1650 K

For NM droplets, the model predicted a monotonic increase in the ignition delay with increasing droplet size as shown in Figure 69, suggesting that NM droplets in this ambient temperature would only ignite in the diffusion-controlled regime. In addition, for an ambient temperature of 1650 K, the critical droplet diameter below which ignition would not occur was predicted to be ~0.37 mm.

Ignition delay predictions for IPN also showed that a small range of droplet diameters at this ambient temperature would ignite in the kinetically-controlled regime. In this regime, the ignition delay was predicted to decrease with increasing droplet diameter, until ~0.708 mm, after which it increased steadily as shown in Figure 70. Furthermore, the critical droplet diameter below which ignition would not occur was predicted to be 0.66 mm.

In general, the experimental ignition delay trends for all three fuels at an ambient temperature of ~1650 K were not replicable with the QSDI model. However, ignition in the kinetically-controlled regime was predicted for a large range of the methanol droplets (boiling point 64.7 ℃), but only for a few smaller droplet sizes for IPN (boiling point 101.5℃). No kinetically-controlled region was predicted for NM (boiling point 101.1℃). In addition, in the same conditions, the critical diameters below which ignition would not occur were larger for methanol than for NM and IPN, likely due to the difference in boiling points (volatility).
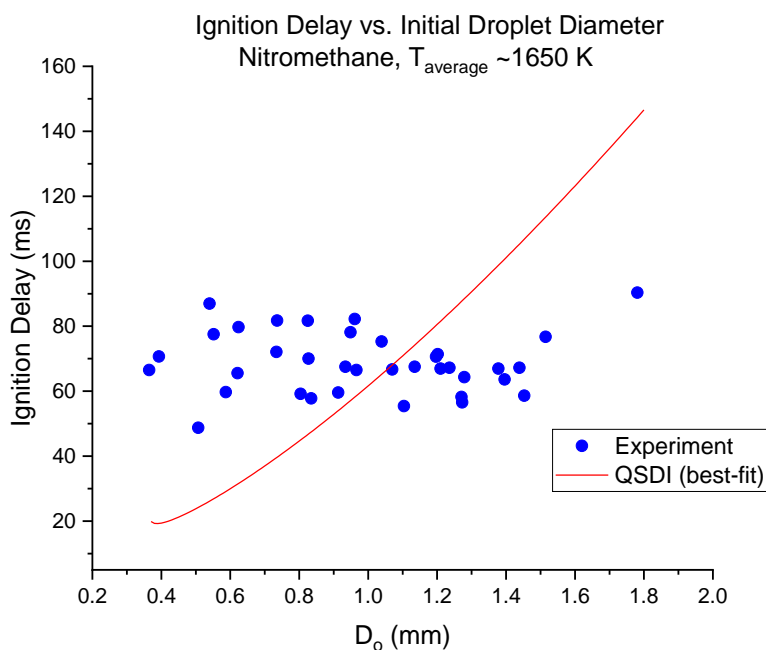
Figure 69. Comparison of QSDI ignition delay predictions with experimental ignition delay for nitromethane in T_{amb} ~1650 K
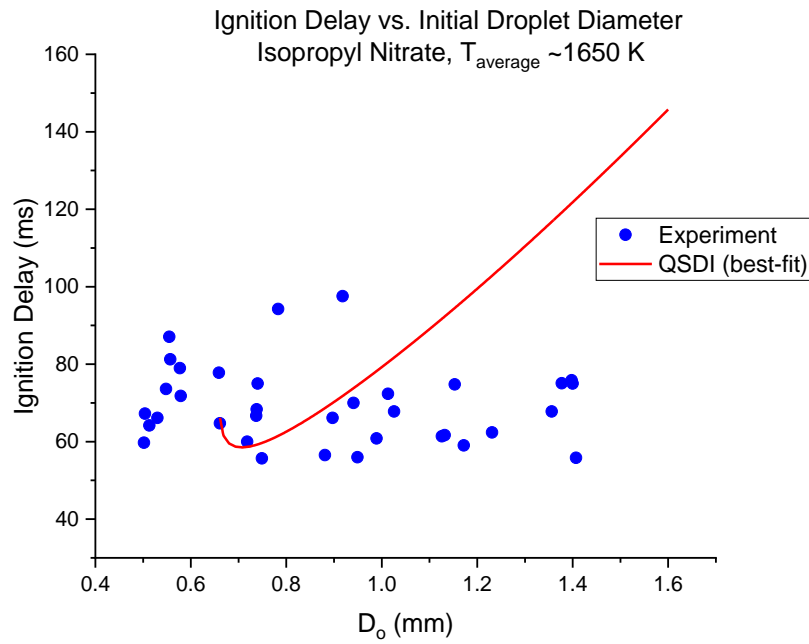
Figure 70. Comparison of QSDI ignition delay predictions with experimental ignition delay for isopropyl nitrate in T_{amb} ~1650 K
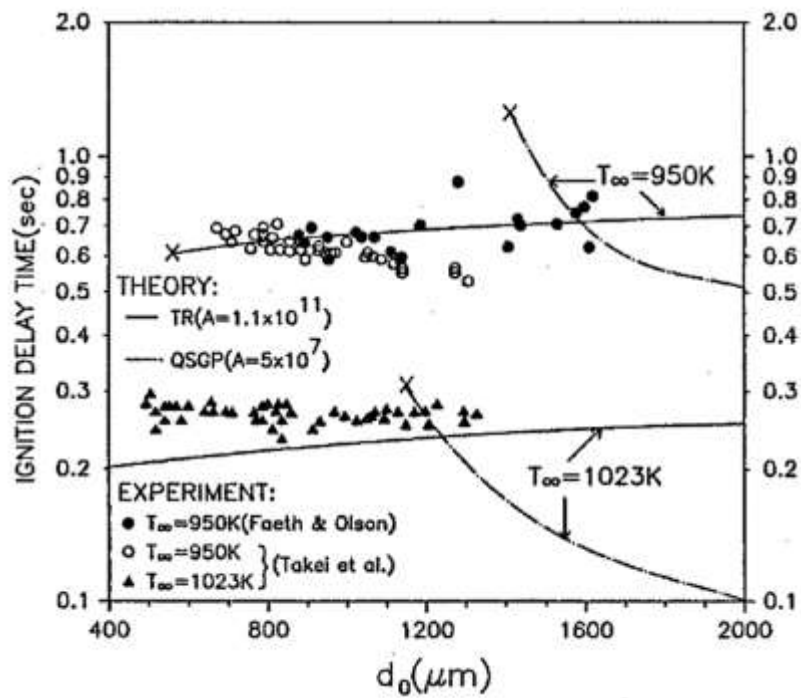
Figure 71. Comparison of transient and QSDI models with n-heptane experimental data [102]

5. SUMMARY AND RECOMMENDATIONS

A push towards greener alternatives for conventional rocket propellants such as monomethyl hydrazine (MMH) and hydrazine has motivated the investigation into HAN and HAN-based fuels as potential replacements. Two fuels which have gained considerable interest are the monopropellants nitromethane (NM) and isopropyl nitrate (IPN). NM has potential for use in space thrusters due to its high energy content and ease of storage, and can also be potentially used in bipropellant devices in combination with an oxidizer. IPN has been used in gas turbine engines and as a diesel cetane improver. Other advantages of both monopropellants include their non-toxicity, non-corrosiveness, affordability and low sensitivity to premature detonation.

The post combustion gases of a McKenna flat flame burner were used to provide the environment for investigating droplet ignition and combustion. The McKenna burner was chosen due to the flame stability and repeatability associated with the burner. The average temperature at specific locations was characterized using coherent anti-stokes Raman spectroscopy (CARS). At 2 in. above the burner, the average temperature was determined to be ~1650 K, with a standard deviation of 4%. At 5 in. above the burner, the average temperature was determined to be ~1337 K, with a standard deviation of ~17%. Due to this larger standard deviation, this condition was designated as 'quasi-steady'. Droplets with diameters ranging between 0.35 mm and 1.4 mm ignited and burned at these two locations above the burner. The experimental mass burning rates were compared to the hybrid combustion model, and the experimental ignition delays were compared to the quasi-steady droplet ignition model.

Over 200 experiments were conducted for methanol, NM and IPN droplets to investigate the effect of initial droplet size and ambient temperature on the ignition delay and mass burning rates of these droplets. To the author's knowledge, no existing data on droplet ignition delays for NM and IPN droplets has been reported in the literature. Qualitative flame structure observations were made, and both NM and IPN droplets exhibited the double-flame structure associated with hybrid combustion, where the inner flame represents the premixed decomposition or monopropellant flame, and the outer flame represents the diffusion bipropellant flame. At 2 in. above the burner (average temperature 1650 K), all the droplets ignited in the diameter range studied, and no

apparent variation was observed in the ignition delay both with initial droplet size and fuel type. In addition, all three fuels reported similar ignition delays between ~55 ms and ~90 ms. This could be attributed to the fact that at higher temperatures, reaction rates are extremely fast compared to vaporization or diffusion rates. Therefore, high temperatures are associated with ignition and burning in the diffusion-controlled regime. However, at these high temperatures, very little heating up of the droplet occurs before it ignites, and the physical processes of droplet heating and vaporization therefore do not play a very important role. Consequently, ignition delay becomes invariant with changes in the initial droplet diameter. Comparison of predictions from the quasi-steady ignition delay model with experimental results at 2 in. above the burner showed that the experimental ignition delay trends were not reproducible using the model. Similar observations were made by Wong et al. [102] for n-heptane droplets where ignition delays were significantly underpredicted by the model. The authors partly attributed this difference to the neglect of fuel accumulation effects.

At 5 in. above the burner (average temperature ~1337 K), ignition delays were longer for all three fuels. For methanol, a region of increasing ignition delay with decreasing droplet size was observed. This has been attributed to increase in Da number near the ignitable limit, where kinetic rates are no longer 'infinitely fast'. In the literature this trend has been referred to as ignition in the kinetically-controlled regime, where kinetic rates are the limiting factor in the ignition process. NM ignition delays at 5 in. also showed a slightly decreasing trend as droplet diameter increased, however no apparent trend was observed for IPN droplets at this height.

Mass burning rates were extracted from the slopes of the square diameter versus time. For all droplets, an initial heat up time was observed during which the droplet temperature increased after being exposed to the hot combustion gases. For all three fuels, burning rate constants were observed to increase with increasing initial droplet diameter. This was attributed to the effect of both natural and forced convection to augment burning rates for larger droplets due to the presence of more fuel vapor and combustion products surrounding the droplets. At ~1650 K average ambient temperature, IPN was found to have higher mass burning rates than NM and methanol. In addition, the rate of increase in mass burning rates with droplet size was found to be higher for IPN compared to NM and methanol, suggesting that convection effects had more of an influence

on IPN droplets than the other two fuels. At 5 in. above the burner, burning rate constants for all three fuels were lower as expected due to the lower ambient temperature. IPN droplets again experienced higher burning rates than NM and methanol.

In general, for NM and IPN, the classical D^2 Law was found to be in good agreement for relatively smaller droplet sizes, however burning rates for larger droplet sizes were underpredicted. The inclusion of convection effects through film theory augmented the burning rates significantly, greatly improving the agreement with NM burning rate data despite the model's design for bipropellant fuels. Burning rates for methanol were significantly overpredicted compared to the experiment, with and without the inclusion of convection effects. One possible reason is the presence of absorbed water which could result in either the augmentation or reduction in experimental burning rates depending on the amount of water absorbed. Burning rate curves for the D^2 Law with and without convection effects were shown to merge for smaller droplets, showing that convection effects are much more significant for relatively large droplet sizes. In addition, the semi-empirical hybrid combustion model was found to be in good agreement with NM and IPN mass burning rates. The hybrid combustion solution was also found to merge with the D^2 Law with and without convection effects for relatively small droplets. This suggested that for very small droplets, the bipropellant flame dominates the combustion process. Theoretical predictions from the hybrid combustion model for MMH droplets with diameters between 1 mm and 2 mm burning in an ambient temperature of 2530 K were comparable to those obtained in this study for NM and IPN.

As discussed previously, simultaneous CARS measurements at higher frequencies in a location below the droplet would provide valuable information about the variation of the ambient temperature immediately surrounding the droplet with time, and thus more accurate information about the ambient temperature at ignition. Furthermore, the small size of CARS probe volumes in general would enable the characterization of droplet flame temperatures. Additional experiments in a variety of ambient temperatures lower than those investigated in this study would be beneficial for characterizing the ignition and combustion of these fuels and for studying the influence of kinetic effects. To eliminate the effects of flow unsteadiness experienced at different heights while varying ambient temperature, several methods may be employed to reduce the ambient

temperatures experienced by the droplets while still maintaining a 2 in. height above the burner, and thus maintain a steady flow around the droplets. One such method would be the use of cool flames, or flames with lower adiabatic flame temperatures. Alternatively, a series of wire meshes at locations below the droplet could also be employed to reduce the temperature of the post-combustion gases through radiation heat losses. To ascertain the velocity of the post-combustion gases around the droplet, hot wire anemometry may be employed in order to better predict the type of secondary droplet breakup experienced by the different fuel droplets. Lastly, an expansion of the range of droplet sizes to those approaching sizes in practical systems would provide additional useful information on the effect of droplet size on the ignition and combustion of these fuels.

APPENDIX A: FUNDAMENTALS OF THE QSDI THEORY

In the quasi-steady droplet ignition theory, Aggarwal [14] represents the finite rate chemistry by a one-step irreversible reaction:

$$v_f F + v_o O \xrightarrow{k} v_p P \tag{24}$$
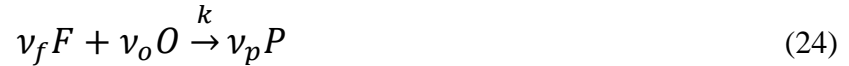
The governing equations are then non-dimensionalized using the parameters outlined in the nomenclature, and the species and temperature conservation equations are presented with the assumption of spherical symmetry as:

$$\frac{M}{r^2} \frac{dY_F}{dr} - \frac{1}{r^2} \frac{d}{dr}\left[r^2 \frac{dY_F}{dr} \right] = \dot{w} \tag{25}$$

$$\frac{M}{r^2} \frac{d(Y_{O\infty}/\sigma)}{dr} - \frac{1}{r^2} \frac{d}{dr}\left[r^2 \frac{d(Y_{O\infty}/\sigma)}{dr} \right] = \dot{w} \tag{26}$$

$$\frac{M}{r^2} \frac{dT}{dr} - \frac{1}{r^2} \frac{d}{dr}\left[r^2 \frac{dT}{dr} \right] = \dot{w} \tag{27}$$

The oxidizer concentration species term $Y_{O\infty}/\sigma$ presented in the formulation [24] represents the ambient oxidizer concentration divided by the stoichiometric mass ratio of oxidizer to fuel. This term indicates that the important fraction of the ambient oxidizer concentration is that which stoichiometrically reacts with the fuel. The production term, $\dot{w}$, is derived from the law of mass action, non-dimensionalized and re-arranged to give a term proportional to the Da number:

$$\dot{w} = Da \frac{Y_O^{a_O}}{M^2} \frac{\dot{Y_F}^{a_F}}{(T)^{a_O + a_F}} \exp\left(\frac{T_a}{T} \right) \tag{28}$$

where the Da number is given as:

$$Da = \frac{\nu_f B'(W_f')^{(1-a_f)}}{(\lambda_\infty'/C_{p\infty}')(W_f')^{a_o}} \left(\frac{p'C_p'}{R'Q'}\right)^{a_o+a_F} (M'r_s')^2 \tag{29}$$

It is important to note that the precise definition of the Da number is not essential and it may vary from scenario to scenario. It is only necessary that the Da number defines the ratio of a characteristic transport time of a particular system to a characteristic reaction time [60]. In Law's derivation, the Da number, when non-dimensionalized, is an approximate measure of the ratio of characteristic flow time ($\sim r_s/\lambda_g/(C_{pg}\rho_g)$) to characteristic reaction time (ρ_g/A) [95].

The boundary conditions for the governing equations are given as follows:

For $r = \infty$ (ambience):

$$Y_o = Y_{0\infty}/\sigma = \alpha \tag{30}$$

$$Y_f = 0 \tag{31}$$

$$T = T_\infty \tag{32}$$

For $r = 1$ (droplet surface):

$$\frac{dY_F}{dr} = -M(1 - Y_{Fs}) \tag{33}$$

$$\frac{dT}{dr} = MH \tag{34}$$

$$T = T_S \tag{35}$$

Figure 72 depicts the boundary conditions. It is important to note that the term in equation (33) communicates that the fuel mass fraction of the convective flux involves the difference between the fuel mass fraction within the droplet (which is unity by definition) and the fuel mass fraction in the gas phase at the droplet surface. A unity Lewis number assumes equality of the thermal and mass diffusion rates, and as a result, the convective heat flux though the droplet surface can be equated to the product of the rate of mass transfer and a change of enthalpy as shown in equation(34). In this case the change in enthalpy, , the effective latent heat of vaporization [13,58].
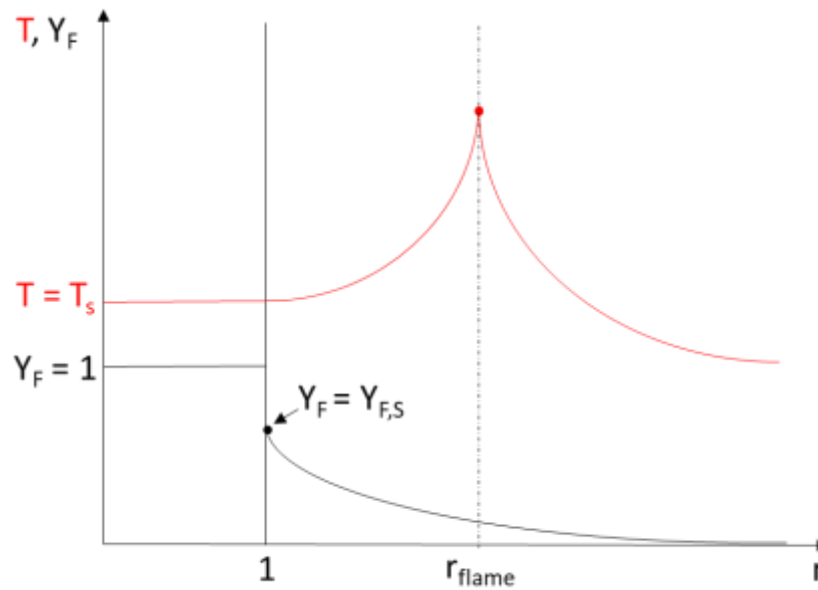
Figure 72. Fuel mass fraction and temperature profiles for a burning droplet (Adapted and modified from [104])

The Shvab-Zeldovich formulation is then used to express the species mass fractions in terms of temperature, effectively reducing the number of equations to a single energy equation. To numerically solve the energy equation, Law and others used asymptotic analysis and perturbation theory, considering ε as the small perturbation parameter, and the solution is presented in terms of burning rate as a function of Da number, thus yielding the S-curve of Figure 21.

The focus of the ignition theory is the lower part of the S-curve or the weakly-reacting branch, where Da_I is defined as the ignition or critical Da number. This section of the S-curve can be obtained by plotting the maximum perturbed temperature of the system, θ, in the limit as the

stretched coordinate variable, X, goes to infinity, as a function of a modified Da number for various values of the heat transfer parameter, β, as shown in Figure 73. The tangent values to the curves represent the critical or ignition Da numbers, such that the ignition criterion can be written as $\Delta \leq \Delta_I$, where the reduced or modified Da [14], Δ, is given as:

$$\Delta = \left\{ \frac{B'(W_f')^{(1-a_f)}}{\lambda_\infty'/C_{p\infty}'(W_O')^{a_o}} \left(\frac{p'C_p'}{R_u'Q'} \right)^{a_o+a_f} \right\} \times \left\{ \frac{(Y_{o\infty})^{a_o} \exp(-T_a'/T_\infty')(M'r_s')^2}{\left(\frac{C_p'T_\infty'}{Q'} \right)^{a_o+a_f} \left(\frac{C_p'T_\infty'^2}{T_a'Q'} \right)^{3-a_f}} \right\} \tag{36}$$

Here, X has been introduced as an inner stretched coordinate. In this case, stretching the coordinates helps explore in detail what is occurring on different length scales. The inner stretched coordinate is given as:

$$X = x/\varepsilon \tag{37}$$

where the coordinate transformation

$$x = 1 - \exp\left(-\frac{M}{r}\right) \tag{38}$$

has been made and represents the ambience surrounding the droplet and allows the region surrounding the droplet to be explored in more detail.
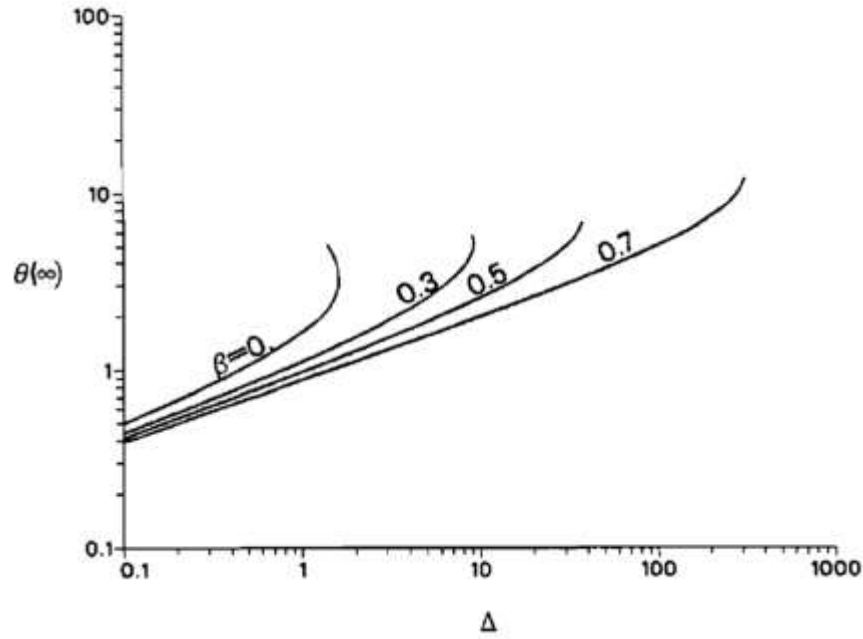
Figure 73. Maximum perturbed temperature vs. modified Da number for various values of heat transfer parameter [24]

Law and other investigators have presented an explicit expression of ignition Da number as a function of the heat transfer parameter, β. Law's expression is given by

$$\Delta_I = 1.05 \exp(6.40\beta) \qquad \text{for } \beta \leq 0.35 \qquad (39)$$

with the assumption of unity exponents for fuel concentration ($a_F = a_o = 1$), while Mawid and Aggarwal's [24] version is given by

$$\Delta_I = 0.9865 \exp(6.463\beta + 0.35) \qquad \text{for } \beta \leq 0.30 \qquad (40)$$

with a non-unity fuel exponent ($a_F = 0.25$).The two expressions yield results in good agreement with each other.

To predict ignition delay time, the general procedure begins with given fuel and ambient properties of the system. Time $t = 0$ represents the instant when the droplet is introduced into the hot environment after which it begins to heat up and vaporize. An appropriate droplet heating model is employed and at each time step, temporally-varying parameters are calculated including the

droplet surface temperature, T_s', the instantaneous droplet radius, r_s', and the ignition and system Da numbers. At each of these time steps, the two Da numbers are compared to check if the ignition criterion has been satisfied. The ignition delay time is defined as the instant when the ignition criterion $\Delta = \Delta_I$ has been satisfied [14].

APPENDIX B: NASA CEA OUTPUT

NASA-GLENN CHEMICAL EQUILIBRIUM PROGRAM CEA2, FEBRUARY 5, 2004

BY   BONNIE MCBRIDE AND SANFORD GORDON

REFS: NASA RP-1311, PART I, 1994 AND NASA RP-1311, PART II, 1996

```
**************************************************************************

 prob case=78958072  hp p(atm)=1
 phi=0.51
 reac
  fuel  CH4              wt%= 100.0 t,k= 298.15
  oxid  N2               wt%= 68.0 t,k=  298.15
  oxid  O2               wt%= 32.0 t,k=  298.15
   output massf
 output trans
 output short
 output trace= 1e-5
 end
```

THERMODYNAMIC EQUILIBRIUM COMBUSTION PROPERTIES AT ASSIGNED

PRESSURES

CASE = 78958072

	REACTANT	WT FRACTION (SEE NOTE)	ENERGY KJ/KG-MOL	TEMP K
FUEL	CH4	1.0000000	-74600.000	298.150
OXIDANT	N2	0.6800000	0.000	298.150
OXIDANT	O2	0.3200000	0.000	298.150

 O/F= 24.44402 %FUEL= 3.930197 R,EQ.RATIO= 0.510000 PHI,EQ.RATIO=
0.510000

THERMODYNAMIC PROPERTIES

```
P, BAR              1.0132
T, K                1842.47
RHO, KG/CU M     1.8690-1
H, KJ/KG           -182.76
U, KJ/KG           -724.90
G, KJ/KG          -17476.2
S, KJ/(KG)(K)       9.3860

M, (1/n)            28.257
(dLV/dLP)t        -1.00011
(dLV/dLT)p          1.0041
Cp, KJ/(KG)(K)      1.4863
GAMMAs              1.2492
SON VEL,M/SEC        822.9
```

TRANSPORT PROPERTIES (GASES ONLY)
  CONDUCTIVITY IN UNITS OF MILLIWATTS/(CM)(K)

VISC,MILLIPOISE 0.67161

 WITH EQUILIBRIUM REACTIONS

```
Cp, KJ/(KG)(K)      1.4863
CONDUCTIVITY        1.3696
PRANDTL NUMBER      0.7288
```

 WITH FROZEN REACTIONS

```
Cp, KJ/(KG)(K)      1.4024
CONDUCTIVITY        1.2761
PRANDTL NUMBER      0.7381
```

MASS FRACTIONS

```
*CO              5.9377-5
*CO2             1.0772-1
H2O              8.7914-2
```

```
*NO              3.6659-3
NO2              1.0365-5
*N2              6.5156-1
*O               3.6675-5
*OH              6.3491-4
*O2              1.4839-1
```

 * THERMODYNAMIC PROPERTIES FITTED TO 20000.K

 NOTE. WEIGHT FRACTION OF FUEL IN TOTAL FUELS AND OF OXIDANT IN TOTAL
OXIDANTS

APPENDIX C: DROPLET ANALYSIS MATLAB CODE

```matlab
%Monodisperse spray code
%Original Code: Ignition Movie Analysis by Timothée Pourpoint (2005)
%Modified by: Angela Mbugua - Jan 2015

clear all;
close all;
clc;
format short;
fontsize = 9;
NbBin = 240; %why?
NbElements = 10;
Plots = 1;
tic
%

NameIn = '10mmsil-t1-1-size.avi';

TitleFig = 'Methanol droplet';
CROPWINDOW = [400 120 140 700];  %xmin, ymin, width, height
Nbin = 240; %why?
NbElements = 10; %depends on how many you can expect for one value of
eccentricity, may change.
FirstPict = 1;
PictStep = 100;

FILEINFO = VideoReader(NameIn)
numFrames = FILEINFO.NumberOfFrames;
%LastPict = 670; %used to be numFrames

scrsz = get(0,'ScreenSize'); % Get screen size for optimal picture display

%Define new movie name, compression scheme and frame rate
NEWMOVIE = VideoWriter(['MovieAnalysis_',NameIn],'Uncompressed AVI');
NEWMOVIE.FrameRate = 1; %fps playback
RecordFrameRate = NEWMOVIE.FrameRate;
open(NEWMOVIE);
%Loop
i = 1; %Frame when droplet first 'enters' hot environment (nichrome wire sits
in position)

%displaying first image
MOV = VideoReader(NameIn);
X = read(MOV, i);
%X = imbinarize(X,'adaptive','ForegroundPolarity','dark','Sensitivity',0.3);
   % figure, imshow(X)


%imshow(X) %Displays first picture (i) of the movie

Time_index = 0;
```

```matlab
EDGEFILTER = 0.1; %edge filter sensitivity paramter (threshold)
%X = rgb2gray(X); %convert RGB image to grayscale intensity image, but X is
already gray scale
%AF = edge(X,'zerocross',[],'canny');

AF = edge(X,'zerocross',EDGEFILTER,'canny');
%AF = edge(X,'canny');
AF = imfill(X,'holes');

[B,L,N] = bwboundaries(AF,8,'noholes'); %traces exterior boundaries of holes
figure(1)
imshow(AF)
warndlg({'Select Known Length';'Ex: opposite corners of FOV';'Press ENTER
twice to acknowledge this message'})
pause
[X00,Y00] = ginput(1); %ginput --> graphical input from mouse
[X01,Y01] = ginput(1);
W = abs(X00-X01);
H = abs(Y00-Y01);


lengthscale = 80; %microns

alpha = lengthscale/H; %length scaling parameter in microns/pixel
%alpha = lengthscale/H;

j =1;
%LOOP

%Trying to remove background on all images in the movie
%MOV = VideoReader(NameIn);
%Xfirst = read(MOV, 1);
%A = size(Xfirst); %all frames are the same size

%for i = 2:10
%X = read(MOV,i);
%imshow(X)

%for r = 1:A(1)
%    for c = 1:A(2)
%        if (X(r,c) == Xfirst(r,c));
%            X(r,c)= 126; %number that will give me a nice clean background
(can vary)
%        end
%    end
%end
%imshow(X)
%end

endframe = numFrames - FirstPict;

while i < numFrames
```

```matlab
    Time_index = Time_index + 1;
    Time(Time_index) = (i - FirstPict)/5000.0; %How many seconds have elapsed

    MOV = VideoReader(NameIn);
    XP = read(MOV,i);
    %Xsub = read(MOV,26);
    %X = X - Xsub;
    %X = imshow(X);
%     X = imcrop(X,CROPWINDOW);  % X2 = imcrop(X, map, rect) crops the
indexed image X.  Cropping rectangle: [xmin ymin width height]
    %X is already in grayscale from PHOTRON, no need for rgb2gray
    %X = rgb2gray(X); %convert RGB image to grayscale intensity image, but X
is already gray scale
    figure
    [X,rect] = imcrop(XP);


    %Removing background:
    AF =
imbinarize(X,'adaptive','ForegroundPolarity','dark','Sensitivity',0.55);
    %AF = edge(X,'zerocross',EDGEFILTER,'canny');
     %figure
     %imshow(AF)
%     AF = imcomplement(AF);
    AF = not(AF);
%     figure
%     imshow(AF)
    AF = imfill(AF,'holes');
  %figure
  % imshow(AF)
    AreaW(Time_index)=round(bwarea(AF)); %Where do we use this?
    [B,L,N] = bwboundaries(AF,8,'noholes');
%     figure
%     imshow(~L)


%     figure
%     imshow(~L)
    stats =
regionprops(L,'Area','Centroid','Eccentricity','EquivDiameter','MajorAxisLeng
th','MinorAxisLength');
    equivD = stats.EquivDiameter
    equivD_units = [stats(:,1).EquivDiameter]*alpha;
    maxdiams = max(equivD_units);
    Diamdrop = [stats(:,1).EquivDiameter];
    diameters = mean([stats.MajorAxisLength stats.MinorAxisLength],2);
    radii = diameters/2;
    radiip = equivD/2;
    centers = stats.Centroid;

    %changed to microns (alpha = microns/pixel)
    Ecc = [stats(:,1).Eccentricity];
    MajorA = [stats(:,1).MajorAxisLength]*alpha; %microns
    MinorA = [stats(:,1).MinorAxisLength]*alpha; %microns
    Diametersrao = sqrt(MajorA.*MinorA);
```

```matlab
    Radius = [stats(:,1).EquivDiameter]*alpha/2; %microns
    Radius_m = Radius*1e-6; %Radius in m
    %Radiusdrop = Radius;%Magnification of size in composite plot (to be able
to see the drops better)
    %Diamdrop = [stats(:,1).EquivDiameter];
    MeanEcc(Time_index) = mean(Ecc);
    stdEcc(Time_index) = std(Ecc);
    MeanRad(Time_index) = mean(Radius);
    Radiinew(Time_index) = radii;
    equivdiams(Time_index) = equivD*alpha; %at each time index, there may be
more than one object, so the size of this array changes with time
    stdequiv(Time_index) = std(equivD*alpha); %is other than zero only when
there is more than one object
    stdRad(Time_index) = std(Radius); %is other than zero only when there is
more than one object
    %MaxMA = max(MajorA); % May need to rewrite this, likely inaccurate
    MaxD(Time_index) = max(Diamdrop)*alpha; %For single droplet videos, all
other objects are smaller than the actual droplet, so this represents the
droplet diameter we are looking for.
    MaxDiamrao(Time_index) = max(Diametersrao);
    massdrops = (Radius_m.^3).*(((4.0/3.0)*pi)*880); %KG  % Mass of closed
structures assuming ellipsoid volume * density of MMH (kg/m^3)
    Totalmass(Time_index) = sum(massdrops)*1000;  %GRAMS - Sum masses of all
closed structures on a given frame, convert kg to grams


    if Plots == 1

        iptsetpref('ImshowAxesVisible','off') %Set image processing
preferences, look at other preferences

        %Time display
        subplot('Position',[0.02 0.55 0.28 0.4],'FontSize', fontsize),
imshow(X)
        title([TitleFig, ' - Time = ', num2str(Time(Time_index)*1000), '
ms'],'FontSize',fontsize,'FontWeight','Bold','Color','Red')

        %BW display
        subplot('Position',[0.32 0.5 0.3 0.45],'FontSize', fontsize),
imshow(~L)
        title(['Frame #', num2str(i), ' of ', num2str(numFrames),', ',
num2str(N), '
objects'],'FontSize',fontsize,'FontWeight','Bold','Color','Red')
% Display original movie frame
        %plot the circles
        %Drawing the outline surrounding the object:
%     imshow(label2rgb(L, @jet, [.5 .5 .5]))
hold on
for k = 1:length(B)
  boundary = B{k};
  plot(boundary(:,2), boundary(:,1), 'w', 'LineWidth', 2)
end

%
%          hold on
% %          visboundaries(B)
```

```matlab
%           viscircles(centers,radiip);
%           hold off

        hold on

        subplot('Position',[0.62 0.55 0.28 0.4],'FontSize', fontsize)

        cla
        for h = 1:1:length(stats)
            Center(h,:) = [stats(h,1).Centroid(1) -stats(h,1).Centroid(2)];
            drop(h) = rsmak('circle',(Diamdrop(h)/2),Center(h,:));
            fnplt(drop(h))
            axis('equal')
            hold on
        end
        %axis([0 1024 -1096 0]) xmin xmax ymin ymax
        %axis([0 896 -824 0])
        axis([0 1024 -1024 0])
        %[400 350 700 700]
        title(['Composite Image with ', num2str(N), '
objects'],'FontSize',fontsize,'FontWeight','Bold','Color','Red')
        for h = 1:1:length(stats)
            %text(Center(h,1)+10,Center(h,2)+10,num2str(stats(h).MajorAxisLen
gth))
            tx = text(Center(h,1)+35,Center(h,2)-
20,num2str((stats(h,1).EquivDiameter)*alpha));
            tx.FontSize = 6;
        end

          %Radius histogram
%         subplot('Position',[0.05 0.05 0.38 0.4],'FontSize', fontsize),
hist(equivD_units, NbBin)
%         grid on;
%         xlabel('Diameter [microns]','FontSize',
fontsize,'FontWeight','Bold')
%         ylabel('Closed Structure #','FontSize',
fontsize,'FontWeight','Bold')
%         %axis([0 30e3 0 NbElements])
%         axis([0 1500 0 NbElements])
%         title(['Single Droplet diameter = ',
num2str(round(equivdiams(Time_index))), ', Std. Dev. = ',
num2str(round(stdequiv(Time_index))), ' , Peak @ ', num2str(round(maxdiams)),
'microns'],'FontSize',fontsize,'FontWeight','Bold','Color','Blue')


        %Diameter history graph
        subplot('Position',[0.05 0.05 0.38 0.4], 'FontSize', fontsize),
plot(Time(Time_index),MaxD(Time_index),'ob')
        grid on;
        xlabel('Time(s)','FontSize', fontsize,'FontWeight','Bold')
        ylabel('Equivalent Diameter','FontSize',fontsize,'FontWeight','Bold')
        title(['Single Droplet Diameter (microns) = ',
num2str(round(equivdiams(Time_index)))],'FontSize',fontsize,'FontWeight','Bol
d','Color','Blue')
        hold on
```

```matlab
        %Eccentricity histogram
        subplot('Position',[0.55 0.05 0.45 0.4],'FontSize',
fontsize),hist(Ecc, NbBin)
        grid on;
        xlabel('Eccentricity','FontSize', fontsize,'FontWeight','Bold')
        ylabel('Closed Structure #','FontSize', fontsize,'FontWeight','Bold')
        axis([0 1 0 NbElements])
        title(['Mean Value = ', num2str(MeanEcc(Time_index)), ', StdDev = ',
num2str(stdEcc(Time_index))],'FontSize',fontsize,'FontWeight','Bold','Color',
'Blue')


    else

        disp('imaging and plotting turned off')


    end
    stats_history(i-FirstPict+1) = stats(1).MajorAxisLength;
    M = getframe(gcf);
    writeVideo(NEWMOVIE, M)

    i = i + PictStep;

    %prompt = ('Should I continue? Press Enter for yes');
    %pause

end
close(NEWMOVIE)
%close all;

 %nfig = 1;

% figure(3)
% axes('FontSize', 20)
% hold on;
% grid on;
% %plot(Time, MeanRadmic,'LineWidth',2)
% plot(Time, Radiinew*2*alpha)
% title('Droplet Diameter')
% xlabel('Time [s]')
% ylabel('Diameter [/mu]')
% %nfig = nfig + 1;

figure(3)
axes('FontSize', 20)
hold on;
grid on;
%plot(Time, MeanRadmic,'LineWidth',2)
plot(Time, MaxD,'o')
title('Droplet Equivalent Diameter')
xlabel('Time [s]')
ylabel('Diameter [/mu]')
%nfig = nfig + 1;
```

```
% figure(4)
% axes('FontSize', 20)
% set(5,'Name','Std Dev Diameter');
% hold on;
% grid on;
% %plot(Time, stdRadmic,'LineWidth',2)
% plot(Time, stdequiv)
% title('Std Dev Diameter')
% xlabel('Time [s]')
% ylabel('Std Dev Diameter [-]')
% %
```

APPENDIX D: DROPLET IGNITION THEORY MATLAB CODE

```matlab
%Prediction of Ignition Delays of Nitromethane in Post combustion gases of
%a flat flame burner

clear all, close all, clc

NMexptldata = load('nmID.txt');
NMexD = NMexptldata(:,1);
NMexID = NMexptldata(:,2);


Tinf_prime = 1650;%K - Ambient temperature

Yo_inf = 0.148; % ambient oxidizer mass fraction based on ~0.131 mole
fraction at phi = 0.51
ao = 1.5; % Law Theory - oxygen exponent
af = 0.25; %Law Theory - oxygen exponent
%DIMENSIONAL VALUES
%Dso_primes = 1.0545; %mm
Dso_primes = [0.1:0.01:1.8]; %Range of diameters in mm
rso_prime = Dso_primes./20; %In cm
Zprime = Yo_inf.*(rso_prime.^2);
%Zprime = 0.0000463669;
%Z' = Yo_inf*(rso'^2) correponding to droplet sizes between ~0.06-~1.8mm

%rso_prime = sqrt(Zprime./Yo_inf);

for j = 1:numel(Zprime)

Ts_prime = 300:0.5:358; %K %Range of droplet surface temperatures guessed

%CHEMICAL KINETICS PARAMETERS: Results sensitive to choice of
%B' = (pre-exponential factor)

 E_prime = 50e3; %cal/mole %Previous is 53e3;
 B_prime = 2.9082e13; %cm3/mole-s  %B_prime = 5e16; %cm3/mole-s %Previous is
7.8e15;4
Wf_prime = 61.04; %g/mole %Molecular weight of the fuel
Q_prime = 2776; %cal/g %Heat release per unit mass of fuel consumed (Heat of
combustion)
Ru_prime = 1.986; %cal/molK %Universal gas constant
R_prime_f = 1.9859/Wf_prime; %cal/gK %Fuel specific gas constant
R_prime = 7.03e-2; %cal/gmK specific gas constant of the ambient gases
Ta_prime = E_prime/Ru_prime; %Activation temperature


Wo_prime = 32; %g/mole Oxidizer (Oxygen) molecular weight
Winf_prime = 28.25; %g/mol Molecular weight of the ambient gases (CEA)
% Wf_Wavg = 0.5; %Wavg is the average molecular weight of all the gas species
at the surface except the fuel...
%here we are assuming realistically (law 1976) that the fuel vapor is
%saturated at the droplet surface
rhoD_inf = 0.67161e-3; %gm/cm-sec Dynamic viscosity of the ambient gases
(CEA)
```

```matlab
Cp_p = 0.355; %cal/gmK Specific heat at constant pressure of the ambient
gases (CEA)
Pinf_prime = 0.0242; %cal/cm^3 which is = 1 atm Ambient pressure
Pinf_prime_atm = 1; %ambient pressure in atmospheres
Lp = 134.95; %cal/gm Fuel (NM) specific latent heat of vaporization
Tb_p = 373.2; %K Fuel (NM) boiling point
rho_l_p = 1.137; %gm/cm3 Fuel (NM) liquid density


%NON-DIMENSONAL AND NON-DIMENSONALIZED VALUES
Ts = (Cp_p/Q_prime).*Ts_prime; %Non-dimensional temperature
Tinf = Cp_p.*Tinf_prime/Q_prime;%Non-dimensional temperature
L = Lp/Q_prime;%Non-dimensional latent heat of vaporization

%IMPLEMENTATION OF RAPID MIXING MODEL OF DROPLET HEATING:

%CONSTANTS
alpha = exp(-Lp/(R_prime*Tb_p));
gam = Cp_p*Lp/(Q_prime*R_prime);

%*****************************************************
% %Calculating Yfs: Mole fraction of the fuel vapor at the droplet surface
Psat_Pb = exp((-Lp/R_prime_f)*(1./Ts_prime - 1/Tb_p)); %Pb here is 1 atm
% %Since P is 1 atm:
Xfs = (1/Pinf_prime_atm)*Psat_Pb;
% %Interface mixture molecular weight:
Wmix_prime = Xfs.*Wf_prime + (1-Xfs).*Winf_prime;
%*****************************************************

%CALCULATING TEMPORAL VARIABLES LAW'S WAY
%We assume that fuel vapor is saturated at the droplet surface
Yfs = (1+(Wf_prime./Wmix_prime).*((alpha*Pinf_prime_atm).*exp(gam./Ts) -
1)).^(-1);
H = (Tinf-Ts).*((1./Yfs)-1);
Beta = Tinf - Ts + H;
M = log(Beta./H); %Make sure this is correct M to feed into the other code

%Initializing droplet radius array
rs_prime(1) = rso_prime(j);
rs(1) = 1;

%calculating rs & rs_prime
for i = 2:numel(Ts)
Integrand1 = (-2/3)*(1./(H(1:i)-L));
Int1(i) = trapz(Ts(1:i),Integrand1);
rs(i) = exp(Int1(i));
rs_prime(i) = rs(i).*rso_prime(j);
end

t(1) = 0;
%calculating time

for i = 2:numel(Ts)
Integrand2 = (2/3)*((rs(1:i).^2)./(M(1:i).*(H(1:i)-L)));
t(i) = trapz(Ts(1:i),Integrand2);
tterm = (2*rhoD_inf)/(rho_l_p*rso_prime(j)^2);
t_prime(i) = t(i)/tterm;
```

```matlab
end

%Calculating Damkohler number (Aggarwal)
term1 = B_prime*Wf_prime^(1-af)/(rhoD_inf*Wo_prime^ao);
term2 = (Pinf_prime*Cp_p/(Ru_prime*Q_prime))^(ao+af);
term3 = (Yo_inf^ao)*exp(-Ta_prime/Tinf_prime).*((rs_prime.^2).*M.^2);
term4 =
((Cp_p*Tinf_prime/Q_prime)^(ao+af))*((Cp_p*Tinf_prime^2/(Ta_prime*Q_prime))^(
3-af));
System_Da = term1*term2*term3/term4;
Ignition_Da = 0.9865.*exp(6.463.*Beta + 0.35); %Aggarwal 1989
%Ignition_Da = 1.05.*exp(6.40.*Beta); %Law 1978
[System_Da',Ignition_Da'];

%Limiting scope of Da numbers because they backtrack on themsleves
% for k = 1:numel(System_Da)
%     if System_Da(k-1)>System_Da(k)
%         New


%Finding Ignition Delay:

ROBUST = 1;

[tp,Dp_int] = intersections(t_prime,System_Da,t_prime,Ignition_Da,ROBUST);
if isempty(tp)
  Predicted_ID(j) = 0;
 elseif numel(tp)>1
     Predicted_ID(j) = tp(1);
else
  Predicted_ID(j) = tp;
end

% figure
% plot(Ts_prime,System_Da,'r')
% hold on
% plot(Ts_prime,Ignition_Da,'b')
% plot(Ts_prime(p),System_Da(p),'og')
% xlabel('Droplet Surface Temperature (K)')
% ylabel('Damkohler Number')
% title('Law Work: N-hexadecane Droplet Ignition, Tso = 300, rso ~ 66 mic,
T_a_m_b=1600K, P_a_m_b=1atm')
% legend('System Da','Ignition Da')
%
% figure
% plot(t_prime,System_Da,'r')
% hold on
% plot(t_prime,Ignition_Da,'b')
% %plot(t_prime(p),System_Da(p),'og')
% xlabel('time(s)')
% ylabel('Damkohler Number')
% title('Law Work: N-hexadecane Droplet Ignition, Tso = 300, rso = 66 mic,
T_a_m_b=1600K, P_a_m_b=1atm')
% legend('System Da','Ignition Da')

% aa = Dso_primes(j)
% bb = Predicted_ID(j)
```

```matlab
% %
% figure
% plot(t_prime,Ts_prime)
% xlabel('time(s)')
% ylabel('Droplet surface temperature (K)')
% title('Droplet surface temperature variation (rso = 66 mic, T_a_m_b=1400K,
Tso=300K)')

end

% figure
% plot(rso_prime*2*10000,Predicted_nondim_ID,'or')
% %hold on
% %plot(rso_prime*2*10000,WithWfeq1,'*b')
% %set(gca, 'YScale', 'log')
% xlabel('initial droplet diameter, Do (microns)')
% ylabel('non-dim ID time')
% title('ID vs rso, T_a_m_b=1600K, Tso=300K, P=1atm')
% %legend('W_b_a_r varying','W_b_a_r = 1')

p = find(Predicted_ID == 0);
Predicted_ID(p) = [];
diam_prime_mic = rso_prime.*(2*10);
diam_prime_mic(p) = [];

figure
plot(diam_prime_mic,Predicted_ID*1000,'b')
xlabel('initial droplet diameter, Do (mm)')
ylabel('ID time (ms)')
hold on
plot(NMexD,NMexID,'or')
title('Nitromethane ID vs rso, T_a_m_b=1650K, Tso=300K, P=1atm')

% figure
% plot(t_prime, System_Da,'b')
% hold on
% plot(t_prime, Ignition_Da,'r')
% xlabel('time(s)')
% ylabel('Da number')
% legend('System D_a','Ignition D_a')
```

APPENDIX E: HYBRID COMBUSTION MODEL AND D^2 LAW MATLAB CODE

```matlab
clc, close all, clear all
%Hybrid Combustion Model - NM Comparison

data = load('NM_exptl_data.txt');
Do_cm = data(:,1); %cm
M_gps = data(:,2); %g/s

D_l = .035:0.001:0.180; %Initial droplet diameter in cm 0.35 mm to 1.5mm
for i = 1:numel(D_l)
r_l = D_l(i)/2; %Initial droplet radius in cm
T_inf = 1650; %K  %Ambient temperature
YO_inf = 0.148; %Ambient oxidizer concentration

T_l = 373.2; %liquid droplet temperature = fuel boiling point in Kelvin
rho_l = 1.137; %g/cm3 MMH
gam = 0.37; %stoic ratio? "Stoic coefficient" for NM decomp products
L_F = 134.95; %Latent heat of vaporization of NM, cal/g

C_P = 0.5; %specific heat at constant pressure, biprop flame products -
cal/gK - NM
C_F = 0.461;  %specific heat at constant pressure, fuel - cal/gK - NM
C_FP = 0.425;  %specific heat at constant pressure, decomp flame products -
cal/gK - NM
C_O = 0.355;  %specific heat at constant pressure, ambient gas (containing
oxidizer) - cal/gK - CEA
R = 1.987204; % Universal gas constant, cal/molK

lambda_A_l = 3.27e-5; %thermal conductivity in region A - NM vapor (cal/cm-s-
K)
lambda_B_l = 4.33e-4; %thermal conductivity in region B, cal/cm-s-K (cal/cm-
s-K)
lambda_C_l = 3.27e-4; %thermal conductivity in region C - ambient gases
(cal/cm-s-K)

q1 = -167; %me for NM
q2 = -7093; %me for NM

sigma = (1+gam)*C_P - gam*C_O; %Allison

%for i = 1: length(r_l)
    L_star = L_F/(C_F*T_inf); %Allison eq 3.31 pg 31
    Q1 = q1/(C_FP*T_inf); %Allison eq 3.32 pg 31
    Q2 = q2/(sigma*T_inf);%Allison eq 3.33 pg 31
    theta_l = T_l/T_inf;%Allison eq 3.30 pg 31
    theta_ref = 298/T_inf;%Allison eq 3.30 pg 31
    beta_inf = beta_inf_fcn2(r_l,T_inf);%Allison eq 3.29 pg 31

    A = 0.042;
    E = 50*1000; %Activation energy cal/mole (0,10,30)

    %%Solve system of 4 eqns for Beta_I, Beta_f, theta_I and m_dot
```

```matlab
    syms theta_f beta_I beta_f theta_I m_dot
    vars = [theta_f beta_I beta_f theta_I m_dot];

    eqn_zero = theta_f - ((1-theta_ref+Q2)/(((gam +
YO_inf)/gam)^(sigma/C_O))) - theta_ref + Q2 == 0;

    %equation 1
    eqn1 = (m_dot*C_F/(lambda_A_l*r_l))*(1 - (1/beta_I)) -
(1/theta_l)*(theta_I - theta_l - (L_star - theta_l)*log((theta_I - theta_l +
L_star)/L_star)) == 0;
    %equation 2
    eqn2 = (m_dot*C_FP/(lambda_B_l*r_l))*((1/beta_I) - (1/beta_f)) -
(1/theta_l)*(theta_f - theta_I - (Q1 - theta_ref)*log((theta_f - theta_ref +
Q1)/(theta_I - theta_ref + Q1))) == 0;
    %equation 3
    eqn3 = ((m_dot*sigma/(lambda_C_l*r_l))*((1/beta_f)-(1/beta_inf))) -
(1/theta_l)*(1 - theta_f - (Q2 - theta_ref)*log((1-theta_ref+Q2)/(theta_f-
theta_ref+Q2))) == 0;
    %equation 5
    eqn5 = m_dot - (beta_I^2)*(r_l^2)*A*exp(-E/(2*R*theta_I*T_inf))== 0;

  S = vpasolve(eqn_zero, eqn1, eqn2, eqn3, eqn5, vars,4);


    soln_beta_I = (S.beta_I);
    soln_theta_f = (S.theta_f);
    soln_beta_f = (S.beta_f);
    soln_theta_I = (S.theta_I);
    soln_beta_inf = (beta_inf);
    r_f = soln_beta_f*r_l;
    r_I = soln_beta_I*r_l;
    m_dot = (S.m_dot);

    pi = 3.1416;
    M_dot(i) = 4*pi*m_dot;

end



figure
plot(D_l*10,M_dot,'-r')
hold on
plot(Do_cm*10,M_gps,'ob')
title('Mass burning rate output')
xlabel('Droplet Diameter (mm)')
ylabel('Mass burning rate (g/sec)')



clc, close all, clear all
%Hybrid Combustion Model - IPN Comparison

data = load('IPN_exptl_data.txt');
Do_cm = data(:,1); %cm
M_gps = data(:,2); %g/s
```

```matlab
D_l = .01:0.001:0.180; %Initial droplet diameter in cm 0.35 mm to 1.5mm
for i = 1:numel(D_l)
r_l = D_l(i)/2; %Initial droplet radius in cm
T_inf = 1650; %K  %Ambient temperature
YO_inf = 0.148; %Ambient oxidizer concentration


T_l = 374.65; %liquid droplet temperature = fuel boiling point in Kelvin
rho_l = 1.04; %g/cm3 MMH
gam =0.9; %stoic ratio? "Stoic coefficient" for NM decomp products
L_F = 88.29; %Latent heat of vaporization of NM, cal/g

C_P = 0.528; %specific heat at constant pressure, biprop flame products -
cal/gK - NM
C_F = 0.561;  %specific heat at constant pressure, fuel - cal/gK - NM
C_FP = 0.7043;
C_O = 0.355;  %specific heat at constant pressure, ambient gas (containing
oxidizer) - cal/gK - CEA
R = 1.987204; % Universal gas constant, cal/molK

lambda_A_l = 3.27e-5; %thermal conductivity in region A - NM vapor (cal/cm-s-
K)
lambda_B_l = 4.86e-4; %thermal conductivity in region B, cal/cm-s-K (cal/cm-
s-K)
lambda_C_l = 3.27e-4; %thermal conductivity in region C - ambient gases
(cal/cm-s-K)

q1 = 349; %me for IPN
q2 = -1610; %me for IPN

sigma = (1+gam)*C_P - gam*C_O; %Allison


    L_star = L_F/(C_F*T_inf); %Allison eq 3.31 pg 31
    Q1 = q1/(C_FP*T_inf); %Allison eq 3.32 pg 31
    Q2 = q2/(sigma*T_inf);%Allison eq 3.33 pg 31
    theta_l = T_l/T_inf;%Allison eq 3.30 pg 31
    theta_ref = 298/T_inf;%Allison eq 3.30 pg 31
    beta_inf = beta_inf_fcn2(r_l,T_inf);%Allison eq 3.29 pg 31


    A = 0.86;
    E = 37*1000; %Activation energy cal/mole (0,10,30)

    %%Solve system of 4 eqns for Beta_I, Beta_f, theta_I and m_dot
    syms theta_f beta_I beta_f theta_I m_dot
    vars = [theta_f beta_I beta_f theta_I m_dot];

    %equation 0
    eqn_zero = theta_f - ((1-theta_ref+Q2)/(((gam +
YO_inf)/gam)^(sigma/C_O))) - theta_ref + Q2 == 0;
    %equation 1
    eqn1 = (m_dot*C_F/(lambda_A_l*r_l))*(1 - (1/beta_I)) -
(1/theta_l)*(theta_I - theta_l - (L_star - theta_l)*log((theta_I - theta_l +
L_star)/L_star)) == 0;
    %equation 2
```

```matlab
    eqn2 = (m_dot*C_FP/(lambda_B_l*r_l))*((1/beta_I) - (1/beta_f)) -
(1/theta_l)*(theta_f - theta_I - (Q1 - theta_ref)*log((theta_f - theta_ref +
Q1)/(theta_I - theta_ref + Q1))) == 0;
    %equation 3
    eqn3 = ((m_dot*sigma/(lambda_C_l*r_l))*((1/beta_f)-(1/beta_inf))) -
(1/theta_l)*(1 - theta_f - (Q2 - theta_ref)*log((1-theta_ref+Q2)/(theta_f-
theta_ref+Q2))) == 0;
    %equation 5
    eqn5 = m_dot - (beta_I^2)*(r_l^2)*A*exp(-E/(2*R*theta_I*T_inf))== 0;

  S = vpasolve(eqn_zero, eqn1, eqn2, eqn3, eqn5, vars,4);

    soln_beta_I = (S.beta_I);
    soln_theta_f = (S.theta_f);
    soln_beta_f = (S.beta_f);
    soln_theta_I = (S.theta_I);
    soln_beta_inf = (beta_inf);
    r_f = soln_beta_f*r_l;
    r_I = soln_beta_I*r_l;
    m_dot = (S.m_dot);

    pi = 3.1416;
    M_dot(i) = 4*pi*m_dot;

end


figure
plot(D_l*10,M_dot,'-r')
hold on
plot(Do_cm*10,M_gps,'ob')
title('Mass burning rate output')
xlabel('Droplet Diameter (mm)')
ylabel('Mass burning rate (g/sec)')
```

```matlab
function [beta_inf,Re,Pr] = beta_inf_fcn(r_l,T_inf)

R = 1.987204; %universal gas constant - cal/K.mol
P = 0.024217; %cal/cm3 = 1 atm = 14.7 psia for use in the density equation in
allison' thesis page 80
bo2 = [0.248,1.67e-5,2.02e-4,2.73e-7,4.55e-5,1.322e-7];
bo = [0.282,1.67e-5,1.85e-4,2.5e-7,7.18e-5,1.282e-7];
bn2 = [0.282,1.21e-5,1.52e-4,2.35e-7,3.18e-5,1.232e-7];
bno = [0.277,0.72e-5,1.95e-4,2.55e-7,3.70e-5,1.321e-7];
bco2 = [0.298,1.35e-5,1.52e-4,2.35e-7,1.19e-5,1.397e-7];
bco = [0.292,0.85e-5,1.63e-4,2.35e-7,3.20e-5,1.282e-7];

%For Yo_inf = 0.148, v_inf = 40.1 cm/s CEA McKenna Burner
x_co = 5.9901e-5;
x_co2 = 6.9166e-2;
x_no = 3.4522e-3;
x_n2 = 6.5723e-1;
x_o = 6.4774e-5;
```

```
x_o2 = 1.3104e-1;
x_h2 = 2.9965e-5;
x_h2o = 1.3789e-1;


%Specific heats for the various ambient species in cal/g-K values at 25C
%and one atmosphere
%C_co = 0.243;
C_co = bco(1) + bco(2)*T_inf;
C_co2 = bco2(1) + bco2(2)*T_inf;
C_no = bno(1) + bno(2)*T_inf;
C_n2 = bn2(1) + bn2(2)*T_inf;
C_o = bo(1) + bo(2)*T_inf;
C_o2 = bo2(1) + bo2(2)*T_inf;


%Molecular weights in g/mol:
Mco = 28.01;
Mco2 = 44.01;
Mno = 30.01;
Mn2 = 28.01;
Mo = 16;
Mo2 = 32;
Mh2 = 2.01;
Mh2o = 18.01;


%Viscosity calculation for ambient conditions in g/cm-s - properties -
Allison for Pr
%and Re in g/cm.s
mu_co = x_co*(bco(3) + bco(4)*T_inf);
mu_co2 = x_co2*(bco2(3) + bco2(4)*T_inf);
mu_no = x_no*(bno(3) + bno(4)*T_inf);
mu_n2 = x_n2*(bn2(3)+ bn2(4)*T_inf);
mu_o = x_o*(bo(3) + bo(4)*T_inf);
mu_o2 = x_o2*(bo2(3) + bo2(4)*T_inf);


mu = mu_co + mu_co2 + mu_no + mu_n2 + mu_o + mu_o2;


%Thermal conductivities of the various species in cal/cm.s.K values at 25C
%and one atmosphere
%k_co = 5.5449e-5;
k_co = bco(5) + bco(6)*T_inf;
k_co2 = bco2(5) + bco2(6)*T_inf;
k_no = bno(5) + bno(6)*T_inf;
k_n2 = bn2(5) + bn2(6)*T_inf;
k_o = bo(5) + bo(6)*T_inf;
k_o2 = bo2(5) + bo2(6)*T_inf;


k_all = x_co*k_co + x_co2*k_co2 + x_no*k_no + x_n2*k_n2 + x_o*k_o +
x_o2*k_o2;


%Density calculation for ambient conditions - properties - Allison for Pr
%and Re
rhocoeff_co = x_co*Mco/(R*T_inf);
rhocoeff_co2 = x_co2*Mco2/(R*T_inf);
rhocoeff_no = x_no*Mno/(R*T_inf);
rhocoeff_n2 = x_n2*Mn2/(R*T_inf);
rhocoeff_o = x_o*Mo/(R*T_inf);
rhocoeff_o2 = x_o2*Mo2/(R*T_inf);
```

```
rho = P*(rhocoeff_co + rhocoeff_co2 + rhocoeff_no + rhocoeff_n2 + rhocoeff_o
+ rhocoeff_o2);%g/cm3

%Specific heat calculation for ambient conditions - properties - Allison for
Pr
%and Re
Spec1 = x_co*Mco*C_co + x_co2*Mco2*C_co2 + x_no*Mno*C_no + x_n2*Mn2*C_n2 +
x_o*Mo*C_o + x_o2*Mo2*C_o2;
Spec2 = x_co*Mco + x_co2*Mco2 + x_no*Mno + x_n2*Mn2 + x_o*Mo + x_o2*Mo2;
C_all = Spec1/Spec2;

%Reynolds number - ambient properties
v_s = 40.1; %cm/s
D_l = 2*r_l; %cm
Re = rho*v_s*r_l/mu;
%Prandtl number - ambient properties
Pr = C_all*mu/k_all;
g = 981; %gravitational accelration in cm/s2

%Grashoff and Nusselt numbers
Gr = ((rho^2)*(g)*(D_l^3))/(mu^2);

Nu_st = 2 + 0.6*(Gr^(1/4))*(Pr^(1/3));

Nu = (1 + 0.278*(Re^(1/2))*(Pr^(1/3))*(1+1.237*(1/Re)*(Pr^(-4/3)))^(-
0.5))*Nu_st;

beta_inf = Nu/(Nu - 2);

end
```

```
clear all, close all, clc
%D2 law theory comparison of NM droplet combustion data
%k_expt (experimental burning rate constant) is obtained from the linear
%graph of (DS/DO)^2 vs Time (s)
%This comparison calculates the predicted burning rate constant and burning
%rate from quasi-steady droplet combustion theory
%As per Chowdhury et al (2018), properties of the liquid fuel, fuel vapor
%and surrounding atmosphere are simplified by evaluating them at an average
%temperature between flame temperature and boiling point of NM
%Gas properties were obtained from CEA calculations

%Experimental Data
ExData = load('expdata_2inch_p51_NM.txt');
ExD = ExData(:,1);
ExK = ExData(:,2);

DATS = load('NM_exptl_data.txt');
dDATS = DATS(:,1).*10; %experimental diameter in mm
MDATS = DATS(:,2); %Experimental mass burning rate in g/s

%Theory
D = (0.30:0.005:1.8)*10^-3; %series of droplet diameters ranging between
0.3mm and 1.8mm
```

```matlab
%Loading conditions data info from CEA calculations. Filename
= %cond_props.dat
Conds = load('cond_props.dat');
O2concs = Conds(:,1).*0.01; %Mole fraction
Tads = Conds(:,2);%K
mus = Conds(:,3);%Pa.s
ks = Conds(:,4);%W/mK
Cps = Conds(:,5);%J/kgK
rhos = Conds(:,6);%kg/m3
Prs = Conds(:,7);
Us = Conds(:,8);%m/s

%Prompt1 = 'What condition are you running (1-14)?';
%p = input(Prompt1);
p = 7;
%Temperatures
Ts = 373; %K, boiling point of NM
Prompt2 = 'What is the measured ambient temperature surrounding the droplet
in Kelvin?';
Tinf = input(Prompt2);

%Quasi-steady classical theory - independent of initial droplet diameter
%kf = 0.0772; %thermal conductivity of nitromethane vapor in W/mK from
Chowdhury 2018
%Thermal conductivity correlation from Boyer and Kuo:
A = 3.135e-5;
BP = 1.1119;
C = -91.6;
DP = 1.28e5;
kf = (A*Tinf^BP)/(1+(C/Tinf)+(DP/Tinf^2)); %thermal conductivity of gas phase
NM from Boyer and Kuo
%kf = 0.0772; %W/mK
ka = 0.0756; %thermal conductivity of air from Turns in W/mK - not used here
though.

k_pcg = ks(p);
kg = 0.4*kf + 0.6*k_pcg; %W/mK

%NM vapor specific values
hfg = 33.99e3; %J/mol for NM vapor taken from Chowdhury 2018 at standard
conditions
rho_l = 1140; %NM - kg/m3 at standard conditions
delta_hc = 709.188e3; %J/mol for NM
nu = 1.69; %From chowdhury 2018
Cpg = 1920.73; %J/kgK of nitromethane vapor assumed to be eual to CPF and
taken from Chowdhury 2018

%Transfer number
B = ((delta_hc/nu) + Cpg*(Tinf-Ts))/hfg;
k_turns = (((8*kg)/(rho_l*Cpg))*log(1+B))*10^6; %Classical theory from Turns
result

%For droplet in convective environment, improved prediction form
%incorporating effects from natural convection from film theory
%(turns) %pcg = post combustion gases
rho_pcg = rhos(p);
U_pcg = Us(p);
```

```matlab
mu_pcg = mus(p);
Cp_pcg = Cps(p);
O2_calc = O2concs(p);

%For droplet in convective environment, improved prediction form
%incorporating Grashoff number

g = 9.8; %m2/s (gravitational acceleration)
Tad = 2540; %K
Tfl =  0.75*Tad; %K %Similar to aggarwal (1905 K)
Tavg = 0.5*(Tfl + Tad); %K
Bee = 1/Tavg; %K^-1
vg = mus(p)/rhos(p);

GrD = (g*Bee*(Tfl - Tinf)/vg^2).*(D.^3);

for i = 1: numel(D)
    Re_pcg(i) = ((rho_pcg*U_pcg)*D(i))/mu_pcg;
    %Pr_pcg = Cp_pcg*mu_pcg/k_pcg;
    Pr_pcg = Prs(p);
    %Calculating nusselt number;
    nu1(i) = 0.555*(Pr_pcg^(1/3))*((Re_pcg(i))^0.5);
    nu2(i) = (Pr_pcg^(4/3))*Re_pcg(i);
    NU_D(i) = 2 + (nu1(i)/(1 + (1.232/nu2(i)))^0.5);
    k_NU(i) = (((4*kg*NU_D(i))/(rho_l*Cpg))*log(1+B))*10^6;
    k_qs(i) = k_turns;
    k_gr(i) = 0.338*D(i)*10^3+1.272;
    DEE(i) = k_gr(i)/k_qs(i);
    M_qs(i) = (4*pi*(kg/Cpg)*(D(i)/2)*log(1+B))*1000; %g/s
    M_NU(i) = (2*pi*(kg/Cpg)*(D(i)/2)*NU_D(i)*log(1+B))*1000;
end

figure(1)
plot(D.*(10^3),k_NU,'b-.')
hold on
plot(D.*(10^3),k_qs,'r-.')
plot(D.*(10^3),k_gr,'g-.')
plot(ExD,ExK,'ko')
xlim([0 2])
ylim([0 3])
xlabel('Droplet diameter (mm)')
ylabel('Burning rate constant (mm^2/s)')
title(['Theoretical Burning Rate Constants for NM, T = ~',num2str(Tinf),'K,
X_O_2 (CEA) ~',num2str(O2_calc)]);
legend('K - film theory (conv. effects)','K - Quasi-steady','K -
Experimental','Location','SouthEast');

figure(2)
plot(D.*(10^3),M_qs,'b')
hold on
plot(D.*(10^3),M_NU,'r')
plot(dDATS,MDATS,'om')
xlabel('Droplet Diameter (mm)')
ylabel('Mass burning rate (g/s)')
```

```matlab
clear all, close all, clc
```

```
%D2 law theory comparison of IPN droplet combustion data
%k_expt (experimental burning rate constant) is obtained from the linear
%graph of (DS/DO)^2 vs Time (s)
%This comparison calculates the predicted burning rate constant and burning
%rate from quasi-steady droplet combustion theory
%As per Chowdhury et al (2018), properties of the liquid fuel, fuel vapor
%and surrounding atmosphere are simplified by evaluating them at an average
%temperature between flame temperature and boiling point of IPN
%Gas properties were obtained from CEA calculations

% %Experimental Data
% ExData = load('expdata_2inch_p51_NM.txt');
% ExD = ExData(:,1);
% ExK = ExData(:,2);

DATS = load('IPN_exptl_data.txt');
dDATS = DATS(:,1).*10; %experimental diameter in mm
MDATS = DATS(:,2); %Experimental mass burning rate in g/s

%Theory
D = (0.30:0.005:1.8)*10^-3; %series of droplet diameters ranging between
0.3mm and 1.8mm

%Loading conditions data info from CEA calculations. Filename
= %cond_props.dat
Conds = load('cond_props.dat');
O2concs = Conds(:,1).*0.01; %Mole fraction
Tads = Conds(:,2);%K
mus = Conds(:,3);%Pa.s
ks = Conds(:,4);%W/mK
Cps = Conds(:,5);%J/kgK
rhos = Conds(:,6);%kg/m3
Prs = Conds(:,7);
Us = Conds(:,8);%m/s

%Prompt1 = 'What condition are you running (1-14)?';
%p = input(Prompt1);
p = 7;
%Temperatures
Ts = 373.7; %K, boiling point of NM
Prompt2 = 'What is the measured ambient temperature surrounding the droplet
in Kelvin?';
Tinf = input(Prompt2);

%Quasi-steady classical theory - independent of initial droplet diameter
%kf = 0.0772; %thermal conductivity of nitromethane vapor in W/mK from
Chowdhury 2018
%Thermal conductivity correlation from Boyer and Kuo:
A = 3.135e-5;
BP = 1.1119;
C = -91.6;
DP = 1.28e5;
kf = 0.0592; %W/mK
ka = 0.0756; %thermal conductivity of air from Turns in W/mK - not used here
though.

k_pcg = ks(p);
```

```matlab
kg = 0.4*kf + 0.6*k_pcg; %W/mK

%NM vapor specific values
hfg = 38.79e3; %J/mol for IPN
rho_l = 1140; %NM - kg/m3 at standard conditions
delta_hc = 1950.9e3; %J/mol for IPN heat of combustion
nu = 4.25; %From chowdhury 2018
Cpg = 2349; %J/kgK of IPN

%Transfer number
B = ((delta_hc/nu) + Cpg*(Tinf-Ts))/hfg;
k_turns = (((8*kg)/(rho_l*Cpg))*log(1+B))*10^6; %Classical theory from Turns
result

%For droplet in convective environment, improved prediction form
%incorporating effects from natural convection from film theory
%(turns) %pcg = post combustion gases
rho_pcg = rhos(p);
U_pcg = Us(p);
mu_pcg = mus(p);
Cp_pcg = Cps(p);
O2_calc = O2concs(p);

%For droplet in convective environment, improved prediction form
%incorporating Grashoff number

g = 9.8; %m2/s (gravitational acceleration)
Tad = 1600; %K
Tfl =  0.75*Tad; %K %Similar to aggarwal (1905 K)
Tavg = 0.5*(Tfl + Tad); %K
Bee = 1/Tavg; %K^-1
vg = mus(p)/rhos(p);

GrD = (g*Bee*(Tfl - Tinf)/vg^2).*(D.^3);

for i = 1: numel(D)
    Re_pcg(i) = ((rho_pcg*U_pcg)*D(i))/mu_pcg;
    %Pr_pcg = Cp_pcg*mu_pcg/k_pcg;
    Pr_pcg = Prs(p);
    %Calculating nusselt number;
    nu1(i) = 0.555*(Pr_pcg^(1/3))*((Re_pcg(i))^0.5);
    nu2(i) = (Pr_pcg^(4/3))*Re_pcg(i);
    NU_D(i) = 2 + (nu1(i)/(1 + (1.232/nu2(i)))^0.5);
    k_NU(i) = (((4*kg*NU_D(i))/(rho_l*Cpg))*log(1+B))*10^6;
    k_qs(i) = k_turns;
    k_gr(i) = 0.338*D(i)*10^3+1.272;
    DEE(i) = k_gr(i)/k_qs(i);
    M_qs(i) = (4*pi*(kg/Cpg)*(D(i)/2)*log(1+B))*1000; %g/s
    M_NU(i) = (2*pi*(kg/Cpg)*(D(i)/2)*NU_D(i)*log(1+B))*1000;
end

% figure(1)
% plot(D.*(10^3),k_NU,'b-.')
% hold on
% plot(D.*(10^3),k_qs,'r-.')
% plot(D.*(10^3),k_gr,'g-.')
% plot(ExD,ExK,'ko')
```

```matlab
% %xlim([0 2])
% %ylim([0 3])
% xlabel('Droplet diameter (mm)')
% ylabel('Burning rate constant (mm^2/s)')
% title(['Theoretical Burning Rate Constants for NM, T = ~',num2str(Tinf),'K,
X_O_2 (CEA) ~',num2str(O2_calc)]);
% legend('K - film theory (conv. effects)','K - Quasi-steady','K -
Experimental','Location','SouthEast');

figure(1)
plot(D.*(10^3),M_qs,'b')
hold on
plot(D.*(10^3),M_NU,'r')
plot(dDATS,MDATS,'om')
xlabel('Droplet Diameter (mm)')
ylabel('Mass burning rate (g/s)')
```

APPENDIX F: TEST PROCEDURES

Aerospace Sciences Laboratory and Applied Laser Spectroscopy Laboratory			
Location: MSEE 345 Plasma Lab			
Monopropellant Test Procedures			
Written by: Angela Mbugua			
Test Requirements: Tests will be performed with minimum two students authorized to work by Dr. Sally Bane must be present for all tests; all safety equipment must be present before tests begin. Extraneous personnel should be cleared of lab/control room areas prior to running a test sequence.			
SECTION 0: EMERGENCY			
IN CASE OF LEAK, FIRE, OR OTHER INCIDENT			
0.000	TC1, TC2		Test conductors will use their best judgment to determine the severity of the situation
0.001	TC1, TC2		In case of observable flashback, HIT ABORT BUTTON ON VI to automatically CLOSE PV-CH4-01, CLOSE PV-O2-01 and OPEN PV-N2-01
0.002	TC1, TC2		Regardless of the incident severity, the appropriate personnel will be notified by phone of the incident and will provide guidance for further action. Sally Bane: 765-414-1357 (Cell phone)
ITEMS NEEDED			
0.003	TC1, TC2		Labcoats, safety glasses, face shield, nitrile gloves, paper towels, plastic pipette, small fuel vial, small beaker with DI water in it
1. CAMERA SETUP and DELAY GENERATOR TESTING (THE DAY BEFORE TESTING)			
1.067	TC1, TC2		Gather SA4, SAZ, Intensifier, K2 lens, UV lens, dummy adapter, and filter adapter, including all appropriate cables from wherever they are (Zucrow, ASL e.t.c)
1.068	TC1, TC2		Mount them in their appropriate positions orthogonal to the burner
PHOTRON SA4			
1.069	TC1, TC2		Ensure all camera wiring is done and K2 lens is mounted properly
1.070	TC1, TC2		Mount Green LEDs in place on the opposite side of the burner
1.071	TC1, TC2		Ensure lens cap is on the K2
1.072	TC1, TC2		Turn on the photron camera
1.073	TC1, TC2		Start up PFV software and ensure camera is detected
1.074			Set frame rate to 3600 fps for focusing and testing, and the resolution to 1024 X 1023
1.075	TC1, TC2		Go to 'Camera Option', Go to 'I/O' and set 'General In' to 'TRIG POS' to trigger camera externally
1.076	TC1, TC2		Take a CSR (Hit 'shading' on the PFV software)
1.077	TC1, TC2		Take the lens cap off
1.078	TC1, TC2		Turn on the LED
1.079			If field of view is not well lit, open aperture to desired level
1.080	TC1, TC2		Place the calibration dot card in the center of the burner
1.081	TC1, TC2		Focus on the calibration card using lens and aperture

1.082	TC1, TC2		Calibrate the field of view with known distance and record/take a snap shot for later use in post-processing code
1.083	TC1, TC2		Turn off the LED and put the lens cap back on
1.084	TC1, TC2		Exit the software and turn off the photron until continued test setup tomorrow

PHOTRON SAZ AND IRO

This section is divided into two parts: 1. Focusing the intensifier onto the camera, 2. Getting the center of the burner in focus with and without OH filter

Focusing Camera onto IRO (Lens cap always on for this)

1.027	TC1, TC2		Ensure all wiring is done according to Camera and intensifier wiring on the next sheet (Cam and Intensifier wiring)
1.028	TC1, TC2		Replace coupling on SAZ to be used with the intensifier
1.029	TC1, TC2		On the rail, mount both the SAZ and intensifier together, ensuring they couple together at the interface properly
1.030	TC1, TC2		Take out the intensifier cap and put the UV lens fitted with the dummy adapter onto the intensifier, ensuring lens cap remains on throughout this initial focusing
1.031	TC1, TC2		Once you are satisfied with the mounting, turn on IRO controller and ensure minimum settings are on the screen (Delay: 5ns, Gate: 100ns, Gain: 0% and mode: Off)
1.032	TC1, TC2		Turn on the SAZ
1.033	TC1, TC2		Open PFV camera software
1.034	TC1, TC2		Go to 'Camera Option', Go to 'Additional Features 2' and turn the SAZ fan on to prevent overheating, and 'Additional Features 1' to make sure the 12 bit option is selected
1.035	TC1, TC2		On the toolbar at the top of the screen, go to 'Option' -> 'Configuration' -> 'Data'. Then change image level bit depth to 'Real bit' if it is on '8 bit'. Hit 'Apply', and 'OK'.
1.036	TC1, TC2		On the menu under Live mode, got to 'Camera Option', 'I/O', set GEN OUT 1 to EXPOSE POS, and GEN OUT 2 to RECORD POS, and GENERAL IN to TRIG POS
1.037	TC1, TC2		Change frame rate to 60 fps for focusing camera onto intensifier
1.038	TC1, TC2		Click 'Shading' to recalibrate
1.039	TC1, TC2		Click 'BitShift' on the top icon toolbar, and change it to '4'.
1.040	TC1, TC2		On the IRO controller, change the mode to 'internal'
1.041	TC1, TC2		Unplug disable BNC (from GEN OUT 2 on SAZ)
1.042	TC1, TC2		Turn the gate up to 50 microseconds (50,000 ns) on the controller
1.043	TC1, TC2		Start coming up in the gain on the controller setting at 10% and continue to 70% - Somewhere in between you should see noise in form of dots that seems out of focus
1.044	TC1, TC2		Once you see the dots, push camera into intensifier and play around with intensifier focus ring until the dots are in focus
1.045	TC1, TC2		Once the dots are sufficiently in focus, secure the camera and intensifier down and throughout the experiment, the coupling should not be moved at all, but can be translated together during focusing on an object
1.046	TC1, TC2		Turn the gain back down to 0% and the gate back down to minimum (100 ns) - do this whenever the intensifier is not in use
1.047	TC1, TC2		Set the mode to 'off' until ready to run the intensifier again
1.048	TC1, TC2		Replace the disable BNC cable for now

Focusing Camera onto image

1.049	TC1, TC2		Place a card using a clamp at the center of the burner to focus on this particular plane. For this particular experiment, a good focus is when the lens is at full zoom, aperture is between 56 and 8, and the lens front is apprimately 1' 1.5" away from the center of the burner
1.050	TC1, TC2		Turn off the lights
1.051	TC1, TC2		Take out the disable BNC cable to enable the intensifier to run continuously while you focus
1.052	TC1, TC2		Keep the Photron at 60 fps and max exposure (1/1000 s or 1 ms)
1.053	TC1, TC2		Ensure the UV lens aperture is all the way open (number 4)

1.054	TC1, TC2		Take off lens cap and change the mode to internal
1.055	TC1, TC2		On the controller (only for this experiment), start at a gate of 150,000 ns (150 microseconds)
1.056	TC1, TC2		Raise the gain to 30%
1.057	TC1, TC2		Shine a light on the card and see if the camera is well focused
1.058	TC1, TC2		If not, raise the gain at that gate to ~40-50%. At this point, the card should be well focused.
1.059	TC1, TC2		Once the camera is well focused, turn the gain back down to 0%, the gate down to minimum (100 ns)
1.060	TC1, TC2		Put the lens cap back on
1.061	TC1, TC2		Put the disable BNC back into place
1.062	TC1, TC2		Turn the mode to 'off' for now
1.063	TC1, TC2		Turn off the controller for now and turn the lights on
1.064	TC1, TC2		Switch lens adapters to that with the OH filter
Triggering both cameras with the delay generator (UV lens cap remains on)			
1.065	TC1, TC2		Switch on the delay generator and Recall ANGIE3M settings
1.066	TC1, TC2		Ensure that these settings are correct on all correct channels (see settings section)
1.085	TC1, TC2		Ensure correct BNC cables are plugged into the correct channels on the delay generator
1.086	TC1, TC2		Turn the delay generator on
1.087	TC1, TC2		Turn on the SA4 (lens cap on K2 can also remain on)
1.088	TC1, TC2		Open PFV software for the SA4 laptop - so you should have two laptops open to the PFV software (one for SAZ and one for SA4)
1.089	TC1, TC2		Turn the mode on the controller to 'disable' - this ensures that the intensifier only runs when the SAZ is in recording mode
1.090	TC1, TC2		Set both cameras to wait for trigger on the PFV software
1.091	TC1, TC2		Ensure that both cameras have been set to 3600 fps and random reset (10,000 frames)
1.092	TC1, TC2		Trigger both cameras using the delay generator - ensure that both cameras have been indeed triggered
1.093	TC1, TC2		Set 'Triggered' on the delay generator and trigger both cameras again via Labview
1.094	TC1, TC2		Once satisfied with the triggering, ensure IRO controller is set to all minimum settings (5ns delay, 100ns gate, 0% gain)
1.095	TC1, TC2		Turn off the controller
1.096	TC1, TC2		Exit the PFV software
1.097	TC1, TC2		Turn off the SAZ
1.098	TC1, TC2		Turn off the SA4
1.099	TC1, TC2		Make sure the correct settings are saved on the delay generator and turn it off
1.100	TC1, TC2		Replace the adapter on the IRO with the OH filter adapter and secure in place - leave the UV lens cap on
2. OVERALL TEST SETUP (DAY OF TESTING)			
2.000	TC1, TC2		Ensure that the experiment is assembled correctly - all O2, N2, AR, CH4 and water lines are assembled correctly and tightened
2.001	TC1, TC2		Ensure the NI USB cable and the ethernet cable connected to the computer
2.003	TC1, TC2		OPEN the monopropellants VI
2.004	TC1, TC2		Disable all the valves, and turn off the flowmeters (the icons should change from green to black)
2.002	TC1, TC2		Turn on DAQ box knob and power strip to turn on DAQ
2.005	TC1, TC2		Start VI and ensure temperature readings are correct (the O2 valve will click because it is open by default, and is closing upon starting the VI - this is normal!)
2.003	TC1, TC2		Ensure that the manual valve to the pneumatic cylinder is initially closed
2.006	TC1, TC2		Ensure that MR-AIR-01 on the bottle is unloaded all the way
2.004	TC1, TC2		Open the air bottle all the way and then close 1/2 a turn
2.007	TC1, TC2		Load MR-AIR-01 on the air bottle to 80 psi for valve and pneumatic cylinder operation (the valves should now be pressurized)

2.005	TC1, TC2		Valve check PV-O2-01, PV-N2-01, PV-CH4-01 and PV-N2-02 and ensure all valves are CLOSED
2.008	TC1, TC2		Put on the power supply for the pneumatic cylinder and ensure the default position of the cylinder is withdrawn
2.006	TC1, TC2		Fill the water bucket with water and place the water pump in the bucket without turning the pump on
2.009	TC1, TC2		Ensure water-out line goes back into the bucket
2.007	TC1, TC2		Place a small beaker with DI water in the fumehood for fuel dilution after test completion
3. PRE-TEST PROCEDURES			
2.001	TC1, TC2		Put on PPE (lab coat, safety glasses and nitrile gloves)
2.002	TC1, TC2		Ensure that MR-AR-01 on the ox nitrogen bottle is unloaded all the way and the needle valve NV-N2-01 is fully open
2.002	TC1, TC2		Open the Argon bottle all the way and close 1/2 turn
2.003	TC1, TC2		Load MR-AR-01 to 50 psi
2.004	TC1, TC2		Ensure that MR-O2-01 on the oxygen bottle is unloaded all the way and the needle valve NV-O2-01 is fully open
2.005	TC1, TC2		Open the O2 bottle all the way and close 1/2 turn
2.006	TC1, TC2		Load MR-O2-01 to 50 psi for O2 synthetic air flow
2.007	TC1, TC2		Open the N2 shroud gas bottle all the way and close 1/2 turn
2.008	TC1, TC2		Load MR-N2-02 to 50 psi for N2 shroud gas flow
2.009	TC1, TC2		Ensure that MR-CH4-01 on the fuel bottle is unloaded all the way and the needle valve NV-CH4-01 is fully open
2.010	TC1, TC2		Open the CH4 bottle all the way and close 1/2 turn
2.011	TC1, TC2		Load MR-CH4-01 to 50 psi for CH4 fuel flow
2.012	TC1, TC2		Ensure that the ceramic flame shield is out of the way (pnuematic cylinder in withdrawn position - energized position)
2.013	TC1, TC2		Turn on the water pump and ensure set the water ensure water is steadily flowing into and out of the burner (this may take a minute to stabilize)
Camera Preparation			
2.014	TC1, TC2		Turn on the SA4
2.015	TC1, TC2		Open the PFV software for the SA4 camera
2.016	TC1, TC2		Set the frame rate to 3600 fps and resolution to 1024 X 1024, General In to Trig POS, and trigger mode to Random Reset 10,000
2.017	TC1, TC2		Hit 'Shading' to calibrate the field of view
2.018	TC1, TC2		Leave the lens cap on and don't turn on the GREEN LED yet until ready to test
2.019	TC1, TC2		Turn on the IRO controller
2.020	TC1, TC2		Ensure minimum settings (5ns delay, 100ns gate, 0% gain)
2.021	TC1, TC2		Turn on the SAZ
2.022	TC1, TC2		Open PFV software for SAZ laptop
2.023	TC1, TC2		Ensure the necessary settings (fan on, Gen out1, Gen out2, General In, Realbit and Bitshift, and trigger mode random reset depending on first test
2.024	TC1, TC2		Ensure disable BNC is connected
2.025	TC1, TC2		Change mode to 'internal' and leave the lens cap on
Fuel Loading			
2.030	TC1, TC2		With gloves on, transfer fuel bottle (NM, IPN or methanol) to the fumehood (if not already in the fumehood)
2.031	TC1, TC2		With gloves on, load liquid fuel (NM, IPN, or methanol) inside the fumehood into small vial using a plastic pipette and place inside fumehood with paper towel on the side in case of spills
2.032	TC1, TC2		Using the vial, load microliters of the liquid fuel into the syringe inside the fumehood
2.033	TC1, TC2		Place the syringe on the paper towel while you close the open vial inside the fumehood
2.034	TC1, TC2		Transfer the microliter syringe to the setup on the optics table and mount it in place ready for testing
3. TESTING			

3.001	TC1, TC2		Set the condition flowrates on AR and O2 and then close the valves
3.002	TC1, TC2		Open manual valve to pressurize air cylinder - leave it in default position over the burner
3.003	TC1, TC2		Turn on the Green LED
3.004	TC1, TC2		Turn off the lights
3.005	TC1, TC2		Take lens cap off the K2 lens on the SA4
3.006	TC1, TC2		Take the lens cap off the UV lens on the IRO/SAZ system
3.007	TC1, TC2		On the IRO controller, set the gate to 100 microseconds
3.008	TC1, TC2		Set the gain to 45 - 60% depending on fuel (see settings 1, 2, 3, 4, or 5 on IRO controller)
3.009	TC1, TC2		Ensure both cameras are waiting for a trigger
3.010	TC1, TC2		OPEN PV-AR-01, PV-O2-01, PV-CH4-01, and turn on CH4 mass flow controller
3.011	TC1, TC2		Ensure AR and O2 flowrates are correct, set N2 shroud gas flow rate
3.012	TC1, TC2		Set CH4 flowrate on the VI and ensure it reads correctly on the massflowmeter display screen
3.013	TC1, TC2		Produce a droplet using linear actuator and place it on the silica fiber
3.014	TC1, TC2		light the burner
3.015	TC1, TC2		Hit 'IGNITE' on the VI to remove the flame shield and trigger both cameras
3.016	TC1, TC2		Once droplet disappears (after ~2-4s), close PV-CH4-01 and PV-02-01 - flame will blow off
3.017	TC1, TC2		Shut off shroud gas
3.018	TC1, TC2		Close PV-AR-01
3.019	TC1, TC2		Turn gain down to 0% and gate down to minimum (100ns) - Settings 2 on controller
3.020	TC1, TC2		Put lens cap back on
3.021	TC1, TC2		Save both files
3.022	TC1, TC2		For additional tests, repeat 3.007-3.021
3.023	TC1, TC2		When done with tests, proceed to section 4
3.024	TC1, TC2		If syringe runs out of fuel before testing, transport microliter syringe to the fumehood and repeat steps 2.032 to 2.034
4. SHUTDOWN AND CLEANUP			
4.000	TC1, TC2		Ensure that all data has been saved properly
4.001	TC1, TC2		Ensure settings on the IRO are minimum, and the lens cap on the UV lens is on
4.002	TC1, TC2		Turn the mode to 'off' for now
4.003	TC1, TC2		Turn on the lights
4.004	TC1, TC2		Turn off the IRO controller
4.005	TC1, TC2		If all files are saved, exit the PFV software on the SAZ computer
4.006	TC1, TC2		Turn off the SAZ
4.007	TC1, TC2		Put the lens cap on the K2
4.008	TC1, TC2		Exit the PFV software on the SA4 laptop
4.009	TC1, TC2		Turn the photron off
4.010	TC1, TC2		CLOSE the O2, CH4, AR and N2 shroud gas bottles and ensure that they are tightly closed (do not close AIR bottle)
4.011	TC1, TC2		Set mass flow rate on CH4 flowmeter on VI for depressurizing
4.012	TC1, TC2		OPEN PV-CH4-01 and de-pressurize the line (You don't have to unload regulator unless you are not testing the next day)
4.013			CLOSE PV-CH4-01
4.014	TC1, TC2		Set mass flow rate on O2 flowmeter FM-O2-01 on VI for depressurizing
4.015	TC1, TC2		OPEN PV-O2-01 and de-pressurize the line
4.016			CLOSE PV-O2-01
4.017	TC1, TC3		Set the desired flowrate on FM-AR-01 and depressurize the line
4.018	TC1, TC2		CLOSE PV-AR-01
4.019	TC1,TC2		OPEN N2 shroud flowmeter until shroud as line is depressurized
4.020	TC1, TC2		CLOSE AIR bottle
4.021	TC1, TC2		CYCLE PV-O2-01 several times until pneumatic lines are depressurized
4.022	TC1, TC2		Ensure flame shield is depressurized and is away from burner surface

| 4.023	TC1, TC2		STOP the VI and exit LabView
4.024	TC1, TC2		Turn off the DAQ and switch off the DAQ power strip
4.025	TC1, TC2		Turn off the delay generator
4.026	TC1, TC2		Turn off the pneumatic cylinder valve power supply
4.027	TC1, TC2		If not testing again in the next two days, disconnect all cables, disassemble all connections and put lens, cables and cameras back into their cases
PROPELLANTS SHUTDOWN			
4.028	TC1, TC2		If there is fuel in the fuel syringe, transport the microliter syringe to the fumehood and unload the syringe into the water beaker to dilute it at the corner of the fumehood and leave for later disposal
4.029	TC1, TC2		Wipe the syringe with a paper towel and set aside on the corner for rinsing later - leave the syringe inside the fumehood
4.030			If the small vial still has fuel inside of it, ensure that it closed, labeled and left inside the fumehood for later storing
Later disposal			
4.031	TC1, TC2		Ensure you are wearing proper PPE - nitrile gloves, safety goggles, facemask and labcoat
4.032	TC1, TC2		Load a second beaker with DI water and transport to fumehood
4.033	TC1, TC2		Load microliter syringe multiple times in the beaker and unload to the paper towel to rinse out the syringe for next testing day
4.034	TC1, TC2		Leave the syringe to dry inside the fumehood on a paper towel
4.035	TC1, TC2		If the small vial has too little fuel to be used for the next tests, do not refill with fuel still inside, pour remaining NM into the new DI water beaker that was used to rinse syringe and leave the vial inside the beaker
4.036	TC1, TC2		Transport the WATER+NM beaker and vial to the sink near the optics table and open the water drain while pouring out the NM simultaneously
4.037	TC1, TC2		Rinse the beaker and small vial thoroughly and return to the fumehood on the paper towel next to the syringe
SETTINGS - Delay Generator			
External Trigger			Ensure external trigger from the DAQ is plugged into the external trigger channel on the delay generator
Ch C	Cylinder		Width:10 s; Delay:0s, Out: Adjustable; Pol: Active High; Ampl: 5.00V; Mode: Single Shot; Wait: 0 plses
Ch D	SA4		Width:20 µs; Delay:0s, Out: Adjustable; Pol: Active High; Ampl: 5.00V; Mode: Single Shot; Wait: 0 plses
Ch A	SAZ		Width:20 µs; Delay:0s, Out: Adjustable; Pol: Active High; Ampl: 5.00V; Mode: Single Shot; Wait: 0 plses
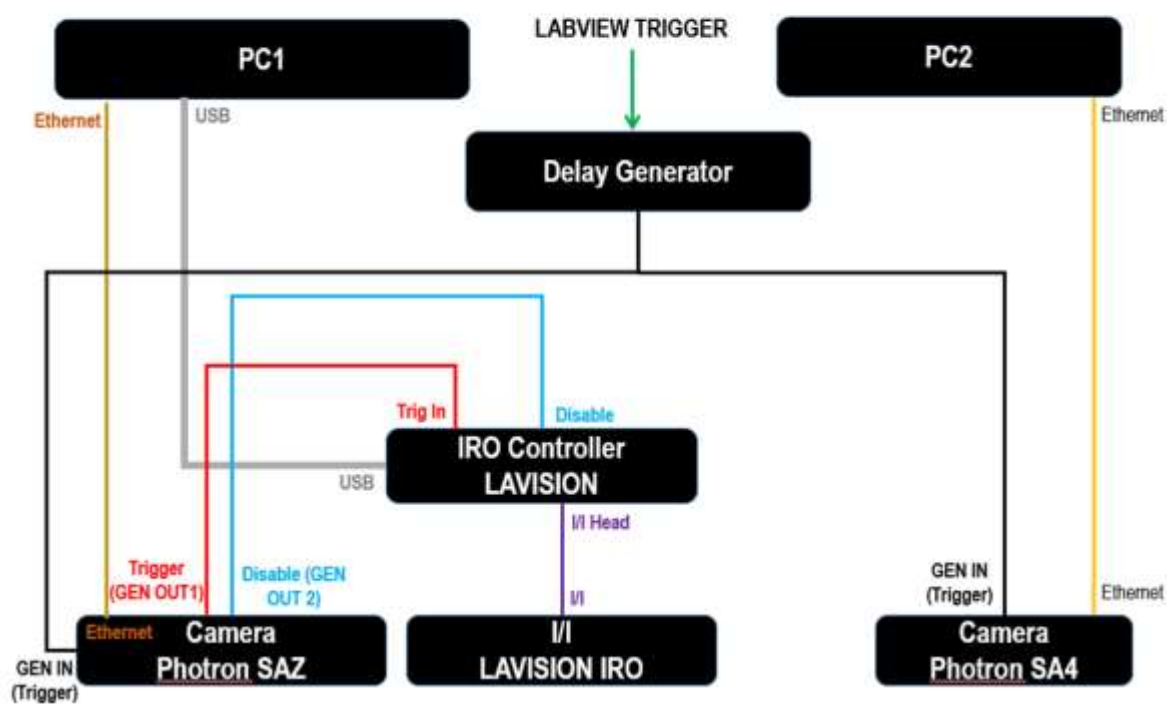
Figure 74. Camera wiring diagram referred to in test procedures

REFERENCES

[1] C. B. Allison, "Hybrid and Decomposition Combustion of the Hydrazine Fuels," The Pennsylvania State University.

[2] A. Ambekar, A. Chowdhury, S. Challa, and D. Radhakrishna, "Droplet combustion studies of hydrocarbon-monopropellant blends," *Fuel*, vol. 115, pp. 697–705, 2014.

[3] E. Boyer and K. K. Kuo, "Characteristics of Nitromethane for Propulsion Applications," in *44th AIAA Aerospace Sciences Meeting and Exhibit*, 2006, no. January.

[4] L. B. Zung, E. A. Tkachencko, and B. P. Breen, "A Basic Study on the Ignition of Hypergolic Liquid Propellants," *NASA Interim Rep. NAS 7-438*, 1962.

[5] J. J. Sangiovanni and A. S. Kesten, "A Theoretical and Experimental Investigation of the Ignition of Fuel Droplets," *Combust. Sci. Technol.*, 1977.

[6] G. M. Faeth and D. R. Olson, "The Ignition of Hydrocarbon Fuel Droplets in Air," *SAE Tech. Pap. 680465*, 1968.

[7] G. M. Faeth, "The Kinetics of Droplet Ignition in a Quiescent Air Environment," The Pennsylvania State University, 1964.

[8] N. A. Chigier and C. G. McCreath, "Combustion of Droplets in Sprays," *Acta Astronaut.*, vol. 1, no. 5–6, pp. 687–710, 1974.

[9] H. H. Chiu, "Advances and challenges in droplet and spray combustion. I. Toward a unified theory of droplet aerothermochemistry," *Prog. Energy Combust. Sci.*, vol. 26, pp. 381–416, 2000.

[10] S. R. Turns, *An Introduction to Combustion - Concepts and Applications*, 2nd ed. McGraw-Hill Education, 1999.

[11] C. M. Verwey, "An Experimental Investigation of the Effect of Fuel Droplet Size on the Vaporization Process in a Turbulent Environment at Elevated Temeprature and Pressure," The University of Manitoba, 2017.

[12] S. Rah, A. F. Sarofim, and J. M. Beër, "Ignition and Combustion of Liquid Fuel Droplets Part II: Ignition Studies," *Combust. Sci. Technol.*, vol. 49, pp. 169–184, 1986.

[13] C. A. Bergeron and W. L. H. Hallett, "Ignition Characteristics of Liquid Hydrocarbon Fuels as Single Droplets," *Can. J. Chem. Eng.*, vol. 67, pp. 142–149, 1989.

[14] S. K. Aggarwal, "Single droplet ignition: Theoretical analyses and experimental findings," *Prog. Energy Combust. Sci.*, vol. 45, pp. 79–107, 2014.

[15] C. K. Law, "Theory of Thermal Ignition in Fuel Droplet Burning," *Combust. Flame*, vol. 31, pp. 285–296, 1978.

[16] K. Annamalai and W. Ryan, "Interactive Processes in Gasification and Combustion. Part I : Liquid Drop Arrays and Clouds," *Prog. Energy Combust. Sci.*, vol. 18, pp. 221–295, 1992.

[17] E. A. Hurlbert, R. J. Moreland, and S. Candel, "Propellant Ignition and Flame Propagation," in *Liquid Rocket Thrust Chambers: Aspects of Modeling, Analysis and Design*, P. Z. V. Yang, M. Habiballah, J. Hulka, M. Popp, Ed. Reston, VA: Progess in Aeronautics and Astronautics, AIAA, 2004, pp. 405–436.

[18] E. M. Dambach, "Ignition of Hypergolic Propellants," Purdue University, 2010.

[19] T. D. Kubal, S. F. Son, W. E. Anderson, and T. L. Pourpoint, "Aspects of Monomethyl hydrazine and Red Fuming Nitric Acid Ignition," in *AIAA/SAE/ASME/ASEE Joint Propulsion Conference, Nashville, TN*, 2010.

[20] M. D. James, "Liquid and Gelled Sprays for Mixing Hypergolic Propellants using an Impinging Jet System," Purdue University, 2010.

[21] J. M. Forness, "Phenomena Resulting from Hypergolic Contact," Purdue University, 2013.

[22] C. K. Law, "Theory of thermal ignition in fuel droplet burning," *Combust. Flame*, vol. 31, pp. 285–296, 1978.

[23] M. Takei, T. Tsukamoto, and T. Niioka, "Ignition of Blended-Fuel Droplet in High-Temperature Atmosphere," *Combust. Flame*, vol. 93, pp. 149–156, 1993.

[24] M. Mawid and S. K. Aggarwal, "Chemical Kinetics Effects on the Ignition of a Fuel Droplet," *Combust. Sci. Technol.*, vol. 65, no. 1–3, pp. 137–150, 1989.

[25] B. J. Wood and W. A. Rosser Jr, "An Experimental Study of Fuel Droplet Ignition," *AIAA J.*, vol. 7, no. 12, pp. 2288–2292, 1969.

[26] A. M. Kanury, *Introduction to Combustion Phenomena: (for fire, incineration, pollution and energy applications)*. New York: Gordon and Breach, c1975.

[27] I. Awasthi, G. Gogos, and T. Sundararajan, "Effects of Size on Combustion of Isolated Methanol Droplets," *Combust. Flame*, vol. 160, pp. 1789–1802, 2013.

[28] G. A. Longt and E. A. Grens II, "Self-ignition behavior of fuel droplets in hot stagnant gases," *Chem. Eng. Schience*, vol. 25, pp. 623–631, 1970.

[29] C. A. Gregory Jr and H. F. Calcote, "Combustion Studies of Droplet-Vapor Systems," *Fourth Internaltional Symp. Combust.*, pp. 830–837, 1953.

[30] E. M. Goodger and A. F. M. Eissa, "Spontaneous Ignition Research: Review of Experimental Data," *J. Inst. Energy*, vol. 60, pp. 84–94, 1987.

[31] N. Nishiwaki, "Kinetics of Liquid Combustion Processes: Evaporation and Ignition Lag of Fuel Droplets," *Proc. Combust. Inst*, vol. 5, pp. 148–158, 1955.

[32] T. Saitoh, S. Ishiguro, and T. Niioka, "An Experimental Study of Droplet Ignition Characteristics Near the Ignitable Limit," *Combust. Flame*, vol. 48, pp. 27–32, 1982.

[33] M. Ogasawara, F. Fujimoto, T. Takagi, and Y. Tosa, "Ignition and Combustion of a Fine Fuel Droplet Falling Freely into a Hot Atmosphere," *Bull. JSME*, vol. 16, no. 102, pp. 1938–1946, 1973.

[34] R. Nakanishi, H. Kobayashi, S. Kato, and T. Niioka, "Ignition Experiment of a Fuel Droplet in High-Pressure High-Temperature Ambient," in *Twenty-fifth Symposium (International) on Combustion*, 1994, pp. 447–453.

[35] J. J. Sangiovanni and A. S. Kesten, "A Theoretical and Experimental Investigation of the Ignition of Fuel Droplets," *Combust. Sci. Technol.*, vol. 16, pp. 59–70, 1977.

[36] A. Makino and H. Fukada, "Ignition and Combustion of a Falling, Single Sodium Droplet," *Proc. Combust. Inst.*, vol. 30, no. 2, pp. 2047–2054, 2005.

[37] M. T. Monaghan, R. G. Siddall, and M. W. Thring, "The Influence of Initial Diameter on the Combustion of Single Drops of Liquid Fuel," *Combust. Flame*, vol. 12, pp. 45–53, 1968.

[38] H. Hara and S. Kumagai, "The effect of initial diameter on free droplet combustion with spherical flame," *Twenty-fifth Symp. Combust.*, vol. 25, no. 1, pp. 423–430, 1994.

[39] C. H. Wang, K. H. Shy, and L. C. Lieu, "An Experimental Investigation on the Ignition Delay of Fuel Droplets," *Combust. Sci. Technol.*, vol. 118, no. 1–3, pp. 63–78, 1996.

[40] T. Kadota, H. Hiroyasu, and H. Oya, "Spontaneous Ignition Delay of a Fuel Droplet in High Pressure and High Temperature Gaseous Environments," *Bull. JSME*, vol. 19, no. 30, pp. 437–445, 1976.

[41] B. J. Wood and W. A. Rosser Jr, "An Experimental Study of Fuel Droplet Ignition," *Nonlinear Partial Differ. Equations Eng. J. A. Riddell, F. R. J. Aeronaut. Sci.*, vol. 35, no. 12, pp. 101–104, 1965.

[42] B. P. Mullins, *Spontaneous Ignition of Liquid Fuels*. London: Butterworths Publications Ltd., 1955.

[43] J. J. Sangiovanni and A. S. Kesten, "Effect of Droplet Interaction on Ignition in Monodisperse Droplet Streams," *Symp. Combust.*, vol. 16, no. 1, pp. 577–592, 1977.

[44] W. R. Laster and K. Annamalai, "Ignition Delay of Droplet Clouds: Results from Group Combustion Theory," *Chem. Eng. Commun.*, vol. 105, no. 1, pp. 201–219, 1991.

[45] R. Subramanyam, R. Gollahalli, and T. A. Brzustowski, "Experimental Studies on the Flame Structure in the Wake of a Burning Droplet," *Symp. Combust.*, vol. 14, no. 1, pp. 1333–1344, 1973.

[46] D. A. Charvonia, "A study of the combustion and ignition delay of fuel droplets falling through the decomposition vapors of white fuming nitric acid," Purdue University, 1953.

[47] M. El-Wakil and M. Abdou, "The Self Ignition of Fuel Drops in Heated Air Streams The Self Ignition of Fuel Drops in Heated Air Streams," *SAE Tech. Pap. 620284*, 1962.

[48] S. Satcunanathan, "Spontaneous Ignition of Liquid Fuel Droplets Falling through a Hot Air Column," vol. 9, no. 3, pp. 359–362, 1970.

[49] "General Background for Spherically Symmetric Isolated Droplet Combustion." [Online]. Available: www.princeton.edu/~combust/research.

[50] V. Nayagam, "Quasi-steady Flame Standoff Ratios during Methanol Droplet Combustion in Microgravity," *Combust. Flame*, vol. 157, pp. 204–205, 2010.

[51] C. K. Law, S. H. Chung, and N. Srinivasan, "Gas-phase Quasi-steadiness and Fuel Vapor Accumulation Effects in Droplet Burning," *Combust. Flame*, vol. 38, pp. 173–198, 1980.

[52] W. A. Rosser, "The Decomposition Burning of Monopropellant Drops: Hydrazine, Nitromethane, and Ethyl Nitrate," *Prog. Rep. No. 20-305, Jet Propuls. Lab. Pasadena, Calif.*, 1957.

[53] O. W. Dykema and S. A. Greene, "An Experimental Study of RP-1, UDMH and N2H4 Single Droplet Burning in Air and in Oxygen," in *Progress in Aeronautics and Rocketry*, vol. 2, New York: Academic Press, 1960, pp. 299–324.

[54] B. R. Lawver, "Some Observations on the Combustion of N2H4 Droplets," *AIAA J.*, vol. 4, no. 4, pp. 659–662, 1966.

[55] C. B. Allison and G. M. Faeth, "Decomposition and hybrid combustion of hydrazine, MMH and UDMH as droplets in a combustion gas environment," *Combust. Flame*, vol. 19, no. 2, pp. 213–226, 1972.

[56] R. L. Peskin and H. Wise, "A Theory for Ignition and Deflagration of Fuel Drops.," *AIAA J.*, vol. 4, no. 9, pp. 1646–1650, 1966.

[57] D. R. Kassoy and F. A. Williams, "Effects of Chemical Kinetics on Near Equilibrium Combustion in Nonpremixed Systems," *Phys. Fluids*, vol. 11, no. 6, p. 1343, 1968.

[58] A. Linán, "The Asymtotic Structure of Counterflow Diffusion Flames for Large Activation Energies," *Acta Astronaut.*, vol. 1, pp. 1007–1039, 1974.

[59] C. K. Law, "Asymptotic theory for ignition and extinction in droplet burning," *Combust. Flame*, 1975.

[60] C. K. Law, *Combusiton Physics*. New York: Cambridge University Press, 2006.

[61] D. B. Spalding and V. K. Jain, "Theory of Burning of Monopropellant Droplets," *ARC Tech. Rep. C.P. No. 447*, 1958.

[62] F. A. Williams, "Combustion of Droplets of Liquid Fuels," *Combust. Flame*, vol. 21, pp. 1–31, 1973.

[63] G. A. E. Godsave, "Studies of the Combustion of Drops in a Fuel Spray - the Burning of Single Drops of Fuel," *Symp. Combust.*, vol. 4, no. 1, pp. 818–830, 1953.

[64] D. B. Spalding, "The Combustion of Liquid Fuels," *Symp. Combust.*, vol. 4, no. 1, pp. 847–864, 1953.

[65] A. J. Marchese, F. L. Dryer, V. Nayagam, and R. O. Colantonio, "Hydroxyl Radical Chemiluminescence Imaging and Structure of Microgravity Droplet Flames," *Twenty-sixth Symp. Combust. Combust. Inst.*, 1996.

[66] T. Kathrotia, M. Fikri, M. Bozkurt, M. Hartmann, U. Riedel, and C. Schulz, "Study of the H+O+M reaction forming OH*: Kinetics of OH* Chemiluminescence in Hydrogen Combustion Ssystems," *Combust. Flame*, vol. 157, 2010.

[67] A. J. Marchese, T. L. Vaughn, K. Kroenlein, and F. L. Dryer, "Ignition delay of fatty acid methyl ester fuel droplets : Microgravity experiments and detailed numerical modeling q," *Proc. Combust. Inst.*, 2010.

[68]   D. M. Fairbrother, H. A. Skinner, and F. W. Evans, "The heats of combustion of organic compounds of nitrogen. Part 1. Ethyl, n-propyl, and isopropyl nitrates," *Trans. Faraday Soc.*, vol. 53, pp. 779–783, 1957.

[69]   S. Datta, "Nitromethane Droplet Combustion: The Influence of Aluminum Particle Size as an Additive to Enhance Burning," Texas Tech University, 2008.

[70]   F. Scientific, "No Title." .

[71]   "Holthuis & Associates Flat Flame Burners." .

[72]   R. Toossi, "Physical and Chemical Properties of Combustion Generated Soot," University of California/Berkeley, 1978.

[73]   C. Brown, U. Mondragon, and V. McDonell, "Introduction to the Flat Flame Burner and its use in Combustion Diagnostics Applications." .

[74]   *Fastcam SA4 Photron Hardware Manual*. .

[75]   *Photron SAZ Fastcam Technical Datasheet*. .

[76]   R. S., J. R. Gord, and A. K. Patnaik, "Recent Advances in Coherent anti-Stokes Raman Scattering Spectroscopy: Fundamental Developments and Applications in Reacting Flows," *Prog. Energy Combust. Sci.*, vol. 36, no. 2, pp. 280–306, 2010.

[77]   H. Dong, A. Satija, K. Jupyoung, Y. W, J. P. Gore, and R. P. Lucht, "Dual-pump vibrational CARS measurements of temperature and species concentrations in turbulent premixed flames with CO2 addition," *Combust. Flame*, vol. 181, pp. 239–250, 2017.

[78]   A. Ambekar, A. K. Maurya, and A. Chowdhury, "Droplet Combustion Studies of Nitromethane and its Blends," *Exp. Therm. Fluid Sci.*, vol. 93, no. January, pp. 431–440, 2018.

[79]   J. Powling and W. A. . Smith, "Flame Decomposition of the Propyl Nitrates," *Combust. Flame*, vol. 1, no. 3, pp. 308–320, 1957.

[80]   J. Morin and Y. Bedjanian, "Thermal Decomposition of Isopropyl Nitrate: Kinetics and Products," *J. Phys. Chem. A*, vol. 120, no. 41, 2016.

[81]   S. N. Bulusu, *Chemistry and Physics of Energetic Materials*. Kluwer Academic Publishers, 1990.

[82]   A. A. Borisov, K. Y. Troshin, and V. N. Mikhalkin, "Ignition and Combustion of IPN," *Russ. J. Phys. Chem. B*, vol. 10, no. 5, pp. 780–784, 2016.

[83]   E. O. R. Guirguis, D. Hsu, D. Bogan, "A Mechanism for Ignition of High Temperature Gaseous Nitromethane - The Key Role of the Nitro Group in Chemical Explosives," *Combust. Flame*, vol. 61, pp. 51–62, 1985.

[84]   C. F. Melius, "Thermochemistry and Reaction Mechanisms of Nitromethane Ignition," *J. Phys. III*, vol. 5, 1995.

[85]   G. M. Faeth, B. L. Karhan, and G. A. Yanyecicj, "Ignition and Combustion of Monopropellant Droplets."

[86]   I. Awasthi, D. N. Pope, and G. Gogos, "Effects of the ambient temperature and initial diameter in droplet combustion," *Combust. Flame*, 2014.

[87]   I. Awasthi, G. Gogos, and T. Sundararajan, "Effects of size on combustion of isolated methanol droplets," *Combust. Flame*, 2013.

[88]   T. Saitoh, K. Yamazaki, and R. Viskanta, "Effect of Thermal Radiation on Transient Combustion of a Fuel Droplet," *J. Thermophys. Heat Transf.*, vol. 7, no. 1, 1993.

[89]   M. Pilch and C. A. Erdman, "Use of Breakup Time Data and Velocity History Data to Predict the Maximum Sie of Stable Fragments for Acceleration-Induced Breakup of a Liquid Drop," *Int. J. Multiph. Flow*, vol. 13, no. 6, pp. 741–757, 1987.

[90]   W. A. Sirignano, "Droplet Behavior Under Near-critical, Transcritical, and Supercritical Conditions," in *Fluid Dynamics and Transport of Droplets and Sprays*, 2nd ed., Cambridge University Press, 2010.

[91]   A. A. Borisov, B. E. Gel'fand, M. S. Natanzon, and O. M. Kossov, "Droplet Breakup Regimes and Criteria for their Existence," *J. Eng. Phys.*, vol. 40, no. 1, pp. 44–49, 1981.

[92]   M. M. Avulapati, L. C. Ganippa, J. Xia, and A. Megaritis, "Puffing and Micro-explosion of Diesel-Biodiesel-Ethanol Blends," *Fuel*, vol. 166, pp. 59–66, 2016.

[93]   W. A. Sirignano, "Multicomponent-Liquid Droplets," in *Fluid Dynamics and Transport of Droplets and Sprays*, 2nd ed., Cambridge University Press, 2010, pp. 90–133.

[94]   J. Shinjo, J. Xia, L. C. Ganippa, and A. Megaritis, "Physics of Puffing and Microexplosion of Emulsion Fuel Droplets," *Phys. Fluids*, vol. 26, no. 103302, 2014.

[95]   C. K. Law, "Recent Advances in Droplet Vaporization and Combustion," *Prog. Energy Combust. Sci.*, vol. 8, pp. 171–201, 1982.

[96]   M. L. Botero, Y. Huang, D. L. Zhu, A. Molina, and C. K. Law, "Synergistic Combustion of Droplets of Ethanol, Diesel and Biodiesel Mixtures," *Fuel*, vol. 94, pp. 342–347, 2012.

[97] A. Lee and C. K. Law, "An Experimental Investigation on the Vaporization and Combustion of Methanol and Ethanol Droplets," *Combust. Sci. Technol.*, vol. 86, pp. 1–6, 1992.

[98] R. Stauch and U. Maas, "The Ignition of Methanol Droplets in a Laminar Convective Environment," *Combust. Flame*, vol. 153, pp. 45–57, 2008.

[99] A. Matsugi and H. Shiina, "Thermal Decomposition of Nitromethane and Reaction between CH3 and NO2," *J. Phys. Chem. A*, vol. 121, no. 22, pp. 4218–4224, 2017.

[100] E. Boyer, "Combustion Characteristics and Flame Structure of Nitromethane Liquid Monopropellant," The Pennsylvania State University, 2005.

[101] H. Krause, N. Eisenreich, and A. Pfeil, "Kinetics of Evaporation and Decomposition of Isopropyl Nitrate by Rapid Scan IR Spectroscopy," *Thermochim. Acta*, vol. 149, no. 10, pp. 349–356, 1989.

[102] S. C. Wong, T. S. Hsu, and J. C. Chang, "Validity of Droplet Ignition Criteria Derived Assuming Gas-Phase Quasisteadiness," *J. Propuls. Power*, vol. 11, no. 1, 1996.

[103] F. A. Williams, "A Review of Flame Extinction," *Fire Saf. J.*, vol. 3, pp. 163–175, 1981.

[104] N. Peters, "Combustion Theory," *Lecture Notes, CEFRC Summer School, Princeton*. 2010.